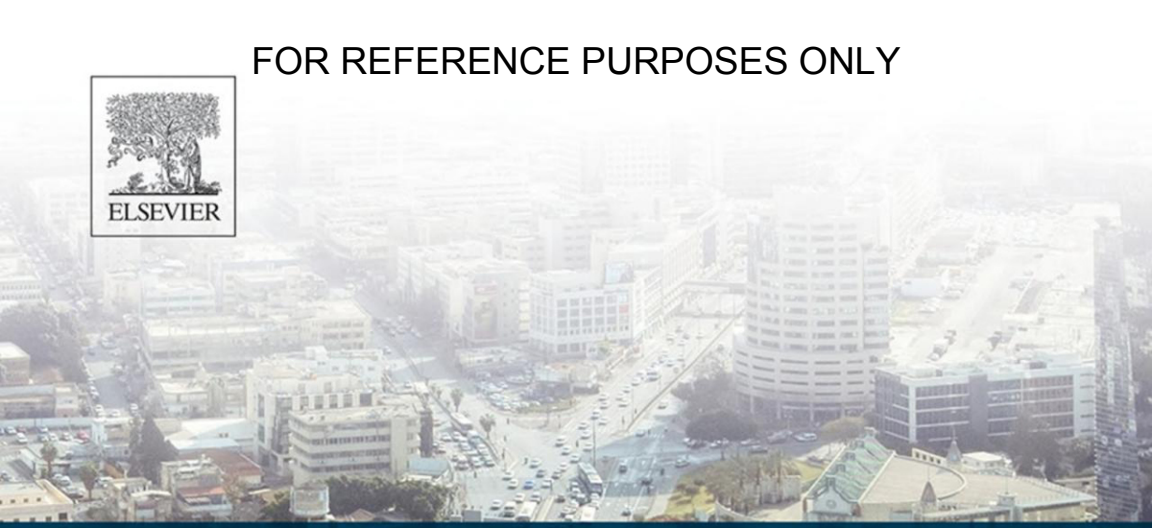

URBAN TRANSPORTATION AND AIR POLLUTION

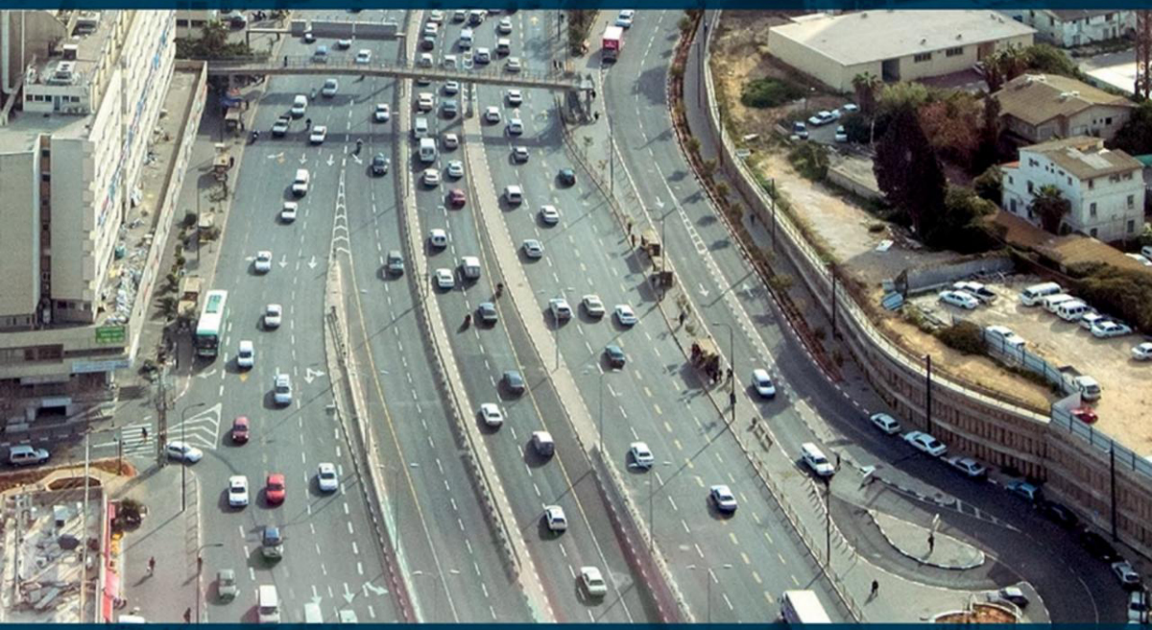

AKULA VENKATRAM • NICO SCHULTE

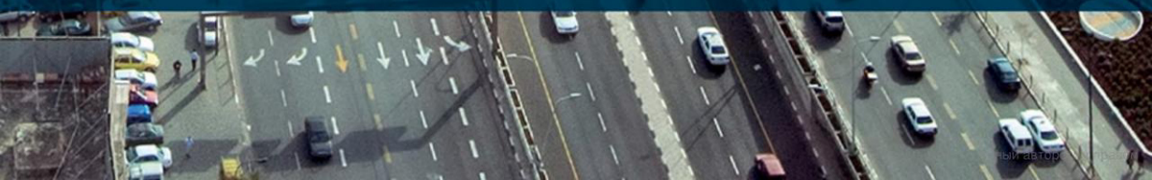

URBAN TRANSPORTATION AND AIR POLLUTION

URBAN TRANSPORTATION AND AIR POLLUTION

AKULA VENKATRAM
Department of Mechanical Engineering,
University of California, Riverside, CA, United States

NICO SCHULTE
California Air Resources Board, Research Division,
Sacramento, CA, USA

Elsevier
Radarweg 29, PO Box 211, 1000 AE Amsterdam, Netherlands
The Boulevard, Langford Lane, Kidlington, Oxford OX5 1GB, United Kingdom
50 Hampshire Street, 5th Floor, Cambridge, MA 02139, United States

Notices
Knowledge and best practice in this field are constantly changing. As new research and experience broaden our understanding, changes in research methods, professional practices, or medical treatment may become necessary.

Practitioners and researchers must always rely on their own experience and knowledge in evaluating and using any information, methods, compounds, or experiments described herein. In using such information or methods they should be mindful of their own safety and the safety of others, including parties for whom they have a professional responsibility.

To the fullest extent of the law, neither the Publisher nor the authors, contributors, or editors, assume any liability for any injury and/or damage to persons or property as a matter of products liability, negligence or otherwise, or from any use or operation of any methods, products, instructions, or ideas contained in the material herein.

British Library Cataloguing-in-Publication Data
A catalogue record for this book is available from the British Library

Library of Congress Cataloging-in-Publication Data
A catalog record for this book is available from the Library of Congress

ISBN: 978-0-12-811506-0

Publisher: Joe Hayton
Acquisition Editor: Brian Romer
Editorial Project Manager: Andrae Akeh
Production Project Manager: Surya Narayanan Jayachandran
Cover Designer: Greg Harris

Typeset by MPS Limited, Chennai, India

PREFACE

This book resulted out of a conversation I had with Brian Romer, the senior transportation editor from Elsevier, who contacted me in late 2015 after he had seen a paper I had co-authored. The paper dealt with the impact of vehicle emissions on near-road air quality. He convinced me that I could expand the topic to cover the broad field covering the relationship between vehicle emissions and urban air quality. I agreed with a little hesitation because several of my students had worked on this topic in their PhD research. Nico Schulte was finishing up his thesis on the impact of near-roadway structures, including noise barriers and urban buildings, on dispersion of vehicle emissions. I thought it was simply a matter of expanding his thesis with appropriate background. However including this background turned out to be much more difficult than I thought it would be. Nico Schulte and I have worked on this book for the last two years to include material that provides the rudimentary understanding of micrometeorology and dispersion required to follow the core of the subject. We felt that this was necessary because our experience indicates that a large fraction of people involved in air pollution modeling do not have the background to interpret the micrometeorological inputs required by currently used short-range dispersion models, such as AERMOD (Cimorelli et al., 2005). Furthermore, there is enough detail in the book to allow the reader to understand the formulation of these models. Thus the book can serve a student interested in the subject, as well as the practitioner who wants to examine the underlying machinery.

This book deals with one aspect of Urban Transportation and Air Pollution. Its primary focus is the development and application of dispersion models to estimate the impact of vehicle emissions on near-road air quality in the complex urban environment. It draws heavily on research that Nico and I have participated in with our collaborators. Thus the book has a relatively narrow focus on the type of models that we have developed and applied. The book is relatively brief because it is confined to models that we can vouch for through evaluation with observations from field studies and wind tunnel experiments.

We refer to the models described in this book as semi-empirical. These models combine a relatively simple mechanistic framework with an empirical approach to account for secondary processes not captured

explicitly; they are not purely statistical relationships between concentrations and the governing variables. Their formulation is based on the hypothesis that the behavior of complex systems can be described by a small number of variables embedded in a framework based on conservation principles. These variables are then combined to yield equations that contain parameters whose values are obtained by fitting model estimates with corresponding measurements. An example of this approach is illustrated in the model for the impact of buildings on dispersion of vehicle emissions in urban areas (Schulte et al., 2015). The framework consists of a mass balance that equates emissions at street level to transport of these emissions in the vertical direction through turbulent diffusion. The associated eddy diffusivity is formulated in terms of the standard deviation of the vertical velocity fluctuations and a length scale that depends on building geometry, which in turn is described in terms of the effective height and the aspect ratio of the buildings lining the urban street of concern. The formulation for the length scale and the relating turbulence and building geometry contain parameters, whose values are obtained by fitting estimates of concentration from the overall model with corresponding measurements.

The applicability of these models outside the range of measurements used in the fitting procedure is determined by two criteria: (1) the validity of the mechanistic foundation, and (2) the variation of the model parameters, which should be as small as possible. The major strength of these models is that they are firmly anchored to observations. In formulating their framework, we use an approach that yields "sensible values" over a wide range of inputs. We achieve this by interpolating between model formulations that can be supported by theory as well as observation. For example, the formulation for vertical plume spread (Venkatram and Schulte, 2014) for the entire range of unstable conditions interpolates between expressions for neutral and very unstable conditions. These expressions can be justified using theory, as well as observations from the Prairie Grass experiment (Barad, 1958). The interpolation is cast in terms of parameters that provide the best fit between model estimates and observations. A similar approach is used in constructing the complex terrain model in AERMOD (Venkatram et al., 2001), described in Appendix A.

This book does not discuss modeling based on computational fluid dynamics (CFD), which attempts to describe all the details of the

governing processes through the numerical solution of the conservation equations. On the other hand, we do acknowledge the valuable insight provided by CFD models that help to formulate semi-empirical models.

There are very few practitioners of semi-empirical modeling, and most of them have collaborated with us in developing the models described in this book. Vlad Isakov, Richard Baldauf, Steven Perry, and David Heist from the United States Environmental Protection Agency (USEPA) worked with us in developing the models described in this book. This collaboration is one of the major reasons that components of our models are incorporated in practice-oriented models, such as AERMOD (Cimorelli et al., 2005) and R-LINE (Snyder et al., 2013), which are widely used to estimate concentrations associated with a variety of pollutant sources. The semi-empirical models are also components of modeling systems to estimate the impact of emissions from urban highways (Barzyk et al., 2015) and seaports (Isakov et al., 2017). Other significant collaborators are Marko Princevac, David Pankratz, Dennis Fitz, Alan Cimorelli, Robert Paine, Sarav Arunachalam, Parikshit Deshmukh, Michelle Snyder, Jeffrey Weil, and Steven Hanna.

My students have played a major role in developing the semi-empirical models described here. Shuming Du, Qiguo Jing, Jing Yuan, Si Tan, and Wenjun Qian helped me with my early research in dispersion modeling. I am deeply grateful to Sam Pournazeri who contributed to several chapters as well as the Appendix of the book. He is also responsible for the colorful illustrations in these sections. The major contributors to the core of the book are Seyedmorteza Amini and Faraz Enayati Ahangar, my students. Nico Schulte, the coauthor of this book, collaborated with me in my research and also helped me bring past research together to create a coherent book.

The research that resulted in the models described in this book has been supported by the California Air Resources Board, the South Coast Air Quality Management District, the California Energy Commission, the National Science Foundation and the USEPA.

REFERENCES

Barad, M.L., 1958. Project Prairie Grass: a field program in diffusion vol II. Geophys. Res. Pap. Available from: https://doi.org/10.1016/0022-460X(71)90105-2.

Barzyk, T.M., Isakov, V., Arunachalam, S., Venkatram, A., Cook, R., Naess, B., 2015. A near-road modeling system for community-scale assessments of traffic-related air pollution in the United States. Environ. Model. Softw 66, 46–56. Available from: https://doi.org/10.1016/j.envsoft.2014.12.004.

Cimorelli, A.J., Perry, S.G., Venkatram, A., Weil, J.C., Paine, R.J., Wilson, R.B., et al., 2005. AERMOD: A dispersion model for industrial source applications. Part I: General model formulation and boundary layer characterization. J. Appl. Meteorol. 44, 682–693. Available from: https://doi.org/10.1175/JAM2227.1.

Isakov, V., Barzyk, T.M., Smith, E.R., Arunachalam, S., Naess, B., Venkatram, A., 2017. A web-based screening tool for near-port air quality assessments. Environ. Model. Softw 98. Available from: https://doi.org/10.1016/j.envsoft.2017.09.004.

Schulte, N., Tan, S., Venkatram, A., 2015. The ratio of effective building height to street width governs dispersion of local vehicle emissions. Atmos. Environ. 112, 54–63. Available from: https://doi.org/10.1016/j.atmosenv.2015.03.061.

Snyder, M.G., Venkatram, A., Heist, D.K., Perry, S.G., Petersen, W.B., Isakov, V., 2013. RLINE: A line source dispersion model for near-surface releases. Atmos. Environ. 77, 748–756. Available from: https://doi.org/10.1016/j.atmosenv.2013.05.074.

Venkatram, A., Brode, R., Cimorelli, A., Lee, R., Paine, R., Perry, S., et al., 2001. A complex terrain dispersion model for regulatory applications. Atmos. Environ. 35. Available from: https://doi.org/10.1016/S1352-2310(01)00186-8.

Venkatram, A., Schulte, N., 2014. On formulating equations for plume spreads for near-surface releases. Int. J. Environ. Pollut. 54. Available from: https://doi.org/10.1504/IJEP.2014.065116.

CHAPTER ONE

Introduction

Contents

Scope of the Book 1
Models Treated in this Book 2
Modeling Emissions for Transport Applications 4
Organization of this Book 8
References 10

SCOPE OF THE BOOK

This book summarizes some of the research conducted during the last 15 years on estimating the impact of vehicle-related emissions on near road air quality. Although the impact of roadway emissions on air quality has been studied since the 1970s, it has become prominent more recently in the light of a number of epidemiological studies reporting associations between living within a few hundred meters of high-traffic roadways and adverse health effects such as asthma and other respiratory impacts, birth and developmental effects, premature mortality, cardiovascular effects, and cancer (e.g., Harrison et al., 1999; Brauer et al., 2002; Hoek et al., 2002; Finkelstein et al., 2004).

Air quality monitoring studies conducted near major roadways indicate that these health effects are associated with elevated concentrations, compared with overall urban background levels, of motor-vehicle-emitted compounds, which include carbon monoxide (CO); nitrogen oxides (NO_x); coarse ($PM_{10-2.5}$), fine ($PM_{2.5}$), and ultrafine ($PM_{0.1}$) particle mass; particle number; black carbon, polycyclic aromatic hydrocarbons, and benzene (Kim et al., 2002; Hutchins et al., 2000; Kittelson et al., 2004).

This book describes models that describe the transport and dispersion of pollutants emitted from vehicles traveling on urban roads. It does not deal with the chemistry of pollutant formation or the factors that determine the emissions rate from vehicles. This is a subject with an extensive

Urban Transportation and Air Pollution.
DOI: https://doi.org/10.1016/B978-0-12-811506-0.00001-4

literature that can be readily consulted by the reader. We confine ourselves to the modeling of the processes that connect emissions to the corresponding concentrations at a receptor. We first review the types of models that are generally used to estimate concentrations as a backdrop to the models that we discuss in this book.

MODELS TREATED IN THIS BOOK

An air quality model is a mathematical description of the system that governs the fate of air pollutants emitted into the atmosphere. The air quality system consists of a large number of processes, which include transport by the mean wind, dispersion through turbulence, scavenging through dry and wet deposition, and chemistry involving the chemical species in the atmosphere. The relative importance of these processes depends on the source-receptor distance of concern. For example, at distances of a few tens of kilometers from a source, transport and dispersion are the dominant processes although this is not always true.

It is convenient to use different approaches to modeling air pollution depending on source-receptor distances. For distances of tens of kilometers from the source, a continuously emitted pollutant is treated as a plume governed by meteorology in the vicinity of the source. For larger distances, when meteorological variables show significant spatial and temporal variations, it is more convenient to model the fate of emissions using puff models or Eulerian grid models. In puff models, an emission over a short period of time is embedded in a puff or air parcel, which is then tracked as it follows the varying wind field. The puff grows in response to turbulent dispersion, and the chemical species inside the puff undergo scavenging and chemical reactions. Puff models require a great deal of bookkeeping because one needs to keep track of the large number of puffs that correspond to each hour of emission. Some of this bookkeeping can be avoided through receptor-oriented puff models. In this approach, the concentration of the species at a receptor is governed only by the puff that arrives at the time and location of interest. The final state of this puff is determined by calculating the history of puff before it arrives at the receptor. This involves tracing the path of the puff as it passes over emissions and is subject to scavenging and chemical reactions.

The Eulerian grid model solves the mass conservation equations using a grid of boxes. In essence, a mass balance is performed for each box for a short period of time. This mass balance involves inflow and outflow of material in the box through transport and dispersion, scavenging through wet and dry processes, and chemical reactions among the species in the box. The boxes within the domain of interest are interconnected through transport between the boxes. The computational requirements of a grid model are proportional to the number of grid boxes used to describe the domain; a change in grid size by a factor of 2 increases the number of boxes by a factor of 8. Therefore grid resolution has to be relatively coarse, about 1 km, to keep the computational requirements at a manageable level. Parallel computing is being used to solve this computational problem, but for the time being, Eulerian grid boxes have horizontal dimensions of about a kilometer. This means that individual plumes cannot be resolved in such models. Thus these models are best suited to estimate concentrations averaged over kilometers. Because Eulerian models can treat complex chemistry, they are used to model the fate of photochemical pollutants over regional and continental scales.

This book focuses on plume-based models applicable to source-receptor distances of a few kilometers. Most short-range dispersion models are based on the assumption that meteorological conditions are spatially homogeneous and vary little with time during the period of interest, which is typically 1 hour. This is equivalent to saying that the time scale governing the variation in meteorology is greater than the time of travel between source and receptor. If the meteorological time scale is 1 hour, and the wind speed is 5 m/s, the assumption of steady state is not likely to be valid for distances much >10 km. At lower wind speeds, the "valid" distances become smaller. In spite of these limitations, steady state plume models are often applied beyond their range of applicability with the justification that the concentration at the receptor is representative of that when the plume eventually reaches the receptor. In principle, dispersion during unsteady and spatially varying conditions can be treated with puff or particle models, which attempt to model the dispersion of puffs or particles as the unsteady wind field carries them along their trajectories. This book does not discuss models based on puff dispersion.

This book focuses on dispersion of near surface releases because most transportation emissions, such as those from vehicles, occur close to the ground. The models presented here are derived from data collected in field and laboratory studies in which emissions were released over flat

terrain, and the meteorological variables governing dispersion of the release were relatively homogeneous over the area in which dispersion was studied. Such idealized conditions do not apply to the inhomogeneous urban areas in which typical transportation sources such as highways and roads are found. However, the models described here represent a convenient framework to describe data in urban areas, and can be modified to provide useful estimates of concentrations. We support this contention by showing the evaluation of these models with data from field studies conducted in urban areas.

The models described here belong to genre that regulatory models, such as AERMOD (Cimorelli et al., 2005), belong to. These models require modest computational resources, capture the essential physics of the system, and are anchored to observations through empirically derived parameters. They are designed to provide realistic estimates of concentrations associated with emissions from the transportation sector under varying conditions. For example, these models can provide answers to questions such as

1. What is the concentration of particulate matter at a distance of 300 m from the edge of a 40 m highway with a traffic flow rate of 10,000 vehicles/day under a specific meteorological condition?
2. What is the effect of a noise barrier on this concentration?
3. How is the concentration affected if the road is depressed by 6 m?
4. What is the impact of micrometeorology on the spatial distribution of concentrations next to a road?

MODELING EMISSIONS FOR TRANSPORT APPLICATIONS

As indicated earlier, we will not go into the chemistry of the formation of vehicle-related pollutants such as CO, NO_x, and hydrocarbons, or describe models that estimate the emissions of these pollutants. Here, we will treat emissions as one of the inputs to the dispersion models that we describe, and show how they are specified in them.

Most of the transport-related sources are mobile: cars, trucks, or trains. While in principle, we can model the air quality impact of each of these moving sources, it is more convenient to model emissions by treating them as a group that is traveling on a road. Let us illustrate this idea

by considering a road that is associated with a traffic flow rate of T_r vehicles per unit time. Then, any segment of the road, when averaged over say an hour, appears to be populated by a group of vehicles. In air pollution modeling, we are usually interested in specifying the emission rate per unit length of this segment of the road. Assume that density of vehicles in this segment is $\rho_v(x)$ vehicles per unit length of the road, and x is the distance along the road in a suitable coordinate system. If the average emission rate of each vehicle is $\dot{e}$ mass/time, then the emission rate per unit length of this segment is $q = \rho_v \dot{e}$. Because $T_r = \rho_v v$, where v is the average velocity of the vehicle,

$$q = T_r\left(\frac{\dot{e}}{v}\right). \tag{1.1}$$

As we will see in later chapters, q, the emission rate per unit length of the road, is the primary way that emission from vehicles are included in dispersion models. The combination, $\left(\dot{e}/v\right)$, which we denote by e_f, is called the emission factor, which represents the pollutant mass emitted by each vehicle when traveling a unit length of the road.

Emissions of pollutants from vehicles are usually expressed as emission factors because testing procedures specified by the USEPA measure this quantity. A vehicle is driven on a dynamometer over a specified velocity/time path called the Federal Test Procedure (FTP) driving cycle, which is then converted into a distance. Pollutants from the exhaust of the vehicle during this test are accumulated and converted into pollutant mass, which when divided by the distance traveled yields the emission factor. Because the emissions correspond to the FTP driving cycle, the emission factors are corrected for non-FTP speeds and accelerations using statistical methods. This approach forms the basis for the most popular emission models such as MOBILE and EMFAC. These factors can only cover a limited range of the highway and vehicle characteristics that determine emissions. For example, these factors do not account for road grade, which has a significant impact on emissions. Furthermore, empirically based emission factors shed little light on the physical processes that govern emissions.

An alternative to the FTP/correction factor approach is the modal emissions approach (Barth et al., 1996) in which the pollutant emission rate is related to the fuel consumption rate. The assumption is that the relationship is linear. The fuel consumption rate, F_f, is in turn related to the power demand of a vehicle.

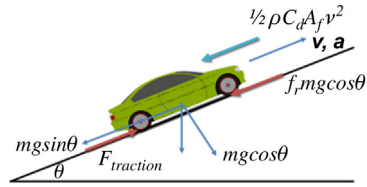

Figure 1.1 Forces acting on a vehicle.

To examine this idea further, consider the power required for the traction of a vehicle traveling on a road with a grade of $\tan(\theta)$. Fig 1.1 shows a free body diagram of a vehicle traveling on the road. The force balance on a vehicle of mass, m, traveling at a velocity, v, with an instantaneous acceleration, a, is

$$F_{traction} - \frac{1}{2}\rho C_d A_f v^2 - mg\,(\sin\theta + f_r\cos\theta) = Ma, \tag{1.2}$$

where $F_{traction}$ is the traction force at the wheels, ρ is the density of air, C_d is the drag coefficient, g is the acceleration due to gravity, and f_r is the rolling friction coefficient. The second term on the left-hand side is the resistance offered by the wind, the third term is the gravitational force, and the fourth term is rolling friction, which is assumed to be proportional to the normal force on the grade.

The traction power is $F_{traction}v = P_{traction}$, which can be obtained by multiplying Eq. (1.2) by v to give

$$P_{traction} = \frac{1}{2}\rho C_d A_f v^3 + mgv\left(\sin\theta + f_r\cos\theta + \frac{a}{g}\right). \tag{1.3}$$

If we assume that the fuel consumption rate and hence the emission rate is proportional to the traction power, Eq. (1.1) implies

$$e_f \sim \frac{1}{2}\rho C_d A_f v^2 + mg\left(\sin\theta + f_r\cos\theta + \frac{a}{g}\right). \tag{1.4}$$

A more realistic model for the emission factor includes other factors such as combustion stoichiometry, engine speed, and displacement (Barth and Boriboonsomsin, 2009). But even this simple model tells us that the emission factor depends on vehicle as well as road characteristics, and is likely to differ substantially from the FTP emission factor, which is based on a driving cycle that might differ substantially from that in a specific case, such as highway driving on a grade.

Eq. (1.4) indicates that a grade of 3% doubles the fuel consumption rate and hence the pollutant emission rate of a vehicle with a mass of 1500 kg driving on a highway at 60 mi/h. Here we have assumed $f_r = 0.01$, $C_d \times A_f = 0.6\ \text{m}^2$, and $\rho = 1.2\ \text{kg m}^{-3}$. An acceleration of 3% of g produces an equivalent effect.

In principle, we could use a "modal" model (Barth et al., 2000) based on Eq. (1.4) to estimate emissions, but this will require information on vehicle and road characteristics that might not be always available. Even with partial information, deterministic emission models allow us to use pollutant concentrations measured in the vicinity of one highway to estimate that at another highway with different characteristics. Consider this example in which a concentration of 50 ppb of NO_x is measured at 25 m from a highway with a traffic flow rate of 1000 vehicles/h traveling on level ground at 65 mi/h. What is the corresponding concentration next to a similar highway in which the traffic flow rate is 800 vehicles/h, and the average speed is 50 mi/h on a grade of 4%? Under similar meteorological conditions, the concentration at the same distance from each of the highways is proportional to the emission per unit length of the road. Taking $m = 1500$ kg, $f_r = 0.01$, $C_d \times A_f = 0.6\ \text{m}^2$, $\rho = 1.2\ \text{kg m}^{-3}$, Eqs. (1.1) and (1.4) yield an estimate of 80 ppb.

There is another common method of quantifying emissions that might be useful in dispersion modeling. This method quantifies emissions in terms of mass of a specific pollutant emitted per unit mass of fuel burned. It is estimated by measuring the ratio of the pollutant concentration to the mass of carbon in the exhaust gases or at a location close enough to the highway that dispersion is the primary mechanism for the reduction in exhaust gas concentrations. This ratio is converted into the required emission metric through information on the carbon content of the fuel. Singer and Harley (1996) and Ning et al. (2008) provide useful fuel-based emission factors for a variety of pollutants. This fuel-based emission factor has been used to produce city-wide estimates of pollutant emissions using estimates of gasoline and diesel sales.

How can fuel-based emission factors be used in dispersion calculations? We can convert them into emission rates by multiplying them with fuel consumption rates, which in turn can be estimated using deterministic models (Ross, 1994) that have been discussed earlier. The associated uncertainty is that we do not know the vehicle and the road characteristics corresponding to any particular measurement of the emission factor to allow us to scale the measured emission factor using this information.

The review of traffic emission models by Smit et al. (2010) indicates that the error in emission estimates can be over a factor of 2 for most pollutants. We need to account for this uncertainty in applying and evaluating dispersion models. We suggest the application of deterministic "modal" emission models in reducing some of this uncertainty.

ORGANIZATION OF THIS BOOK

Chapter 2, Fundamental Concepts of this book discusses terminology and concepts used in characterizing air pollutants and the meteorological processes that govern their concentrations. We first review different methods of quantifying pollutant concentrations and how to convert concentrations expressed in one set of units to another. After a brief description of the composition and vertical structure of the atmosphere, we introduce the important approximation of the vertical momentum equation that balances gravity with the vertical pressure gradient resulting in the hydrostatic balance equation, which is used to estimate the variation of pressure with height from the ground. We provide a brief description of the physical processes that govern large-scale winds and weather systems. These systems determine the meteorological variables that govern the transport and dispersion of air pollutants. This chapter also discusses the important concept of potential temperature, and how it relates to the static stability of the atmosphere.

Chapter 3, Fundamentals of Micrometeorology and Dispersion provides material that is essential to the understanding of the current literature on modeling dispersion in the surface boundary layer, where most transport-related emissions occur. Our discussion of micrometeorology emphasizes its central role in formulating models for the behavior of plumes in the surface layer. A great deal of micrometeorology is semiempirical in the sense that major results are often based on dimensional analysis and unknown parameters in equations are obtained by fitting to observations. This approach often prevents appreciation of their physical content. We alleviate this problem by using simple physically based models to justify these results. For example, we estimate the magnitude of the turbulent velocities generated by buoyancy through relatively simple arguments. We then relate these velocities to the free convection velocity and

the convective velocity scales that are used in micrometeorological formulations. We also provide an intuitively appealing interpretation of the Monin-Obukhov length, which is the primary length scale used in expressions for the velocity and temperature profiles in the surface boundary layer.

Chapter 3, Fundamentals of Micrometeorology and Dispersion shows how micrometeorology and dispersion theory are combined to derive expressions for the vertical and horizontal spreads of a pollutant plume dispersing in the surface boundary layer. The material is not easy going for a beginning student, but we believe that it is a prerequisite for understanding the formulation of plume spreads in models such as AERMOD (Cimorelli et al., 2005) and RLINE (Snyder et al., 2013; Venkatram et al., 2013), which are used to estimate the impact of transport-related emissions.

Chapter 4, The Impact of Highways on Urban Air Quality applies the methods developed in Chapter 2, Fundamental Concepts to formulating models for dispersion of vehicle-emitted pollutants from highways. As in Chapter 3, Fundamentals of Micrometeorology and Dispersion, we delve into the details of the derivation of the models to allow the reader to understand the approximations made in their formulations. Rather than reviewing all the models in current use, we focus on a few that we have developed. While some might argue that this is a biased approach, our defense is that the models that we describe are similar to others in use, and also represent the current state-of-the-art. Another important aspect of this chapter is that we present the evaluation of these models with observations to (1) show that the models provide estimates of real world concentrations and (2) provide the model user with the estimates of model uncertainty. The chapter deals with how the basic highway model can be modified to account for the impact of roadside barriers, both solid and vegetative. We also present a method to estimate the impact of emissions from depressed highways.

Chapter 5, The Impact of Buildings on Urban Air Quality deals with the effects of urban buildings on dispersion of vehicle emissions. We review available models that estimate the impact of buildings, and then focus on a model that we have developed. As in Chapter 4, The Impact of Highways on Urban Air Quality, we derive the relevant equations, and then provide an extensive discussion of the evaluation of the model.

Chapter 6, Modeling Dispersion at City Scale summarizes the results presented in this book in the form of simple models that can be used to

estimate the major effects of urban structures on dispersion of vehicle-emitted pollutants. It also provides a brief description of methods to estimate the micrometeorological inputs that are required to apply dispersion models in urban areas.

REFERENCES

Barth, M., An, F., Norbeck, J., Ross, M., 1996. Modal emissions modeling: a physical approach. Transp. Res. Rec. 1520, 81–88. Available from: https://doi.org/10.3141/1520-10.

Barth, M., An, F., Younglove, T., Scora, G., Levine, C., Ross, M., et al., 2000. Development of a comprehensive modal emissions model. Natl. Coop. Highw. Res. Progr 5–11.

Barth, M., Boriboonsomsin, K., 2009. Energy and emissions impacts of a freeway-based dynamic eco-driving system. Transp. Res. Part D Transp. Environ. 14, 400–410. Available from: https://doi.org/10.1016/j.trd.2009.01.004.

Brauer, M., Hoek, G., Van Vliet, P., Meliefste, K., Fischer, P.H., Wijga, A., et al., 2002. Air pollution from traffic and the development of respiratory infections and asthmatic and allergic symptoms in children. Am. J. Respir. Crit. Care Med. 166, 1092–1098. Available from: https://doi.org/10.1164/rccm.200108-007OC.

Cimorelli, A.J., Perry, S.G., Venkatram, A., Weil, J.C., Paine, R.J., Wilson, R.B., et al., 2005. AERMOD: a dispersion model for industrial source applications. Part I: General model formulation and boundary layer characterization. J. Appl. Meteorol. 44. Available from: https://doi.org/10.1175/JAM2227.1.

Finkelstein, M.M., Jerrett, M., Sears, M.R., 2004. Traffic air pollution and mortality rate advancement periods. Am. J. Epidemiol. 160, 173–177. Available from: https://doi.org/10.1093/aje/kwh181.

Harrison, R.M., Leung, P.L., Somervaille, L., Smith, R., Gilman, E., 1999. Analysis of incidence of childhood cancer in the West Midlands of the United Kingdom in relation to proximity to main roads and petrol stations. Occup. Env. Med. 56, 774–780. Available from: https://doi.org/10.1136/oem.56.11.774.

Hoek, G., Brunekreef, B., Goldbohm, S., Fischer, P., van den Brandt, P.A., 2002. Association between mortality and indicators of traffic-related air pollution in the Netherlands: a cohort study. Lancet 360, 1203–1209.

Hutchins, J., Morawska, L., Wolff, R., Gilbert, D., 2000. Concentrations of submicrometre particles from vehicle emissions near a major road. Atmos. Environ. 34 (1), 51–59.

Kim, J., Smorodinsky, S., Ostro, B., Lipsett, M., Singer, B., Hogdson, A., 2002. Traffic-related air pollution and respiratory health: the East Bay Children's Respiratory Health Study. Epidemiology 13 (4), S100.

Kittelson, D.B., Watts, W.F., Johnson, J.P., 2004. Nanoparticle emissions on Minnesota highways. Atmos. Environ. 38 (1), 9–19.

Ning, Z., Polidori, A., Schauer, J.J., Sioutas, C., 2008. Emission factors of PM species based on freeway measurements and comparison with tunnel and dynamometer studies. Atmos. Environ. 42, 3099–3114. Available from: https://doi.org/10.1016/j.atmosenv.2007.12.039.

Ross, M., 1994. EMISSIONS : effects of vehicle and driving characteristics. Annu. Rev. Energy Environ. 19, 75–112. Available from: https://doi.org/10.1146/annurev.energy.19.1.75.

Singer, B.C., Harley, R.A., 1996. A fuel-based motor vehicle emission inventory. J. Air Waste Manag. Assoc. 46, 581–593. Available from: https://doi.org/10.1080/10473289.1996.10467492.

Smit, R., Ntziachristos, L., Boulter, P., 2010. Validation of road vehicle and traffic emission models – a review and meta-analysis. Atmos. Environ. 44, 2943–2953. Available from: https://doi.org/10.1016/j.atmosenv.2010.05.022.

Snyder, M.G., Venkatram, A., Heist, D.K., Perry, S.G., Petersen, W.B., Isakov, V., 2013. RLINE: a line source dispersion model for near-surface releases. Atmos. Environ. 77, 748–756. Available from: https://doi.org/10.1016/j.atmosenv.2013.05.074.

Venkatram, A., Snyder, M.G., Heist, D.K., Perry, S.G., Petersen, W.B., Isakov, V., 2013. Re-formulation of plume spread for near-surface dispersion. Atmos. Environ. 77, 846–855. Available from: https://doi.org/10.1016/j.atmosenv.2013.05.073.

CHAPTER TWO

Fundamental Concepts

Contents

Expressing Concentrations 13
The Composition of Air 17
Hydrostatic Equilibrium 18
The Potential Temperature 21
Atmospheric Stability 22
The Origin of Large-Scale Winds 25
The Pressure Gradient Force 25
The Coriolis Force 27
The Geostrophic Wind 29
High- and Low-Pressure Centers 32
Effects of Friction 34
Fronts 35

This chapter provides a brief review of several topics that help in understanding air pollution in urban areas. We first describe methods used to quantify concentrations of different species in air. We then introduce the variables that are used to characterize the vertical structure of the atmospheric layer in which pollutants are transported. The last section of this chapter describes meteorological concepts relevant to air pollution.

EXPRESSING CONCENTRATIONS

The most obvious way of expressing concentrations in air is in terms of **mass per unit volume**, which is simply the mass of the species in a given volume divided by the volume. Concentrations are usually expressed in terms of milligrams/cubic meter (mg/m^3, $mg = 10^{-3}$ g) or micrograms/cubic meter ($\mu g/m^3$, $\mu g = 10^{-6}$ g). Concentrations of particulate matter in the atmosphere are customarily expressed in mass units.

The concentration of a gas in a mixture of gases is most often expressed in terms of the **mixing ratio (q)** defined by

Urban Transportation and Air Pollution.
DOI: https://doi.org/10.1016/B978-0-12-811506-0.00002-6

$$q = \frac{\textit{concentration of species in a volume}}{\textit{concentration of mixture in the same volume}}. \tag{2.1}$$

The concentration is usually expressed in terms of moles of the gas per unit volume. The mixing ratio is simply the ratio of the number of moles of the species to the number of moles of the mixture in the volume used to calculate concentrations. This means that the mixing ratio does not change if the volume changes. We can always convert mixing ratio to mass per unit volume concentration units at any temperature and pressure by calculating the density of the mixture for these conditions.

To see how this is done, let us review the perfect gas law, which states that:

$$pV = nR_u T, \tag{2.2}$$

where p is the pressure in Newtons/m^2 (a unit referred to as the Pascal denoted by Pa), V is the volume of the gas in m^3, n is the number of moles of the gas, R_u is the universal gas constant and is equal to 8.314 J/(mol K), and T is the temperature in Kelvin.

We can restate Eq. (2.2) in terms of the density of the gas ρ, by expressing the number of moles, n by

$$n = m_g \times 1000/M_w, \tag{2.3}$$

where m_g is the mass of the gas in kg and M_w is the molecular weight of the gas-mass in grams of 1 mole or 6.02×10^{23} molecules of the gas.

Substituting Eq. (2.3) in Eq. (2.2) yields:

$$p = \left(\frac{m_g}{V}\right)\left(\frac{1000R_u}{M_w}\right)T. \tag{2.4}$$

Now, ρ, the density of the gas in mass units is

$$\rho = \frac{m_g}{V}. \tag{2.5}$$

If we define the gas constant specific to the gas as

$$R_g = \frac{1000R_u}{M_w} \tag{2.6}$$

an alternate form of the gas law becomes:

$$p = \rho R_g T. \tag{2.7}$$

If we assume that nitrogen (78% by volume) and oxygen (21% by volume) are the primary components of air, the average molecular weight of air is about $(28 \times 0.78 + 32 \times 0.21)/0.99 = 29$. Let us calculate the gas constant specific to air, R_g by taking $M_w = 29$ g/mole,

$$R_g = \frac{1000\ g/\text{kg} \times 8.314\ J/(\text{mole}\ K)}{29\ g/\text{mole}} = 287\ J/\text{kg K} \quad . \tag{2.8}$$

It is now easy to estimate the density of air at any temperature and pressure. For example, let us estimate the density near the ground where the temperature is 300 K, and the pressure is approximately 10^5 N/m^2. Using Eq. (2.7), we get

$$\rho_a = p/(R_g T) = \frac{10^5\ N/m^2}{287\ J/(\text{kg}\ K) \times 300\ \text{K}} \approx 1.2\ \text{kg}/m^3 \tag{2.9}$$

(notice that Joule = Newton · Meter).

The mixing ratio defined in Eq. (2.1) is essentially a mass ratio. In air pollution work, it is customary to work with **volumetric mixing ratios**. Let us define the volumetric mixing ratio by considering two species, A and B, enclosed in a container with volume V. The gases in the container are subject to a constant atmospheric pressure through a moveable piston exposed to the atmosphere. Now assume that gas B is absorbed using some reagent so that only gas A remains in the container. Because the external pressure remains the same, the piston moves down to enclose a smaller volume occupied by A, denoted by V_A. The volumetric mixing ratio of A is then V_A/V and that of B is $(1-V_A/V)$. This procedure to estimate volumetric mixing ratios can be readily related to molar ratios using the perfect gas law.

Denote the atmospheric pressure by p. Let N be the total number of moles initially in the container, and the number of moles of A be N_A. Then the gas law before and after absorption of B reads:

$$pV = NR_u T, \tag{2.10a}$$

and

$$pV_A = N_A R_u T. \tag{2.10b}$$

We see immediately that the volumetric mixing ratio is simply the mole fraction of the species,

$$\frac{V_A}{V} = \frac{N_A}{N}. \tag{2.11}$$

The mole fraction can be converted in mass per unit volume units at a specified temperature, p_o, and temperature, T_o, using the molar concentration of the mixture of gases given by

$$\frac{N}{V} = \frac{p_o}{R_u T_o}. \tag{2.12}$$

For $p_o = 1.013 \times 10^5\ N/m^2$ (1 atm) and $T_o = 298$ K, the molar concentration works out to be

$$n_a = \frac{N}{V} = \frac{1.013 \times 10^5\ N/m^2}{8.314\ J/(\text{mol K}) \times 298\ \text{K}} \approx 41\ \text{mol}/m^3. \tag{2.13}$$

This concentration is independent of the species. Let us convert 100 ppb of ozone to mass per unit volume units measured at 1 atmosphere and 25°C, which corresponds to the above molar concentration. Now 100 ppb $= 100 \times 10^{-9}$ expressed as a mole fraction, which translates into $10^{-7} \times 41$ mol/m^3. To convert this into mass units, we multiply this concentration by the molecular mass of ozone which is 48 g/mol, and obtain 1.96×10^{-4} g/m^3 or 197 μg/m^3.

This concentration can be referred to some other temperature and pressure, say 0.8 atmospheres and 273 K by noticing that the total molar concentration is directly proportional to pressure, and inversely proportional to temperature. Then the concentration works out to be $197 \times (0.8/1) \times (298/273) = 172$ μg/m^3.

It is just as easy to go from mass per unit volume units to molar mixing ratio by:

- Converting the concentration of the species into mol/m^3 units using the molecular weight of the relevant species;
- Dividing the concentration by the molar concentration of the mixture of gases at the pressure and temperature that the concentration was measured.

To illustrate this conversion, assume that the concentration of sulfur dioxide (SO_2) is measured to be 1000 μg/m^3 at 10°C and a pressure of 900 mb. Let us express this concentration in mixing ratio units. The molecular mass of SO_2 is 64 g/mol, so that the molar concentration is $(1000/64) \times 10^{-6}$ mol/m^3. We need to calculate the density of air (including the gas) at the given pressure and temperature. Note that the

pressure is expressed in terms of millibar $= 10^{-3}$ bar, where bar is an atmospheric pressure unit equal to 10^5 N/m^2 (1 N/m^2 = Pa). Then Eq. (2.13) yields $900 \times 10^{-3} \times 10^5$ N/m^2/(8.314 J/(mol K) $\times$ (273 + 20) K) = 37 mol/m^3 for the molar density of air. The mixing ratio becomes $(1000/64) \times 10^{-6}/37 \times 10^6 = 0.42$ ppm or 420 ppb.

It is sometimes tempting to dismiss atmospheric species concentrations as small simply because they are expressed as parts per billion—1 molecule out of a billion air molecules. This is simply an artifact of the choice of units as can be seen by expressing the concentration in molecules per cubic meter. For example, 1 ppb is approximately $10^{-9} \times 41$(mol/m^3) $\times$ 6×10^{23} molecules/mol $= 2.5 \times 10^{16}$ molecules/m^3, which translates into a large exposure if we consider the fact that we breathe in about 1 m^3/h. This illustrates the fact that terms such as large or small have little meaning; concentration levels assume meaning only when converted into effects of concern, such as that related to human health.

With these preliminaries out of the way, we can discuss the composition of air.

THE COMPOSITION OF AIR

Air primarily consists of nitrogen and oxygen, with nitrogen constituting 78% by volume, and oxygen making up about 21%. This means that 78% of the molecules in any given volume of air consist of nitrogen, and 21% consists of oxygen. The remaining 1% consists of minor constituents such as Argon, Neon, Xenon, and Krypton, whose concentrations are essentially steady with time. There are other minor constituents that are more variable, the most important of which are water vapor and carbon dioxide. Water vapor concentrations are highly variable, ranging from 1% to 10% by volume. As we will see later, the phase changes undergone by these relatively small concentrations of water vapor have profound effects on the energetics of the atmosphere.

The background carbon dioxide concentration is about 350 ppm by volume; which means that 350 molecules of a total of 1 million molecules of air is carbon dioxide. This value is believed to be increasing at a rate of 1.5 ppm/year because of human activity, such as combustion of fossil fuels and deforestation. Both water vapor and carbon dioxide play important

roles in the Greenhouse effect, which refers to the warming caused by the absorption of thermal radiation by these gases.

Chemical species, referred to as air pollutants, contribute to the variable composition of the atmosphere. The species of importance and their typical concentrations are given in the following table:

Species	Concentration (ppb) Polluted	Concentration (ppb) Clean
Sulfur dioxide	100	10
Carbon monoxide	30 (ppm)	3 (ppm)
Nitrogen oxide	50	5
Hydrocarbons	500	50
Ozone	100	10

The composition of pollutants in the atmosphere is governed by the transport and dispersion of anthropogenic emissions into the atmospheric boundary layer, which refers to the lower part of the atmosphere, in contact with the Earth's surface, that is affected by heat and mass transfer between the ground and the atmosphere. The next chapter describes how the boundary layer is characterized in dispersion applications. Here we provide some preliminaries required to understand this chapter.

HYDROSTATIC EQUILIBRIUM

Measurements indicate that the pressure at the Earth's surface is about 10^5 N/m^2, a quantity that is referred to as a **bar**. Standard atmospheric pressure is defined as 1013.25 millibar, where 1 millibar (mb) = 10^{-3} bar. Standard atmospheric pressure corresponds to the pressure at the bottom of column of mercury 76 cm high. Because pressure changes are usually much smaller than a bar, atmospheric pressure is usually expressed in millibars.

We live at the bottom of a large pool of air. The pressure felt at the Earth's surface is caused by the weight of the air above our heads. This means that we should expect the air pressure to go down as we go higher into the atmosphere. Let us use these ideas to get an idea of the variation of pressure in the atmosphere. We know that the density of air is about 1 kg/m^3 near the ground. If we assume that the density does not vary

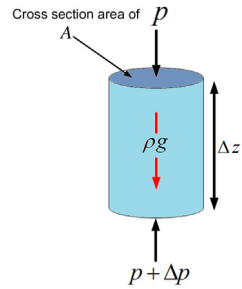

Figure 2.1 Cylinder of air with cross-sectional area *A* in hydrostatic equilibrium.

substantially in the first few kilometers near the ground, we expect the pressure to decrease by the weight of 1 km, which is about $1000 \times 1 \times 9.8 \approx 10^4$ N/m^2 (9.8 is the acceleration due to gravity) for every kilometer we go up into the atmosphere. Thus we expect a pressure drop of about 100 mb for every kilometer we rise into the atmosphere. This cannot be true at all heights because we have not accounted for the decrease in density of air with height. Before deriving the equations to allow us to do this, let us calculate the effective height of the atmosphere assuming that the density goes to zero at the top. Then the average density of the air above the surface is about 0.5 kg/m^3. The height of the column of air that gives rise to the surface pressure of 10^5 N/m^2 is $10^5/(9.8 \times 0.5) \approx 2 \times 10^4$ m = 20 km. This suggests that we expect a small fraction of the atmosphere to exist above this height.

To derive a quantitative relationship between pressure and height, we need to assume that there is a balance between gravitational and pressure forces. This assumption is generally valid at horizontal scales of tens of kilometers. However, rapid vertical motion associated with convective motion or orographic forcing can invalidate this assumption.

To analyze hydrostatic equilibrium, consider the cylinder of air shown in Fig. 2.1.

Downward force due to gravity = density of air $\times$ Volume of cylinder $\times$ $g = \rho A \Delta z g$

Upward force due to pressure = $pA - (p + \Delta p)A = -\Delta pA$

Equating the two forces, and taking the limit $\Delta z \to 0$, we obtain

$$\frac{dp}{dz} = -\rho g. \tag{2.14}$$

This is the hydrostatic equation that allows us to calculate the vertical pressure variation in the atmosphere. We can eliminate the density in the

equation using the gas law, $p = \rho R_a T$, where R_a is the gas constant of air, to obtain:

$$\frac{dp}{dz} = -\frac{gp}{R_a T}, \tag{2.15}$$

which can be integrated if we know the temperature variation with height, as follows:

$$\frac{p}{p_o} = \exp\left[-\frac{g}{R_a}\int_0^z \frac{dz}{T}\right]. \tag{2.16}$$

It is easy to calculate the pressure variation in an atmosphere, in which the temperature decreases at a constant lapse rate, γ, which is the rate at which the temperature decreases with height

$$T = T_o - \gamma z, \tag{2.17}$$

where γ can be taken to be about 6.5 K/km and T_o is the surface temperature. Substituting Eq. (2.17) into Eq. (2.16) and integrating yields

$$\frac{p}{p_o} = \left[\frac{T_o - \gamma z}{T_o}\right]^{g/R_a\gamma}. \tag{2.18}$$

Let us use Eq. (2.18) to estimate the pressure at 10 km, where the temperature is approximately $(300 - 6.5 \times 10) = 235$ K. Taking $R_a = 287$ J/(kg K), and $\gamma = 6.5$ K/km, we find

$$\frac{p}{p_o} = \left(\frac{235}{300}\right)^{g/R_a\gamma} = \left(\frac{235}{300}\right)^{5.26} = 0.277 \tag{2.19}$$

and

$$\frac{\rho}{\rho_o} = \left(\frac{235}{300}\right)^{(g/R_a\gamma)-1} = \left(\frac{235}{300}\right)^{4.26} = 0.35. \tag{2.20}$$

Thus $p \approx 277$ mb, which is consistent with measurements. The air density at this height is about $1.2 \times 0.35 = 0.42$ kg/m^3. Notice that the density falls off less rapidly than the pressure, which explains why we can use the surface density to approximate the pressure gradient below 5 km. At 20 km, the pressure works out to be about 50 mb, which means that 95% of the mass of the atmosphere is below this height.

We next use our knowledge of pressure variation in the atmosphere to define the concept of potential temperature.

THE POTENTIAL TEMPERATURE

We can define the potential temperature, θ, by considering a unit mass of dry air undergoing a change of state by moving vertically. If this parcel does not exchange heat with its surroundings, the first law of thermodynamics states

$$du + pdv = 0, \tag{2.21}$$

where u is the specific internal energy (internal energy per unit mass) and v is the specific volume. Using the perfect gas law, Eq. (2.21) can be restated as

$$\begin{aligned} &C_p\mathrm{dT} - \mathrm{vdp} = 0 \\ &\text{or} \\ &\frac{dT}{T} - \frac{R_a}{C_p}\frac{dp}{p} = 0, \end{aligned} \tag{2.22}$$

where C_p is the specific heat of air at constant pressure. This equation can be integrated to obtain

$$\theta = T\left(\frac{p_o}{p}\right)^{R_a/C_p}, \tag{2.23}$$

where θ is the temperature at p_o, a reference pressure taken to be 10^5 N/m^2, a quantity that is referred to as a **bar** in atmospheric literature. Then the potential temperature, θ, of a parcel of air at a pressure, p, and temperature, T, is defined as that achieved by the parcel when it is moved adiabatically to the reference pressure p_0. If this parcel is moved adiabatically to another pressure, its temperature changes, but its potential temperature does not change; it is a conserved quantity.

The potential temperature is a useful variable that is used to characterize energy changes in the atmosphere. Notice that by dealing with the potential temperature rather than the absolute temperature, we do not have to worry about the expansion work associated with the pressure

changes in the atmosphere. Our analysis has not included the effects of heat released during condensation of the water vapor in an air parcel.

ATMOSPHERIC STABILITY

The concept of stability can be illustrated using the motion of a ball on different surfaces, as illustrated in Fig. 2.2.

The ball in the bottom right figure is in unstable equilibrium because any small motion of the ball results in the ball moving away from its initial position in the direction of the initial push. The ball in the top middle figure is in neutral equilibrium because the motion of the ball is proportional to the push; the ball moves to its new position showing no tendency to move away. The ball in the bottom left figure has a tendency to move back to its original position when pushed in any direction; it is in stable equilibrium.

The preceding concepts on equilibrium can be extended to the motion of a parcel in an atmosphere with the three gradients of potential temperature as shown in Fig. 2.3.

The solid lines in the three figures represent profiles of potential temperature, and the shaded circles represent air parcels whose stability is being examined. Consider the middle figure, which shows the potential temperature decreasing with height. Let us a move an air parcel vertically in this atmosphere, and assume that this motion is adiabatic. This means that during this motion, the potential temperature of the parcel remains constant. The parcel's potential temperature is shown as a vertical line.

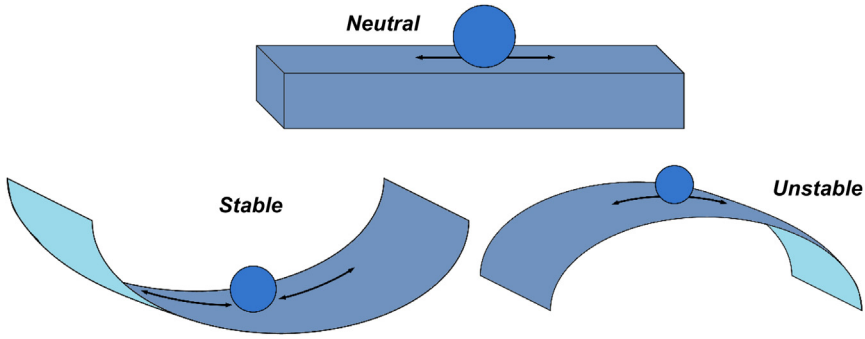

Figure 2.2 Stability of the ball's position relative to its surroundings.

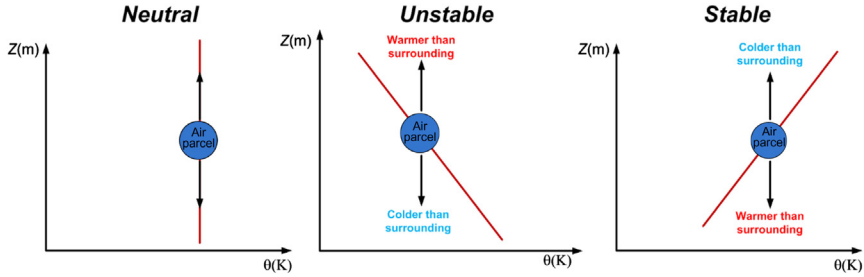

Figure 2.3 Stability of motion of air parcel relative to its surroundings.

When the air parcel is moved upwards to its new position, it is warmer and hence less dense than its surroundings. It is thus subject to an upward buoyancy force which continues to push it away from its initial position. The motion of the air parcel is also unstable when it is pushed downwards. The air parcel is denser than its surroundings, and thus continues to sink away from its initial position. We see that when the potential temperature decreases with height, the atmosphere is unstable to air motion. Any motion is amplified in such an atmosphere.

It is easy to see why an atmosphere with a constant potential temperature is indifferent to air motion. Such an atmosphere, shown in the left figure, is referred to as neutral. The right figure shows a stable atmosphere, which resists vertical motion. If a parcel is moved upwards, it is denser than its surroundings and falls back to its original position. When moved downwards, the parcel is lighter than the surrounding atmosphere, and thus rises back to its original position.

The atmosphere will tend to neutral conditions when it undergoes vertical mixing. It is only when the potential temperature is constant that further mixing does not lead to change in the temperature.

Note that when the potential temperature is constant, the actual temperature decreases with height at the adiabatic lapse rate. It is easy to calculate the temperature decrease in a layer with constant potential temperature as follows. We can use Eq. (2.23), and the hydrostatic balance to derive the relationship between the vertical gradients of the potential temperature and the absolute. Differentiating Eq. (2.23) with respect to z yields

$$\frac{1}{\theta}\frac{d\theta}{dz} = \frac{1}{T}\frac{dT}{dz} - \frac{R_a}{C_p}\frac{1}{p}\frac{dp}{dz}. \tag{2.24}$$

Using Eq. (2.15) to eliminate the vertical pressure gradient, we find

$$\frac{d\theta}{dz} = \frac{\theta}{T}\left[\frac{dT}{dz} + \frac{g}{C_p}\right]. \tag{2.25}$$

Because $\theta/T \cong 1$, we can calculate the potential temperature gradient from

$$\frac{d\theta}{dz} \cong \frac{dT}{dz} + \frac{g}{C_p}. \tag{2.26}$$

If the potential temperature is constant, Eq. (2.26) implies that

$$\frac{dT}{dz} = -\frac{g}{C_p}. \tag{2.27}$$

This temperature decrease with height is called the adiabatic lapse rate, whose value can be readily worked out to be

$$\frac{dT}{dz} = -\frac{g}{C_p} = -\frac{9.81\ m/s^2}{1000\ J/(\mathrm{kg\ K})} \cong -\frac{10}{1000} K/m. \tag{2.28}$$

So if the temperature in the atmosphere decreases faster than the adiabatic lapse rate, the atmosphere is unstable. If the temperature decrease is less than the adiabatic lapse rate, the atmosphere is stable.

When the potential temperature is constant through a layer, the layer is well mixed in the sense that in the absence of external heat input there can be no changes in the potential temperature. To see this, imagine moving an air parcel from one height to another. Initially because its temperature is the same as its surroundings, there is no heat transfer into the air parcel. Any motion does not change this situation because one can imagine this motion to consist of steps in which the parcel is moved adiabatically, and then allowed to come to equilibrium with its surroundings. In its new location, the parcel has exactly the same temperature as its surroundings because adiabatic motion of the parcel does not change the potential temperature, which is identical to the potential temperature of its surroundings. If the potential temperatures are equal, so are the actual temperatures, and there is no heat transfer, and hence no change in the potential temperature of the parcel or its surroundings.

Notice that when we lift a parcel adiabatically, or if a layer is well mixed, the temperature decreases with height. It is this decrease in temperature that leads to the condensation of vapor in moist air parcels, and hence the formation of clouds. However, this condensation results in

the heating of the parcel, and the temperature decrease is smaller than the dry adiabatic lapse rate. The rate of decrease in temperature of the saturated parcel, referred to as the wet adiabatic lapse rate, γ_w, is always smaller than the dry adiabatic lapse rate, γ_d. This makes physical sense because the heat released during condensation of the water vapor has to decrease the rate at which the temperature decreases during dry conditions.

THE ORIGIN OF LARGE-SCALE WINDS

The winds that carry the pollution away from their sources are initiated by the differential heating of the Earth's surface by solar radiation. The intensity of solar radiation is highest near the equator, and becomes small near the poles. This difference in radiation translates into temperature differences at the ground, which in turn give rise to large-scale convective motion. Once initiated, this motion is governed by several forces that determine the subsequent evolution of the wind. These forces of most importance to large-scale motion are (1) the pressure gradient force, (2) the Coriolis force, and (3) the frictional force. Let us consider each of them in turn.

The Pressure Gradient Force

The vertical pressure gradient is proportional to the local air density:

$$\frac{dp}{dz} = -\rho g. \tag{2.29}$$

Eq. (2.29) tells us that the rate at which the pressure decreases with height increases with density. This means that the pressure falls off faster in a cold (dense) atmosphere than in a warm atmosphere. Let us use this observation to determine the role of differential heating in generating large-scale winds.

Assume that the Earth as represented in Fig. 2.4:

In the figure, the air is warm over the equator and cold over the North Pole. We assume that the surface pressures at equator and North Pole are the same. As discussed earlier, the pressure decreases with height more rapidly in the cold (dense) air than in the warm air. This means that

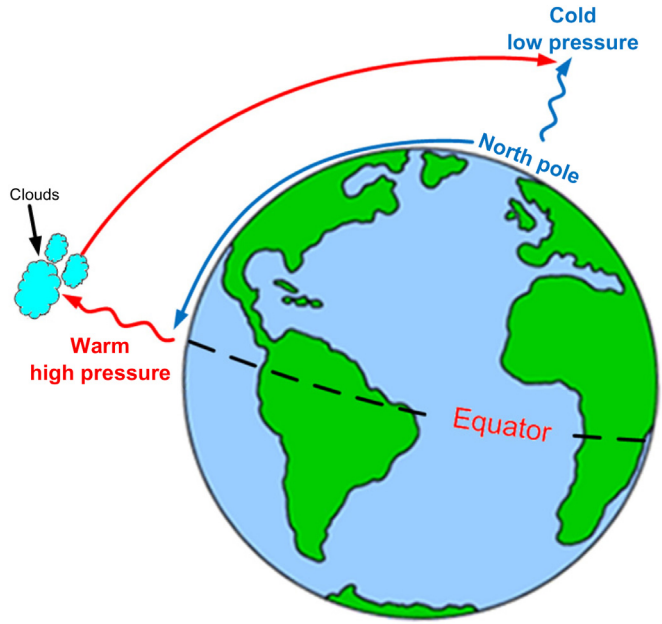

Figure 2.4 Representation of Earth's surface to relate temperature gradients to pressure gradients.

at all heights above the surface; the pressure over the equator is higher than that over the pole at the same height over the Earth's surface. The pressure at High pressure is greater than that at Low pressure, which results in a horizontal pressure gradient that drives the air toward the north. This flow is compensated by flow from the north to the south at the surface. There is rising motion over the equator, and descending motion over the North Pole to complete the convective circulation pattern. In the absence of the Earth's rotation, we would expect to see such a pattern. However, the Earth does rotate, and the circulation pattern is considerably more complicated than this picture.

As the air flows toward the north, the Earth's rotation causes it to turn toward the west. This turning is caused by the Coriolis force, which is a pseudo force that we need to invoke in a rotating frame of reference. The Coriolis force also deflects the southward moving flow toward the east. This general pattern of circulation is seen in cells near the equator, and near the poles. However, in mid-latitudes between 40° and 60°, the flow is much less organized in the vertical. The large-scale flow is westerly

(from the west), and superimposed on this flow are structures referred to as cyclones and anticyclones. These structures are responsible for the weather we see in the mid-latitudes. In this chapter, we will not discuss weather patterns in any great detail. We will confine our attention to the underlying forces that determine air motion. We have already discussed the pressure gradient force. The next section discusses the Coriolis force.

The Coriolis Force

To understand the origin of the Coriolis force, imagine conducting the following experiment with a turntable. Joe is on the rotating turntable shooting beads along the *X*-axis, which is rotating with him. The situation is shown in Fig. 2.5.

If the beads are shot out from the center of the turntable, they would have no tangential velocity and thus move along their original *X*-direction as shown in the figure. This is what, Moe, the stationary observer expects; the successive positions of one of these beads are shown as **A** and **B**. On the other hand, Joe, on the turntable, thinks that the bead ought to be at positions **A**′ and **B**′. Because the bead is observed to be at **A** and **B**, Joe has to invent a force, called the Coriolis force, that forces the beads to their right as they move along Joe's *X*-axis.

We can derive an expression for the Coriolis acceleration by assuming that the beads are forced to move along the *X*-axis in Joe's rotating coordinate system; assume that the beads move along a wire stretched out along the radius, as shown in Fig. 2.6. Then in order for us to keep the beads from deflecting to the right, we need to apply a Coriolis force to the left.

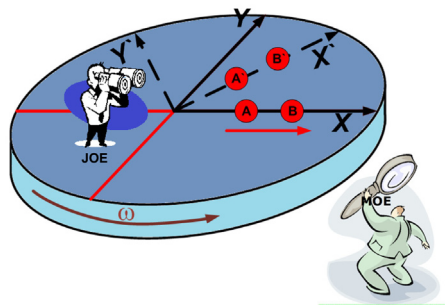

Figure 2.5 Motion of a ball on a turntable as viewed by two different observers.

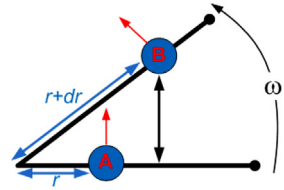

Figure 2.6 Motion of a ball along a wire on a rotating turntable.

Let us calculate the magnitude of the associated Coriolis acceleration by examining the distance traveled by the bead over a small time interval.

Assume that the turntable rotates anticlockwise over a small time interval Δt. If the angular velocity of rotation is ω, the corresponding angle through which the X-axis rotates is $\omega\Delta t$. Now the tangential velocity at position A is ωr. To calculate the Coriolis acceleration, let us use the expression for the distance traveled in the tangential direction:

$$s = ut + \frac{1}{2}at^2, \tag{2.30}$$

where u is the initial velocity and a is the acceleration. Now

$$s = \omega(r + \Delta r)\Delta t$$

where (2.31)

$$\Delta r = v_r \Delta t$$

and v_r is the radial velocity. Substituting Eq. (2.31) into Eq. (2.30), and using $u = \omega r$, we find that the Coriolis acceleration is

$$a_c = 2v_r\omega. \tag{2.32}$$

It turns out that the Coriolis acceleration does not depend on the particle (or bead) traveling radially. The velocity, v_r, can be in any direction on the plane that is normal to the vector of rotation, $\vec{\omega}$. The acceleration is normal to the velocity vector, $v_r^{\rightarrow}$, and when $a_c^{\rightarrow}$ is rotated toward $v_r^{\rightarrow}$, a right handed screw will point toward $\vec{\omega}$.

On the Earth, the rotation rate is a maximum at the pole, and decreases with the latitude as shown in Fig. 2.7

If the rotation rate is ω at the pole, the rotation rate of the plane parallel to the Earth's surface at a latitude, λ, is $\omega\sin\lambda$, and the Coriolis acceleration of a particle moving with a velocity v_r on the plane is

$$a_c = 2v_r\omega \sin\lambda. \tag{2.33}$$

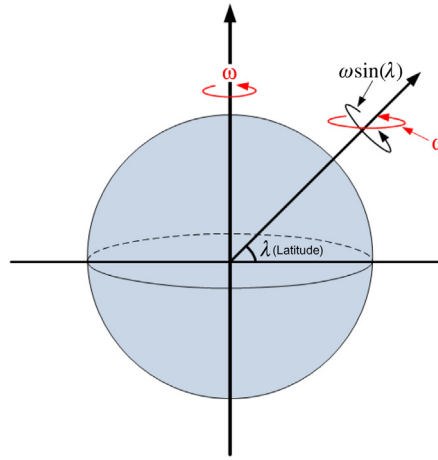

Figure 2.7 Rotation of the Earth as a function of latitude.

In the atmospheric literature, we define the Coriolis parameter, f, as follows

$$f = 2\omega \sin\lambda. \tag{2.34}$$

Notice that f has the units of inverse time. Its inverse $1/f$ is an important time scale that governs several atmospheric phenomena, including the dynamics of the atmospheric boundary layer. We will discuss this briefly in a later section. The magnitude of f at latitude of 45° is given by

$$f = 2 \times \frac{2\pi}{24\ \text{h} \times 3600\ s/h} \sin(45) \cong 1 \times 10^{-4}\ \text{s}^{-1}. \tag{2.35}$$

The next section discusses the winds created by the balance between the pressure gradient force and the Coriolis force.

THE GEOSTROPHIC WIND

We saw earlier that the pressure gradient force generates air motion from a region of high pressure to that of low pressure. As the air accelerates toward the region of low pressure, it is subject to the Coriolis force, which in the northern hemisphere, deflects the wind to the right. This is depicted in Fig. 2.8.

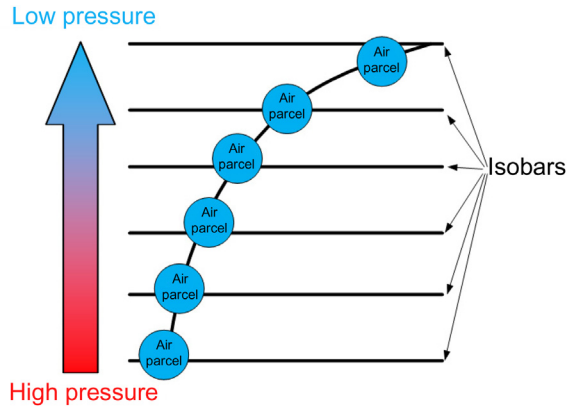

Figure 2.8 Deflection of moving air parcel by Coriolis force.

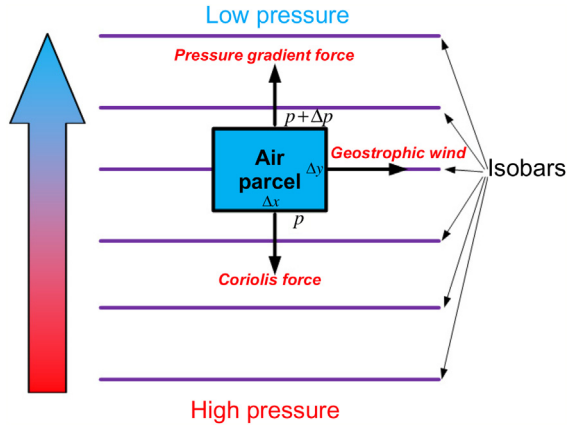

Figure 2.9 Balance between pressure gradient force and Coriolis force to produce the geostrophic wind.

The horizontal lines represent regions of equal pressure at some height above the ground; these lines are called isobars. As the air parcel moves from high pressure to low pressure, it is deflected to the right by the Coriolis force. Over long-time scales, the pressure gradient and the Coriolis forces reach a state of balance, and the wind corresponding to this balance is referred to as the geostrophic wind.

We can derive an expression for the geostrophic wind, V_g, using Fig. 2.9.

Consider an air parcel with dimensions Δx and Δy, and unit depth. Take the density of the air parcel to be ρ. Then the Coriolis force acting downwards is given by

$$\text{Coriolis Force} = f\rho(\Delta x \Delta y) V_g. \tag{2.36}$$

The pressure gradient force acting upwards is given by:

$$\begin{aligned} \text{Pressure gradient force} &= [p - (p + \Delta p)]\Delta x \\ &= -\Delta p \Delta x \end{aligned}. \tag{2.37}$$

Equating the two forces gives us the required expression for the geostrophic wind:

$$V_g = -\frac{1}{\rho f}\frac{\Delta p}{\Delta y}. \tag{2.38}$$

Eq. (2.38) provides useful estimates of the winds at several kilometers above the ground. The equation tells us that horizontal pressure gradients are associated with winds. We can estimate the magnitude of these pressure gradients by taking

$$\begin{gathered} V_g = 10\ m/s \\ \rho = 1\ \text{kg}/m^3 \\ f = 10^{-4}\ \text{s}^{-1} \\ \Delta y = 100\ \text{km} \end{gathered}$$

Then Eq. (2.38) yields

$$\begin{aligned} \Delta p &= -10\ m/s \times 1\ \text{kg}/m^3 \times 10^{-4}\ \text{s}^{-1} \times 100\ \text{km} \times 1000\ m/\text{km} \\ &= 100\ N/m^2 = 1\ \text{mb} \end{aligned}. \tag{2.39}$$

We see that horizontal pressure gradients are of the order of a few mb over 100 km. In contrast, vertical pressure gradients are of the order of 100 mb over 1 km.

Because horizontal winds are associated with pressure gradients, it is often possible to infer the magnitude of winds from maps of pressures. The fact that upper air winds are approximately Geostrophic suggests Guy Ballot's Law: if the wind is at your back, the high pressure is on your right in the northern hemisphere.

Most weather maps usually show surface isobars, which appear as patterns of high and low pressures. These patterns, which are examined in the next section, are important indicators of weather.

HIGH- AND LOW-PRESSURE CENTERS

Large-scale disturbances in the upper atmosphere lead to the formation of localized high- and low-pressure regions, which are commonly referred to as highs and lows. High-pressure regions are associated with large-scale descending motion or subsidence, which leads to compressive heating of the air and the formation of regions in which the temperature increases with height. As we saw earlier, these temperature inversions resist vertical motion, and can thus act as lids to vertical dispersion of pollution. Because descending motion prevents the formation of clouds, highs are associated with clear skies with warm temperatures. Such conditions are conducive to the formation of smog.

Low-pressure regions are associated with large-scale ascending motion of air. This leads to the formation of clouds, which in turn can lead to rain. The formation of clouds is accompanied by condensation and hence heating, which, in turn, can lead to further buoyancy-induced vertical motion. Thus air motion in lows is unstable because of this positive feedback between vertical motion and cloud formation. Weather in lows is generally inclement. It is easy to see that one does not expect air pollution buildup in low-pressure regions.

Low-pressure regions are referred to as cyclones because the air motion around them is **cyclonic**, or in the same direction as the Earth's rotation; this rotation is anticlockwise in the northern hemisphere. High-pressure regions are referred to as anticyclones because the flow around them is clockwise. To understand the direction of flows around highs and lows, we need to examine the forces affecting these flows. Let us first consider the flow around a high-pressure region, as shown in Fig. 2.10.

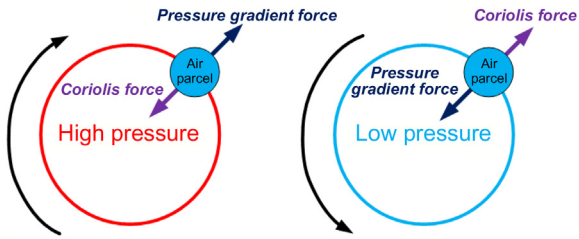

Figure 2.10 Flow around high- and low-pressure centers.

The figure shows an air parcel in the flow around a high-pressure center. The pressure gradient force is outward, while the Coriolis force is directed toward the center of the high. The Coriolis force has to be greater than the pressure gradient force to provide the net inward force to keep the air parcel circulating around the center of the high. If the flow was anticlockwise, both the Coriolis and the pressure gradient forces would be directed outward, and flow around the center would not be possible.

Now consider the flow around a low or cyclone. Here the flow is counterclockwise, with the difference between the inward pressure gradient force and the outward Coriolis force providing the force to keep the air parcel moving around the low. In principle, the flow around the low can be clockwise because both the Coriolis and the pressure gradient forces can add to provide the required inward force. However, such a flow is unusual because the flow around the low originates from winds that are initially in geostrophic balance: the Coriolis force opposes the pressure gradient force. The anticlockwise flow around a low maintains this relationship between the two forces.

The majority of the cyclones and anticyclones are migratory in the sense that they are formed in different parts of the Earth and then move with the large-scale winds until they are dissipated. However, some of these systems are semipermanent because they are associated with the global circulation pattern setup by differential heating of the Earth's surface. The weather in Los Angeles is governed by semipermanent anticyclone associated with the descending region of the **Hadley** cell extending from the equator to about 30°N and S latitudes. This high-pressure center causes the generally good weather marked by the lack of clouds and rain during most of the year. The winter rains occur when the high-pressure region move southwards during winter. The undesirable effect of warm temperatures is the smog that forms when pollutants react under sunny, light wind conditions. Therefore we can blame part of our air pollution problems on weather.

The flows around highs and lows are not parallel to the isobars because of the effects of friction. The wind is directed into the low, and away from the high; there is low-level convergence into a low-pressure region, and divergence at low levels of a high. These modifications by friction are treated in the next section.

EFFECTS OF FRICTION

Friction refers to processes that decrease the wind that would exist under geostrophic balance. The slowing down is caused by the transfer of vertical momentum from upper layers of the atmosphere to lower layers by turbulence. Because the horizontal velocity at the ground has to be zero, any transfer of momentum will lead to reduction of the geostrophic velocity (Fig. 2.11).

We can examine the effects of friction by first assuming that the flow is initially geostrophic, so that the pressure gradient force is balanced by the Coriolis force. When friction slows the velocity, the Coriolis force, $\boldsymbol{F}$, decreases because it decreases with the velocity. The pressure gradient force, $\boldsymbol{P}$, is now greater than the Coriolis force, and the wind is deflected toward lower pressure until a new state of force balance is reached. This is illustrated in Fig. 2.11.

We can determine the cross-isobaric angle, θ, by performing a force balance on the air parcel. We find

$$\begin{aligned} &F\cos\theta = C\sin\theta \\ &\text{and} \qquad\qquad . \\ &F\sin\theta + C\cos\theta = P \end{aligned} \tag{2.40}$$

Eq. (2.40) allows us to solve for the two unknowns, θ and the horizontal velocity, v_H, if we know the relationship between the frictional force, F, and v_H.

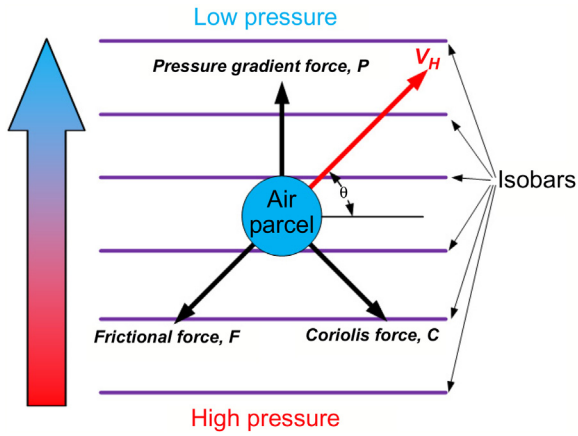

Figure 2.11 Turning of the wind by frictional forces.

Notice that the cross-isobaric angle increases with the frictional force, which means that it has its largest value close to ground, and decreases as we go up in height. Another way of saying this is that the wind rotates clockwise as the height increases. The clockwise rotation and the accompanying increase of velocity is commonly referred to as the Ekman spiral in honor of the German meteorologist, Ekman.

The frictionally induced flow across isobars also occurs in high- and low-pressure centers. The wind flows into a low and away from a high. This is consistent with the low-level convergence and diverge required to maintain lows and highs.

FRONTS

This section provides a very brief description of the phenomena of fronts, which play a major role in determining our weather. Fronts represent the boundaries between air masses with markedly different characteristics, especially temperature. These air masses acquire their properties by moving slowly or stagnating over different regions of the Earth's surface. For example, a large mass of cold air can form by southward moving air that spends a long period of time over the continents that are cold during winter. Similarly, a warm air mass can form in air originating from equatorial regions, and then moving slowly over the warm oceans.

The boundary between the cold and warm air masses is referred to as a front, a name that is associated with the time, the Second World War, during which the phenomena was first discovered and studied. The role of these fronts in determining weather in the mid-latitudes was first suggested by a group of Norwegian meteorologists, who likened the activity at the boundaries between warm and cold air masses to the fronts of advancing and retreating armies.

The weather associated with a front is caused by lateral motion along the boundary between the cold and warm air masses. The usual pattern of motion resembles a wave, which is illustrated in Fig. 2.12.

On the left side of the wave, the cold air mass pushes southward along the cold front, while the warm air pursues the retreating cold air along the warm front. A low-pressure center is located at the crest of the wave,

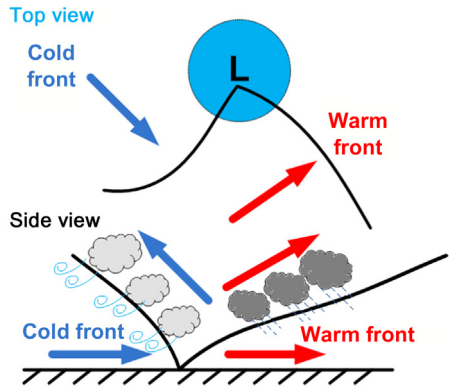

Figure 2.12 Schematic representation of warm and cold fronts.

and as described earlier, the flow around it is cyclonic. At the fronts, the warm air rides over the denser cold air mass. The vertical motion of the warm, usually moist, air at the fronts, results in the formation of clouds and hence rain. The advancing cold front forces the warm air vertically, which results in the formation of clouds and rain at the front. The retreating warm front is shallower than the cold front is, and the vertical motion of the overriding warm is less intense than at the cold front. The weather is generally more unstable at the cold front than at the warm front. Thunderstorms usually occur at the cold front; at the warm front, the more gradual upward motion results in precipitation that is usually light and continuous, but it occurs over a larger area than at the cold front.

The slopes of the fronts are of the order 1 in 100: the vertical scale is of the order of kilometers, while the horizontal scale is of the order of hundreds of kilometers. The weather pattern associated with the passage of the frontal system can be understood by placing yourself on the right of the warm front. As the pattern moves from left to right, you will first notice clouds that are layered in appearance, and whose bases are about 3 km; these are associated with the gentle vertical motion along the retreating warm front. Steady rain will start falling when the warm front is several hundred kilometers from you. This will be accompanied by falling pressure. As the front approaches you, the clouds will start to thicken, and the rain will become heavier and more intermittent, and the cloud bases will become lower signaling the approach of the warm air.

You can see from Fig. 2.12, that as the warm front passes you, the wind direction at the surface will shift from the south, southeast, to

southwest. The temperature will rise, and the precipitation will disappear. Within 24 h, the cold front will approach, and it will signal its presence through rapidly falling pressures and deepening clouds. The passage of the leading edge of the cold front will be accompanied by a rapid change in the wind direction to the northwest, rising pressure, and showers and thunderstorms associated with deep clouds. These rains will last for a few hours until you are in the cold air mass behind the front. The weather now is cold and crisp, and the air is usually clear.

This chapter provides the preliminaries required for a detailed discussion of the processes within the atmospheric boundary layer, which are described in Chapter 3, Fundamentals of Micrometeorology and Dispersion.

CHAPTER THREE

Fundamentals of Micrometeorology and Dispersion

Contents

Introduction 39
Surface Energy Balance—Atmospheric Boundary Layer 40
Turbulence in the Atmospheric Boundary Layer 42
  Convective Velocity Scale 44
Friction Velocity 46
Monin–Obukhov Length 47
  Surface Layer Similarity 47
The Daytime Boundary Layer 50
  Height of the Convective Boundary Layer 52
The Nighttime Boundary Layer 54
  Turbulent Velocities in the Stable Boundary Layer 57
  Dispersion Modeling—Ground-Level Source 58
The Point Source in the Atmospheric Boundary Layer 60
Dispersion in the Atmospheric Boundary Layer 61
  Plume Spread Formulation Used in Current Models 67
  The Unstable Surface Boundary Layer 69
  The Stable Surface Boundary Layer 70
  Horizontal Spread in the Surface Boundary Layer 72
Concluding Remarks 74
References 74
Further Reading 75

INTRODUCTION

This chapter provides the background in the physics of the atmospheric boundary layer that is required to understand transport and dispersion of pollutants associated with the transportation sector. This is followed by an examination of the processes that govern transport and dispersion. We then introduce the models that are used to represent the

Urban Transportation and Air Pollution.
DOI: https://doi.org/10.1016/B978-0-12-811506-0.00003-8

processes. In Chapter 4, The Impact of Highways on Urban Air Quality, we go into the details of these models.

SURFACE ENERGY BALANCE—ATMOSPHERIC BOUNDARY LAYER

The atmospheric boundary layer refers to the layer next to the ground that is governed by heat and mass transfer from the earth's surface to the overlying atmosphere. The dynamics of the atmospheric boundary layer is governed by the input of energy from the ground into the boundary layer. The ultimate source of this energy is the sun that supplies the solar radiation to the ground. Solar radiation from the sun provides the energy to generate both the winds and the turbulence in the atmospheric boundary layer. The mean radiant flux outside the earth's atmosphere normal to the solar beam is about 1350 W/m^2, most of which lies at wavelengths below 4 μm. Ozone and oxygen in the upper atmosphere absorb most of the energy below 0.3 μm, which accounts for about 3% of the total solar energy. A further 17% is absorbed by water vapor and scattered by particles in the atmosphere, so that about 80% of the radiation incident on the earth's atmosphere reaches the earth's surface. This situation is altered considerably in the presence of clouds, which can scatter most of the energy in the direct beam of solar radiation. Part of this scattered energy goes back into space, while the rest is directed toward the earth. The scattered radiation is referred to as the diffuse component of the solar radiation.

Part of the solar radiation reaching the ground is reflected, and part of it is absorbed. The absorbed solar radiation is converted into other forms through an energy balance at the ground. The components of the energy balance are shown in Fig. 3.1.

Notice that the radiative input to the surface has been separated into solar and thermal radiation. Solar radiation refers to the wavelength region corresponding to the radiation from the sun, whose effective blackbody temperature is close to 6000 K. Most of the solar energy lies in the wavelength region $0 \leq \lambda \leq 4$ μm, with the peak of spectrum at around 0.5 μm.

Thermal radiation refers to energy emitted at temperatures typical of the earth's surface, about 300 K. The energy lies in the region

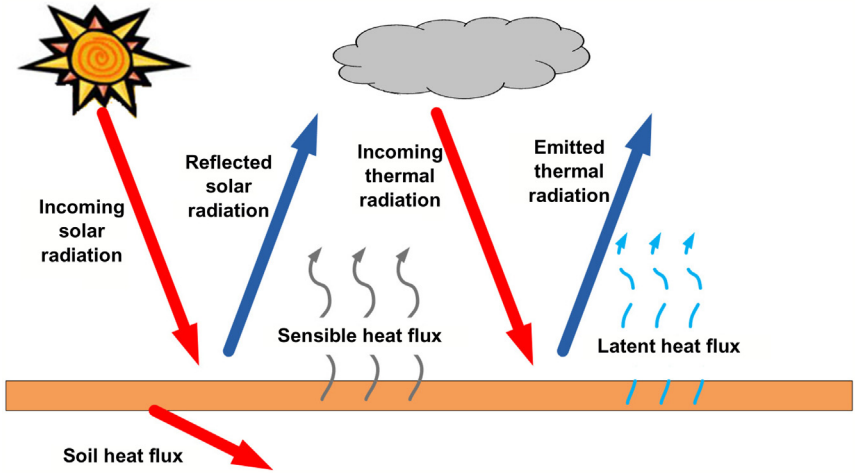

Figure 3.1 The surface energy balance.

$4 \leq \lambda \leq 100\ \mu m$, with the peak of the spectrum at about $10\ \mu m$. The incoming thermal radiation refers to that emitted by the component gases of the atmosphere, such as water vapor and carbon dioxide, and other so-called greenhouse gases. The outgoing thermal radiation is the energy emitted by the ground. Because the ground is usually warmer than the atmosphere, the outgoing thermal radiation usually exceeds the incoming thermal radiation.

The sensible heat flux is the energy flux from the atmosphere to the ground because of temperature differences between the ground and the atmosphere. During the daytime, energy flows away from the ground into the atmospheric boundary layer, while during the night the boundary layer supplies energy to the ground.

The latent heat flux refers to the energy used to evaporate moisture from the ground. The soil heat flux refers to the energy that is supplied to the ground, and which ultimately determines the temperature of the soil layer.

We are now in a position to write the energy flux balance at the interface between the atmospheric boundary layer and the soil. The surface energy balance reads:

$$R_N = H + L + G, \tag{3.1}$$

where R_N is the net radiation, which is the difference between the solar radiation absorbed at the surface and the net thermal radiation emitted by

the surface. H is the sensible heat flux supplied to the boundary layer, L is the latent heat flux related to the evaporation of water from the surface, and G is the heat flux into the soil.

During the day, H is usually greater than zero, i.e., heat is supplied to the atmosphere. During the night, H is less than zero, i.e., heat is drawn from the atmosphere and the ground to support the cooling of the ground as R_N becomes negative. The cooling can be inhibited in the presence of clouds which radiate energy toward the ground.

When the ground is moist, most of the incoming radiation can go toward evaporation. An approximate method of accounting for energy going into evaporation is to assume that the ratio of latent heat flux to sensible heat flux is a number, referred to as the Bowen ratio, that depends only on the type of surface being considered. Some commonly used methods to calculate the components of the surface energy balance are described in Van Ulden and Holtslag (1985).

TURBULENCE IN THE ATMOSPHERIC BOUNDARY LAYER

Turbulence is the term applied to atmospheric motion that is so complex that it does not allow for a deterministic description from a practical point of view; we have to be satisfied with understanding the statistical properties of the flow. Turbulent flows occur when the inertial forces acting on the fluid are much greater than the stabilizing viscous forces. The Reynolds number is a measure of the ratio of these two forces. It is defined by

$$\mathrm{Re} = \frac{ud}{\nu}, \tag{3.2}$$

where u is the mean velocity of the flow, d is the length scale of the flow (e.g., the diameter of the pipe through which the fluid is flowing), and ν is the kinematic viscosity of the fluid. For air, $\nu = 15 \times 10^{-6}\ \mathrm{m^2/s}$. Turbulent flows are characterized by Reynolds numbers much greater than 1000. Fig. 3.2 shows the time variation of the horizontal velocity measured in turbulent flow.

It is common practice to study turbulence using either time averages or something called ensemble averages, which we will not discuss here. If we assume that the flow is steady in the sense that time averages converge

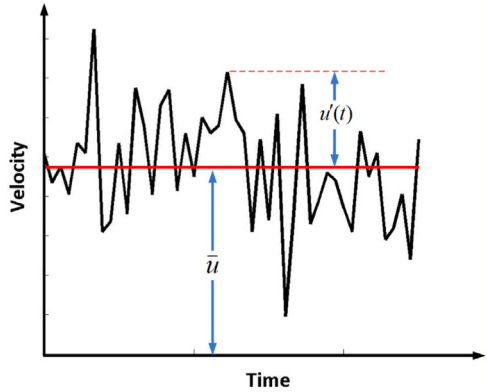

Figure 3.2 Time variation of the horizontal velocity measured in turbulent flow.

to specific values when the averaging time is long enough, we can always write the instantaneous velocity, $\tilde{u}(t)$, as follows:

$$\tilde{u}(t) = U + u(t), \tag{3.3}$$

where U is the time average or mean defined by

$$U = \underset{T\to\infty}{Lim}\ \frac{1}{T}\int_0^T \tilde{u}(t)dt, \tag{3.4}$$

and $u(t)$ is the fluctuating component. In our notation, upper case letters refer to mean quantities, and lower case refers to turbulent fluctuations. By convention, the horizontal components of the velocity are denoted by u and v, and the vertical component by w.

The study of turbulence involves understanding the mean, and the statistics of the turbulent quantities under a variety of conditions. The statistic of greatest relevance to dispersion of pollution is the standard deviation of the fluctuating velocity defined by

$$\sigma_u = \left[\underset{T\to\infty}{Lim}\ \frac{1}{T}\int_0^T u^2 dt\right]^{1/2}. \tag{3.5}$$

Notice that, by definition, the time averages of the fluctuating quantities are zero. However, the average of the product of two fluctuating quantities is not zero.

Turbulence in the atmospheric boundary layer is generated by wind shear and buoyancy associated with sensible heating at the ground.

During the daytime, sensible heating at the surface results in parcels of air that are warmer, and hence less dense than their surroundings. These parcels are subject to buoyancy forces that accelerate them upward.

Turbulence in the boundary layer is also created by shear, which is the motion of a layer of air sliding past another layer with a different velocity. This leads to vertical turbulent motion that transfers momentum between these layers. This is essentially the mechanism that slows down the air as it flows past a stationary surface; momentum is transferred to the ground because the velocity increases with height near the ground.

The velocity time series, such as the one shown in Fig. 3.2, suggests that turbulent motion can be considered to consist of the superposition of the motion of turbulent "eddies" with a range of time and length scales. Turbulent energy is supplied by the mean flow, transferred from the large to the small eddies, and is ultimately dissipated through molecular viscosity at the smallest scales of motion.

In understanding the role of turbulence, it is useful to think of turbulent motion at a particular height in the boundary layer as dominated by an eddy with a length, l, and a velocity w. Then, its overturning timescale is l/w. The magnitude of the velocity scale in any particular direction is of the order of the standard deviation of the corresponding velocity fluctuations. The combination wl is called the eddy diffusivity of turbulence, K. It turns out that under certain circumstances, the eddy diffusivity can be used to estimate the turbulent flux, F_i, of a quantity ϕ using the gradient formula $F_i = -K_i \frac{\partial \phi}{\partial x_i}$, where i denotes a specific direction.

We can estimate the magnitude of the turbulent velocities generated by these two mechanisms, buoyancy and shear, using simple models.

Convective Velocity Scale

As mentioned earlier, heat flux from the ground to the atmosphere creates buoyancy forces, which in turn generate turbulent velocities. We can estimate these turbulent velocities by considering an air parcel of unit mass that has a temperature excess of ΔT over its surroundings that it acquires at the heated ground. Taking the specific volume (volume per unit mass) of the parcel as v, the two forces on the parcel (neglecting drag forces for the moment) are

$$\text{Downward gravitational force} = g. \tag{3.6a}$$

$$\text{Upward buoyancy force} = vg\rho_s, \tag{3.6b}$$

where the subscript "s" refers to surroundings. Then, the net upward force is

$$F_u = v g \rho_s - g = g(v\rho_s - 1), \tag{3.7}$$

where ρ_s is the density of the surroundings.

But

$$v = 1/\rho, \tag{3.8}$$

so that

$$F_u = g\left(\frac{\rho_s}{\rho} - 1\right) = g\left(\frac{T}{T_s} - 1\right) \text{ (from the gas law)} \tag{3.9}$$

or

$$F_u = g\frac{\Delta T}{T_s} \cong g\frac{\Delta\theta}{\theta_s}. \tag{3.10}$$

This force, acting over a distance z, generates a kinetic energy $\approx w^2$ so that

$$\frac{g\Delta\theta z}{\theta_s} \approx w^2. \tag{3.11}$$

Now let us multiply both sides of the equation by w,

$$\frac{g(\Delta\theta w)z}{\theta_s} \approx w^3. \tag{3.12}$$

The term inside the parentheses in Eq. (3.12) is the velocity of the parcel multiplied by the temperature excess carried by the parcel. This quantity is proportional to the surface heat flux:

$$\Delta\theta w \sim \frac{H}{\rho C_p}. \tag{3.13}$$

Then,

$$w \approx \left(\frac{g}{\theta_s}\frac{H}{\rho C_p}z\right)^{1/3}. \tag{3.14}$$

$H/\rho C_p$ is referred to as the kinematic heat flux, and is denoted by

$$\frac{H}{\rho C_p} = Q_0. \tag{3.15}$$

Now, define a *free convection scale*, u_f:

$$u_f = \left(\frac{g}{T_0} Q_0 z\right)^{1/3}. \tag{3.16}$$

where T_0 is the near surface temperature which is approximately equal to θ_s in a well-mixed convective boundary layer.

Another velocity scale that is used to characterize a boundary layer dominated by surface heating is the *convective velocity scale* given by

$$w_* = \left(\frac{g}{T_0} Q_0 z_i\right)^{1/3}, \tag{3.17}$$

where z_i is the boundary layer height, which is also called the mixed layer because vertical motion induced by buoyancy leads to vigorous vertical mixing of the properties of the boundary layer.

FRICTION VELOCITY

Except very close to the ground, the horizontal shear stress is supported by macroscopic turbulent motion. When parcels of air travel vertically, they exchange momentum between layers of air with different velocities. Vertical gradients in horizontal mean velocity lead to changes in instantaneous horizontal velocities during this transfer of momentum. If we denote the horizontal velocity fluctuation, u', created by a parcel of air with vertical velocity, w', the horizontal momentum transferred across a horizontal layer by the parcel is $\rho u'w'$, where ρ is the air density. If the horizontal shear stress is roughly constant with height and is equal to the surface stress, τ_0, then $\tau_0 = -\rho\overline{u'w'}$, where the overbar denotes a time average. The negative sign ensures that τ_0 is positive because a positive w' is associated with a negative u' when the mean horizontal velocity increases with height. These arguments suggest that the turbulent velocities associated with shear production of turbulence scale with the surface friction velocity, u_*, defined by

$$u_* \equiv \sqrt{\frac{\tau_0}{\rho}}. \tag{3.18}$$

Buoyant and shear production of turbulence operate together to determine the structure of the boundary layer. A length scale, referred to

as the Monin–Obukhov length, allows us to combine the effects of these mechanisms into a single framework that describes the vertical structure of the near surface atmospheric boundary layer.

MONIN–OBUKHOV LENGTH

The absolute value of the Monin–Obukhov length, L, is roughly the height at which the turbulent velocity generated by shear is equal to that produced by buoyancy:

$$u_* \sim u_f(z = L) = \left(\frac{g}{T_0} Q_0 L\right)^{1/3} \tag{3.19}$$

which yields the definition

$$L = -\frac{T_0 u_*^3}{gkQ_0}, \tag{3.20}$$

where the von Karman constant $k = 0.4$. The negative sign indicates that when Q_0 is positive during the day, L is negative and positive when the heat flux is toward the ground. So L is positive when the boundary layer is stable, and negative when it is unstable.

Notice from Eq. (3.16) that the velocity associated with buoyancy production of turbulence increases with height. On the other hand, the velocity associated with shear production is more or less constant in the surface layer. This allows us interpret the meaning of the Monin–Obukhov length, L. Shear production of turbulence dominates that by buoyancy at heights below the Monin–Obukhov length, while buoyant production becomes dominant above it.

Surface Layer Similarity

At heights below the order of magnitude of the Monin–Obukhov length, the mean and the turbulent structure of the boundary layer can be described using Monin–Obukhov similarity theory (Businger, 1973). The theory states that the mean temperature and velocity gradients can be represented by universal functions if the velocity, temperature, and height are scaled appropriately. The velocity scale is u_*, the height scale is L, and the temperature scale, θ_*, is given by

$$\theta_* = -\frac{Q_0}{u_*}. \tag{3.21}$$

Let us consider a neutral boundary layer, one that is dominated by shear. In such a boundary layer, the mean velocity gradient is of the same order as the velocity gradient across the dominant turbulent eddy at that height. We assume that the dominant eddy at a height z has a length scale of order z and a velocity scale of order u_*. Then, measurements indicate that we can write

$$\frac{dU}{dz} = \frac{u_*}{kz}, \tag{3.22}$$

where $k = 0.4$ is the von Karman constant. Integration yields the logarithmic expression for the mean wind speed at height z,

$$U(z) = \frac{u_*}{k}\ln\left(\frac{z}{z_0}\right), \tag{3.23}$$

where z_0 is the roughness length. The roughness length is related to the physical dimensions of the objects at the surface. Details on how this is estimated can be found in textbooks on micrometeorology, such as that by Stull (1988).

Monin–Obukhov Similarity theory states that we can account for the effects of heat flux by modifying Eq. (3.23) as follows:

$$\frac{dU}{dz} = \frac{u_*}{kz}\phi_m\left(\frac{z}{L}\right), \tag{3.24}$$

and the potential temperature gradient can be expressed as

$$\frac{d\theta}{dz} = \frac{\theta_*}{kz}\phi_h\left(\frac{z}{L}\right). \tag{3.25}$$

Notice that when the surface heat flux goes to zero, $L \to \infty$ and $z/L \to 0$. This means that $\phi_m(0) = 1$ and $\phi_h(0) = 1$ to be consistent with the gradient in the neutral boundary layer. Note that θ_* goes to zero when the surface heat flux goes to zero.

The forms represented by Eqs. (3.24) and (3.25) are well supported by observations (Businger et al., 1971), which indicate that

$$\phi_m = \left(1 - 15\frac{z}{L}\right)^{-1/4} \text{ for } L < 0, \tag{3.26a}$$

$$= 1 + 4.7\frac{z}{L} \text{ for } L > 0, \tag{3.26b}$$

and

$$\phi_h = 0.74\left(1 - 9\frac{z}{L}\right)^{-1/2} \text{ for } L < 0, \tag{3.27a}$$

$$= 0.74 + 4.7\frac{z}{L} \text{ for } L > 0. \tag{3.27b}$$

With these forms for ϕ_m and ϕ_h, Eqs. (3.24) and (3.25) can be integrated to yield

$$\frac{U}{u_*} = \frac{1}{k}\left(\ln\frac{z}{z_0} - \psi_1\left(\frac{z}{L}\right) + \psi_1\left(\frac{z_0}{L}\right)\right), \text{ for } L < 0, \tag{3.28a}$$

where

$$\psi_1 = 2\ln\left[\frac{(1+x)}{2}\right] + \ln\left[\frac{(1+x^2)}{2}\right] - 2\tan^{-1}x + \frac{\pi}{2} \tag{3.28b}$$

and

$$x = \left(1 - 15\frac{z}{L}\right)^{1/4}. \tag{3.28c}$$

For stable conditions, $(L > 0)$,

$$\frac{U}{u_*} = \frac{1}{k}\left\{\ln\left(\frac{z}{z_0}\right) + 4.7\frac{(z - z_0)}{L}\right\}. \tag{3.29}$$

The expressions for temperature are as follows.

Unstable conditions, $L < 0$

$$\frac{\theta - \theta_o}{\theta_*} = 0.74/k\left[\ln\left(\frac{z}{z_o}\right) - \psi_2\left(\frac{z}{L}\right) + \psi_2\left(\frac{z_0}{L}\right)\right], \tag{3.30}$$

where

$$\psi_2 = \ln\left[\frac{(1+\gamma)}{2}\right], \tag{3.30a}$$

and

$$\gamma = \left(1 - 9\frac{z}{L}\right)^{1/2}. \tag{3.30b}$$

Stable conditions, $L > 0$

$$\frac{\theta - \theta_0}{\theta_*} = 0.74/k\left\{\ln\left(\frac{z}{z_0}\right) + 4.7\frac{(z - z_0)}{L}\right\}. \tag{3.31}$$

In these expressions for the temperature profiles, θ_0 represents the temperature obtained by extrapolating the profile to $z = 0$; this is not the surface temperature. In principle, these profiles can be used to compute surface fluxes of heat and momentum by fitting them to temperature and velocity measurements.

The following sections explain the structures of the upper part of the daytime and nighttime boundary layers.

THE DAYTIME BOUNDARY LAYER

Turbulence in the daytime boundary layer is maintained primarily by sensible heating at the surface, which results in parcels of air that are warmer than their surroundings. These parcels are subject to buoyancy forces that accelerate them upward. The mixing induced by these parcels gives rise to the boundary layer or mixed layer, whose growth is inhibited by the stable temperature gradient of the atmosphere above the mixed layer. Often, the growth of the mixed layer is limited by a sharp subsidence inversion or temperature jump, in which case the height of this inversion determines the maximum mixed layer height.

The turbulent motion in the convective boundary layer is organized into long-lived updrafts and downdrafts that extend through the depth of the boundary layer. These structures are carried by the mean wind as illustrated in Fig. 3.3.

The updrafts consist of accelerating parcels, while the downdrafts are caused by compensating downward motion. Thus, the velocities in updrafts are higher than those in downdrafts; mass balance requires that the horizontal area occupied by downdrafts is higher than that of updrafts. This feature has important effects on dispersion from elevated stacks. Because more material is released into downdrafts than updrafts, the plume centerline descends toward the ground. This gives rise to a vertical concentration distribution that cannot be described with a Gaussian.

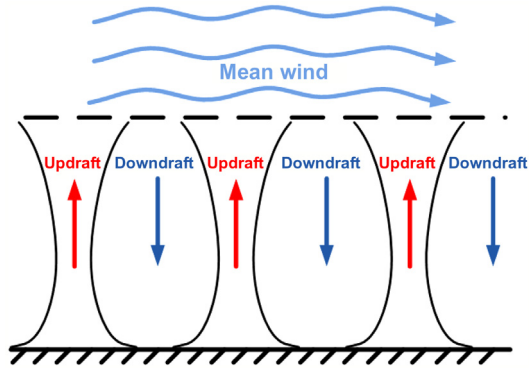

Figure 3.3 Schematic of updrafts and downdrafts caused by surface heating.

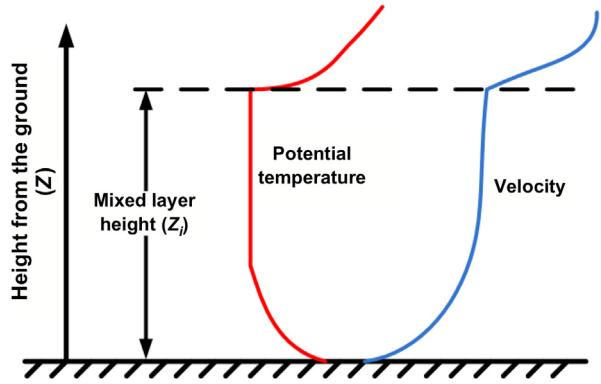

Figure 3.4 Schematic of vertical profile of potential temperature and velocity in the convective boundary layer.

The mean potential temperature and velocity structure in an idealized mixed layer are shown in Fig. 3.4.

The potential temperature is super-adiabatic close to the surface: the potential temperature decreases with height. Above a tenth of the mixed layer height, the potential temperature is relatively uniform because of vigorous vertical mixing. The mixed layer is usually capped by a sharp inversion, especially in areas such as Los Angeles, where semipermanent high-pressure regions create strong subsidence inversions. This inversion limits the height of the mixed layer by resisting the vertical motion of thermals in the mixed layer. The layer above the mixed layer can be stably stratified.

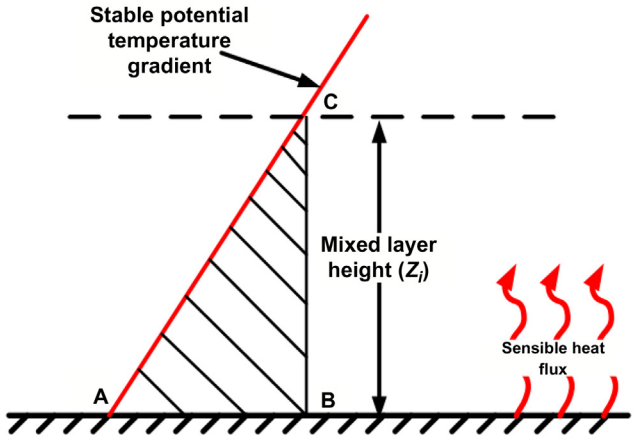

Figure 3.5 Schematic for the calculation of convective boundary layer height.

The velocity profile in the daytime boundary layer is relatively flat in the mixed layer. The rapid change in velocity at the top of the boundary layer reflects the fact that the velocity is vertically mixed below the top.

Height of the Convective Boundary Layer

The height of the mixed layer can be estimated by assuming that the sensible heat input into the atmosphere is used to modify the potential temperature in the mixed layer. Recall from Chapter 2 that the potential temperature, θ, can be used to measure energy changes in the boundary layer; the potential temperature of a parcel changes in response to heat input.

Consider a mixed layer that grows by eroding a layer with a stable potential temperature gradient, as shown in Fig. 3.5.

Assume that the initial temperature profile is represented by AC. Then BC represents the potential temperature after sensible heating has occurred over a time, T, since sunrise. Then, AB is the temperature change at the surface, and the triangle ABC represents the modification of the energy of the atmospheric boundary layer. Denoting the potential temperature gradient of AC by γ, and the temperature change AB by $\Delta\theta$, the energy equivalent of the triangle ABC can be written as

$$\textit{Energy} \text{ in ABC} = \rho C_p \frac{1}{2} \Delta\theta z_i. \tag{3.32}$$

Noticing that $\Delta\theta = \gamma z_i$, we can equate this energy to the sensible heat flux integrated over T to obtain

$$\rho C_p \frac{1}{2}\gamma z_i^2 = \int_0^T H(t)dt, \tag{3.33}$$

where $H(t)$ is the time-varying sensible heat flux. For simplicity, if we assume that the sensible heat flux increases linearly with time, we obtain the following expression for the mixed layer height:

$$z_i^2 = \frac{H_{\max} T}{\gamma \rho C_p}, \tag{3.34}$$

where $H_{\max}$ is the maximum heat flux. If we assume that the maximum occurs at noon, Eq. (3.34) can be used to estimate z_i at noon. Taking $H_{\max}/\rho C_p = 0.3$ m/sK, $T = 6$ hours, and $\gamma = 5$ K/1000 m, we find $z_i \sim 1000m$. Note that the boundary layer height increases with time as long as the heat flux is positive. So the maximum height occurs at sunset. Assuming that this occurs 6 hours after noon, we see from Eq. (3.34) that its value is about $\sqrt{2} \times 1000 = 1414$m.

It was shown earlier that the turbulent velocities generated by buoyancy in the surface layer are proportional to the free convection velocity scale, u_f defined by

$$u_f = \left(\frac{g}{T_s} Q_0 z\right)^{1/3}. \tag{3.35}$$

For heights below $0.1z_i$ we find that buoyancy generates velocities given by

$$\sigma_w = 1.3u_f; \quad z \leq 0.1z_i. \tag{3.36}$$

We saw earlier that at heights less than $|L|$, where turbulence production is dominated by shear, σ_w is roughly proportional to u_*,

$$\sigma_w = 1.3u_*. \tag{3.37}$$

A formulation for σ_w that interpolates between the limits set by $1.3u_*$ and u_f is given by Panofsky et al. (1977) as

$$\sigma_w = 1.3\left(u_*^3 + u_f^3\right)^{1/3}, \tag{3.38}$$

yielding

$$\frac{\sigma_w}{u_*} = 1.3\left[1+2.5\left(\frac{-z}{L}\right)\right]^{1/3}. \tag{3.39}$$

Between $0.1z_i$ and close to the top of the mixed layer, σ_w associated with buoyancy production of turbulence is proportional to the convective velocity scale given by

$$w_* = \left(\frac{g}{T_s} Q_0 z_i\right)^{1/3}, \tag{3.40}$$

where z_i is the mixed layer height. Then, we find that

$$\sigma_w = \sigma_v = \sigma_u \cong 0.6 w_*. \tag{3.41}$$

It is found that σ_u and σ_v are also proportional to w_*, even below $0.1z_i$. The shear contribution to the turbulence levels is usually small relative to the buoyancy contribution at heights above $0.1z_i$.

THE NIGHTTIME BOUNDARY LAYER

When the sun sets, turbulence energy production by buoyancy comes to a stop. Over a period of an hour, the turbulence in the mixed layer collapses, and shear becomes the primary mechanism for the production of turbulence. Because the ground is initially warmer than the atmosphere, the thermal radiation leaving the ground exceeds that being supplied by the atmosphere. This deficit leads to a cooling of the ground.

Initially, both the sensible heat flux and the ground heat flux are directed away from the earth's surface. The surface cools rapidly, and a point is reached at which the ground becomes colder than the layers above in the atmosphere. At this stage, the heat flux from the atmosphere is directed toward the earth's surface. This process is referred to as the formation of a radiation-induced surface inversion—the temperature (and the potential temperature) increases with height.

The mean temperature and velocity above the surface boundary layer increase with height as shown in Fig. 3.6.

There is little agreement on the general form of these profiles in the stable boundary layer. On the basis of measurements made in Holland,

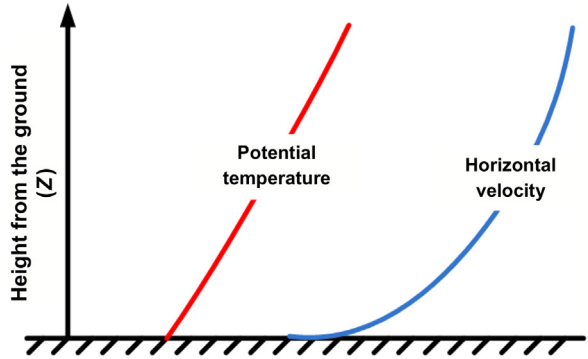

Figure 3.6 Schematic of vertical profile of potential temperature and velocity in the stable boundary layer.

Van Ulden and Holtslag (1985) suggest that the mean wind can be described by

$$u(z) = \frac{u_*}{k}\left[\ln\left(\frac{z}{z_o}\right) - \psi_m\left(\frac{z}{L}\right) + \psi_m\left(\frac{z_o}{L}\right)\right] \tag{3.42}$$

where

$$\psi_m\left(\frac{z}{L}\right) = -17\left[1 - \exp\left(-0.29\frac{z}{L}\right)\right]$$

The horizontal wind usually shows considerable turning with height. Van Ulden and Holtslag (1985) propose the following equation to estimate this turning:

$$\frac{D(z)}{D(z_i)} = d_1\left[1 - \exp\left(-d_2\frac{z}{z_i}\right)\right] \tag{3.43}$$

where

$$d_1 = 1.58;\ d_2 = 1.0$$

and

$$D(z_i) \cong 35^\circ$$

Here z_i is the height of the boundary layer, which is discussed later. We do not have similar equations for the variation of temperature through the depth of the boundary layer. In the absence of information through measurements, we suggest extrapolating the surface boundary layer, Eq. (3.30), through the boundary layer.

Most expressions for the height of the stable boundary layer, which we denote by h, are based on dimensional analysis backed by relatively weak physical arguments. One scheme assumes

$$\frac{dh^2}{dt} \sim wl, \tag{3.44}$$

where l is the length scale and w is the velocity scale of the turbulent eddies leading to the growth of the boundary layer. The combination wl is called the eddy diffusivity of turbulence, K. We will see later how K can be used to derive useful formulas for dispersion of pollutants.

If we assume that the turbulent eddies in the stable boundary layer scale with the Monin–Obukhov length, L, K can be written as

$$K \sim u_* L, \tag{3.45}$$

where u_* is the surface friction velocity. If L exceeds h, the eddies scale with h, and K is written as

$$K \sim u_* h. \tag{3.46}$$

Thus, when h is small relative to L, substituting Eq. (3.46) into Eq. (3.44) yields

$$\frac{dh}{dt} = \alpha u_*, \tag{3.47}$$

where α is a constant that needs to be determined empirically.

When h exceeds L, Eqs. (3.45) and (3.44) give

$$\frac{dh^2}{dt} \sim u_* L. \tag{3.48}$$

We can obtain Zilitinkevich's expression for the stable boundary layer height by integrating Eq. (3.48) assuming that u_* and L are constant:

$$h^2 \sim u_* L t, \tag{3.49}$$

and taking the time of growth, t, to be governed by the Coriolis parameter, f, as follows:

$$t = 1/f. \tag{3.50}$$

Then,

$$h = a\left(\frac{u_* L}{f}\right)^{1/2}, \tag{3.51}$$

where a is an empirically determined constant.

We can readily write an expression that varies continuously between Eqs. (3.47) and (3.48) (for constant u_* and L) as follows:

$$h = u_* t \left[\frac{L/h}{a + bL/h} \right]. \tag{3.52}$$

Eq. (3.52) reduces to Nieuwstadt's (1981) interpretation if we put $t = 1/f$.

The problem with diagnostic equations such as Eq. (3.52) is that the height of the boundary layer reacts instantaneously to u_* and L. This means that h will drop suddenly (and unrealistically) if the wind speed, and thus u_*, decreases quickly. One way of getting around this problem is to allow the boundary layer to have some inertia. This is done by using the following equation to estimate the time evolution of h:

$$\frac{dh}{dt} = \frac{h_d - h}{\tau}, \tag{3.53}$$

where h_d is the estimate given by the diagnostic equation, and τ is the timescale, given by

$$\tau = \frac{\beta h}{u_*}, \tag{3.54}$$

where β is an empirical constant.

When $h_d = h$, h does not change. If h_d increases suddenly in response to an increase in wind speed, dh/dt becomes positive, so that h will grow toward h_d; the time of reaction is proportional to h/u_*. This means that if either h is large, or u_* is small, h reacts slowly to changes in h_d. It is seen that sudden decreases in h_d do not result in similar changes in h unless the reaction timescale, τ, is small enough.

One way of interpreting Eq. (3.54) is to think of h_d as the input to a system, while h is the required output. The response of h to changes in h_d is damped by the timescale, τ. If τ is large, h responds slowly to changes in h_d; a small τ allows h to follow changes in h_d.

Turbulent Velocities in the Stable Boundary Layer

As explained earlier, the stable potential temperature gradient suppresses the production of turbulence because it opposes vertical motion. Under these circumstances, shear production of turbulence is matched by the

destruction associated with the stable temperature gradient and viscous dissipation. This balance between these processes of production and turbulence leads to relatively small levels of turbulence in the nocturnal boundary layer. The low turbulence levels in the stable boundary layer are accompanied by smaller dispersion rates compared to those in the daytime atmospheric boundary layer. Elevated plumes show little vertical spread during the night because of the low levels of turbulence.

The presence of clouds increases the thermal radiation reaching the earth's surface. The surface cools less under these circumstances, and the nocturnal inversion is less pronounced. This implies that turbulence levels in cloudy conditions are higher than those found under cloud-free conditions. This effect of clouds is substantially different from that during the day, when clouds decrease the solar radiation reaching the ground. During daytime when clouds are present, turbulence levels, associated with buoyancy production of turbulence, are reduced compared to those under clear sky conditions.

While we do know that the levels of turbulence in the stable boundary layer are low, we are not in a good position to characterize the variation of these levels as a function of height. The parameterization that is sometimes used to estimate σ_w is that of Nieuwstadt (1984):

$$\sigma_w^2 = 1.7u_*^2\left(1 - \frac{z}{h}\right). \tag{3.55}$$

We point out that the observational evidence to support Eq. (3.55) is meager; measurements indicate that σ_w can actually increase with height. Under these circumstances, it is advisable to use measurements when possible.

The horizontal turbulent velocities, σ_u and σ_v, in the stable boundary layer do not appear to be related to micrometeorological variables. They are affected by mesoscale flows and local topography, which are difficult to characterize using models. In the absence of measurements, a value of σ_v of 1 m/s can be used.

The following sections describe the application of the micrometeorology to estimating dispersion in the surface atmospheric boundary layer.

Dispersion Modeling—Ground-Level Source

The concepts that underlie the formulation of a dispersion model can be illustrated by constructing a simple model to estimate ground-level concentrations associated with a surface release. This type of model is relevant for pollution related to transportation because vehicle emissions occur

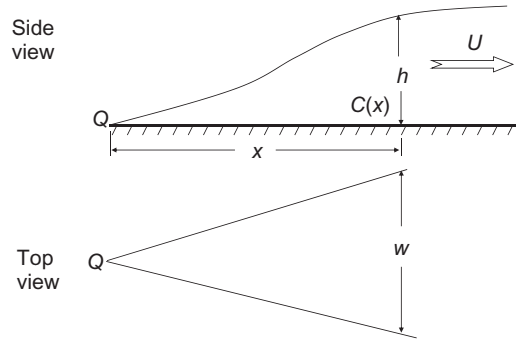

Figure 3.7 Schematic of plume dispersion from a surface release.

close to the ground. Fig. 3.7 shows a plume originating from a point source close to the ground. The plume outline represents a time average so that the irregular boundaries of the observed instantaneous plumes are smoothed out through time exposure. The concentrations associated with an instantaneous plume are difficult to estimate, while a time-averaged plume is more amenable to analysis.

Assume that pollutant release rate (mass/time) is Q. For simplicity, we take the pollutant to be well mixed both in the horizontal and the vertical through the cross-sectional area of the plume. At a distance, x, from the source, the cross-sectional area is the height, h, multiplied by the width, w. Then, the material passing through this area is $C(x)hwU$, where the wind speed, U, is taken to be constant over the height of the plume. If we assume that no material is removed by the ground, the emission rate, Q, has to be equal to the transport of material through the plume cross section at any distance. This yields the following expression for the concentration, $C(x)$,

$$C(x) = \frac{Q}{Uhw}. \tag{3.56}$$

Although this is a highly simplified model of the real world, it contains the essentials of dispersion models used in regulatory applications. In fact, Eq. (3.56) multiplied by a constant was the basis of the dispersion scheme proposed by Pasquill in 1961.

How do we determine the height and width of a plume when, in reality, the concentration is not uniform across the cross section of the plume? Observations indicate that the time-averaged concentration distribution is approximately Gaussian in the horizontal. The distribution in

the vertical is not Gaussian, as we will see later, but most models assume that this distribution holds in the vertical as well. Notice that the actual concentration measurements might deviate significantly from the smooth Gaussian curve.

The models described in this chapter are designed to estimate concentrations averaged over an hour. They cannot be used to estimate instantaneous concentrations, which are relevant to odor. This chapter also provides the background necessary to understand the approach used in the formulation of such models. This includes the essentials of the micrometeorology used to construct the inputs for the model.

THE POINT SOURCE IN THE ATMOSPHERIC BOUNDARY LAYER

Models to estimate the impact of vehicle emissions are based on the framework of the steady-state Gaussian dispersion equation. If the release point is taken to be the origin ($z = 0$), with the x-axis of the coordinate system aligned along the wind direction at the source, the time-averaged (typically 1 hour) concentration field is described in terms of the Gaussian distribution (see Fig. 3.8):

$$C(x, y, z) = \frac{Q}{2\pi\sigma_y\sigma_z U} exp\left[-\frac{z^2}{2\sigma_z^2} - \frac{y^2}{2\sigma_y^2}\right], \tag{3.57}$$

where y is the distance from the plume centerline, shown as a dotted line in Fig. 3.8, and σ_y is the standard deviation of the horizontal Gaussian

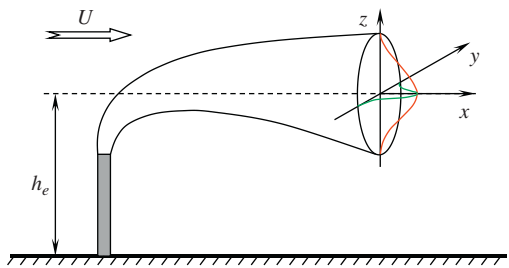

Figure 3.8 Gaussian distribution used to model the plume from a point source. For the time being, we have ignored the effects of the impermeable ground on the concentration field.

distribution. The second exponential in the equation describes the vertical distribution, where z is the height measured from the release point, and σ_z is the standard deviation of the vertical Gaussian distribution. The standard deviations of the distributions, σ_y and σ_z, are referred as the horizontal and vertical spreads of the plume, respectively. Q is the source strength (mass/time), and U is the time-averaged wind speed at source height.

Eq. (3.57) assumes that along-wind dispersion is much smaller than transport by the mean wind. This assumption breaks down when the mean wind is comparable to the turbulent velocity along the mean wind direction, σ_u.

The effect of the ground on concentrations is accounted for by making sure that there is no flux of material through the ground, which we now take to be $z = 0$. The mathematical trick to achieve this is to place an "image" source at a distance $z = -h_e$, where h_e is the effective height of the source above ground. The upward flux from this image source essentially cancels out the downward flux from the real source without affecting the mass balance. Then, the concentration becomes

$$C(x, y, z) = \frac{Q}{2\pi\sigma_y\sigma_z U} exp\left[-\frac{y^2}{2\sigma_y^2}\right]\left\{exp\left[-\frac{(z-h_e)^2}{2\sigma_z^2}\right] + exp\left[-\frac{(z+h_e)^2}{2\sigma_z^2}\right]\right\}. \tag{3.58}$$

In the real atmosphere, dispersion in the upward direction is limited by the height of the atmospheric boundary layer. This limitation of vertical mixing is incorporated into the Gaussian formulation by "reflecting" material off the top of the mixed layer. Then, Eq. (3.58) can be modified to account for the infinite set of "reflections" from the ground and the top of the mixed layer.

The Gaussian formulation for a point source can be used to model both volume and point sources because each of these source types can be discretized into point sources; the associated concentrations are simply the sums of the contributions from these point sources.

DISPERSION IN THE ATMOSPHERIC BOUNDARY LAYER

Until recently plume spread formulations were based on those derived empirically by Pasquill (1961) in the 1960s from observations made during the Prairie Grass dispersion experiment conducted in

Nebraska in 1956 (Barad, 1958). These formulations were modified subsequently by Gifford and Turner, and are commonly referred to as the Pasquill–Gifford–Turner (PGT) curves. For dispersion in urban areas, the Industrial Source Control (ISC) model uses the McElroy–Pooler curves that are derived from experiments conducted in St. Louis, Missouri (McElroy and Pooler, 1968).

The dispersion curves are keyed to stability classes that are related to ranges in the wind speed and incoming solar radiation. The wind speed, measured at 10 m above ground level, is an indicator of turbulence produced by shear, while the incoming solar radiation is a surrogate for the sensible heat flux, which generates turbulence. Thus, the stability classes contain information on shear and buoyancy produced turbulence.

Classes A, B, and C correspond to unstable conditions when buoyancy production of turbulence adds to that due to shear. The sensible heat flux under these conditions is upward. Class A, the most unstable, is associated with the most rapid dispersion rates; the plume spreads for a given distance decreases as we go from class A to C. Class D corresponds to neutral conditions when turbulence production is dominated by shear. Classes E and F are associated with stable conditions. Class F corresponds to the lowest dispersion rates. Thus six dispersion curves, which are only functions of distance from the source, are used to describe the entire range of possible dispersion conditions.

The major advantage of the PGT curves is that they are based on observations and thus provide realistic concentration estimates under a variety of meteorological conditions. Their shortcoming is that they are derived from dispersion of surface releases and are thus not applicable to elevated releases. Furthermore, their formulation does not allow the use of on-site turbulence levels to describe dispersion more accurately than the "broad brush" PGT curves.

In the more recently formulated models such as AMS EPA Regulatory Model (AERMOD) (Cimorelli et al., 2005), plume spreads are described using the solution of the species conservation equation. It turns out that we can learn a great deal about dispersion in the near surface boundary layer using the mass conservation equation expressed in terms of the crosswind-integrated concentration, $\overline{C}^{y}$, which we denote by C here for convenience:

$$U(z)\frac{\partial C}{\partial x} = \frac{\partial}{\partial z}\left(K(z)\frac{\partial C}{\partial z}\right), \tag{3.59}$$

where $K(z)$ is the vertical eddy diffusivity and $U(z)$ is the horizontal velocity. We take the source, with emission rate Q (mass/(time/length)), to be located at ground level at $x = 0$. We assume that there is no flux at the surface and top of the domain and thus the vertical concentration gradients are $\frac{\partial C}{\partial z} = 0$, at $z = 0$ and $z = \infty$, which implies no deposition at the surface. The eddy diffusivity concept, which is based on an analogy with molecular transport, cannot be justified rigorously for turbulent transport. However, it has heuristic value and is useful for developing semiempirical models of turbulent transport.

It can be shown that the eddy diffusivity concept is most applicable when the scale of concentration variation, the plume spread, is larger than the scale of the eddies responsible for plume spreading. In the surface boundary layer, plume spread in the vertical direction is comparable to the length scale of the eddies responsible for vertical transport. It turns out that the eddy diffusivity concept is useful in the surface boundary layer, where Monin−Obukhov similarity provides useful relationships between velocity and temperature gradients and the corresponding heat and momentum fluxes. These relationships can be used to derive eddy diffusivities for heat and momentum, which can be used to describe dispersion by evaluating them at some fraction of the plume height.

Most currently used dispersion models are based on the theoretical foundations laid by a group of workers who showed that understanding of surface micrometeorology, gained in the 1970s, could be used to construct models for dispersion in the surface layer. Several approaches have been in formulating these models. We will follow that proposed by Van Ulden (1978) because it is relatively straightforward.

We can obtain a useful analytical solution of Eq. (3.59) for the following forms of $U(z)$ and $K(z)$:

$$U(z) = U_1 z^m \quad K(z) = K_1 z^n. \tag{3.60}$$

The solution is

$$\frac{C}{Q} = \frac{p}{U_1 \Gamma(s)} \left(\frac{b}{x}\right)^s \exp\left(-\frac{b z^p}{x}\right), \tag{3.61}$$

where

$$b = \frac{U_1}{K_1 p^2} \quad p = m - n + 2$$
$$s = \frac{m+1}{p} \quad , \tag{3.62}$$

and $\Gamma(s)$ is the gamma function defined by $\Gamma(x) = \int_0^\infty t^{x-1}\exp(-t)dt$.

Because the eddy diffusivity equation is a useful model for surface layer dispersion, the solution provides insight into the behavior of crosswind-integrated concentrations under different stabilities. The first thing to notice is that p, the exponent of z, depends on the exponents m and n, which means that the vertical distribution is not Gaussian. That is, p does not equal 2 as elementary dispersion models assume.

In the neutral boundary layer $K = ku_*z$ so that $n = 1$, which means that for any value of m, $s = 1$. This means that the crosswind-integrated concentration falls of as $1/x$, where x is the distance from the source. This means that the concentration from a long line source falls off approximately as distance from the source, as we saw earlier.

When the boundary layer is very stable, $U \sim u_*z/L$ and $K \sim u_*L$ so that $m = 1$ and $n = 0$. This means that $p = 3$, and $s = 2/3$. Notice that for this asymptotic condition, the concentration falls much more rapidly with increasing height than for the value $p = 2$ corresponding to the Gaussian profile. The crosswind-integrated concentration (concentration associated with a line source) falls of as $1/x^{2/3}$.

Under very unstable conditions, the wind speed varies little with height, so that $m = 0$. If we assume that the eddy diffusivity corresponds to that for heat, $K \sim z^{3/2}$, so that $n = 3/2$. Then, $p = 1/2$ and $s = 2$. So the vertical concentration falls of much less rapidly than the Gaussian $p = 2$, and the crosswind-integrated concentration falls of as $1/x^2$.

Van Ulden (1978) shows that we can adapt this solution for any form of the wind speed and eddy diffusivity by recasting the solution, Eq. (3.61), in terms of the mean wind speed, $\overline{U}$, and mean plume height, $\overline{z}$, defined by

$$\overline{U} = \frac{\int_0^\infty U(z)C(z)dz}{\int_0^\infty C(z)dz}$$
$$\overline{z} = \frac{\int_0^\infty zC(z)dz}{\int_0^\infty C(z)dz} \quad . \tag{3.63}$$

Then, Eq. (3.61) can be rewritten as

$$\frac{C}{Q} = \frac{S}{\overline{U}\overline{z}} \exp\left(-\left(\frac{Bz}{\overline{z}}\right)^{p}\right), \tag{3.64}$$

where

$$S = \frac{p\Gamma(2/p)}{\left[\Gamma(1/p)\right]^2} \quad B = \frac{\Gamma(2/p)}{\Gamma(1/p)}. \tag{3.65}$$

This solution becomes useful with the accompanying equation for $\overline{z}$ obtained by differentiating the expression in Eq. (3.63).

$$\frac{d\overline{z}}{dx} = \frac{K(q\overline{z})}{U(q\overline{z})q\overline{z}} \qquad q = (B^p p)^{\frac{1}{1-p}}. \tag{3.66}$$

Van Ulden(1978) shows that for neutral and unstable conditions,

$$\overline{U} = U(0.6\overline{z}) \tag{3.67}$$

is a useful approximation. And for stable conditions,

$$\overline{U} = \frac{u_*}{k}\left[\ln\left(\frac{0.6\overline{z}}{z_0}\right) + 4.7\frac{\overline{z}}{L}\right]. \tag{3.68}$$

By using a constant value for $q = 1.55$ based on $p = 1.5$, Van Ulden (1978) derives implicit expressions for $\overline{z}$ in terms of z_0 and L. More explicit forms of $\overline{z}$ expressed in terms of σ_z are presented in the bulk of the chapter.

Van Ulden (1978) shows that the analytical solution presented in Eqs. (3.64)–(3.68) provides an excellent description of ground-level concentrations measured in Prairie Grass (Barad, 1958). By assuming that the profiles of velocity and eddy diffusivity can be approximated with power laws, Gryning et al. (1983) show that useful estimates of the exponent p of z in the vertical concentration distribution can be obtained from

$$m = \frac{z}{U}\frac{\partial U}{\partial z} \quad n = \frac{z}{K_h}\frac{\partial K_h}{\partial z}, \qquad p = m - n + 2 \tag{3.69}$$

resulting in

$$p = \frac{1+2\beta\zeta}{1+\beta\zeta} + \frac{1+\beta\zeta}{\ln\left(\frac{z_r}{z_0}\right)+\beta\zeta} \quad \zeta > 0$$
$$p = \frac{1-4.5\zeta}{1-9\zeta} + \frac{(1-15\zeta)^{-1/4}}{\ln\left(\frac{z_r}{z_0}\right)-\psi_m(\zeta)} \quad \zeta < 0 \qquad (3.70)$$

where $\zeta = (z_r/L)$, $z_r = 0.8\overline{z}$ for stable conditions and $z_r = 0.4\overline{z}$ for unstable conditions. The function $\psi_m(\zeta)$ corresponds to the Businger–Dyer expression in the velocity distribution

$$\psi_m = 2\ln\left(\frac{1+x}{2}\right) + \ln\left(\frac{1+x^2}{2}\right) - \tan^{-1}x + \frac{\pi}{2}. \qquad (3.71)$$
$$x = (1-15\zeta)^{1/4}$$

We can evaluate the usefulness of these formulas through the numerical solution of Eq. (3.59) using the Businger–Dyer expressions for the wind speed, $U(z)$, and eddy diffusivity, $K_h(z)$. Fig. 3.9 compares the ground-level concentrations obtained from the numerical solution with the Prairie

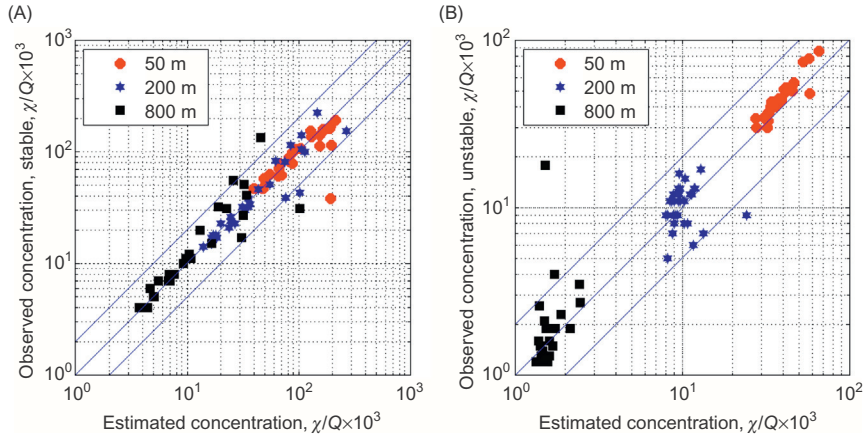

Figure 3.9 Comparison of estimates of crosswind integrated ground-level concentrations from numerical model with corresponding observations from Prairie Grass: (A) stable conditions and (B) unstable conditions. The legend refers to distance from the source. Source: *Data obtained from Van Ulden, A.P., 1978. Simple estimates for vertical dispersion from sources near the ground. Atmos. Environ. 12, 2125–2129.*

Grass data presented by Van Ulden (1978). The deposition velocity of the tracer, SO_2, used in the experiment is taken to be $v_d = 0.07u_*$.

The comparison is good although there is scatter during unstable conditions at 200 and 800 m. Nieuwstadt and Van Ulden (1978) showed that the numerical solution provides an adequate description of the vertical concentration distribution measured at towers located 100 m from the source in the Prairie Grass experiment. They find that the vertical distribution is described well by the solution of:

$$C(x,z) = C(x,0)\exp(-\beta z^p), \tag{3.72}$$

where β and p are obtained through a fitting procedure. It turns out that $p = 2$, corresponding to the Gaussian distribution, is appropriate only under very stable conditions. Under unstable conditions, p is usually less than one. The model, given by Eq. (3.70), provides an adequate description of the magnitude as well as the trend of p as a function of $\overline{z}/|L|$.

The plume spreads, σ_z, formulated in the last section assumed that the vertical distribution is Gaussian. This error is not significant in computing the ground-level concentration because the empirical constants in the formulations reflect the variation of p with stability. However, the error is important in computing the vertical distribution of concentrations. Because the vertical distribution can be approximated with Eq. (3.64), the expression for the crosswind integrated concentration becomes

$$\frac{C(x,z)}{Q} = \sqrt{\frac{2}{\pi}}\frac{1}{\overline{U}\sigma_z}\exp\left(-D\left(\frac{z}{\sigma_z}\right)^p\right) \tag{3.73}$$

where

$$D = \left[\sqrt{\frac{2}{\pi}}\frac{\Gamma(1/p)}{p}\right]^p.$$

Note that σ_z requires an iterative calculation because, the mean velocity, $\overline{U}$, depends on $\overline{z}$, which in turn is related to σ_z through

$$\overline{z} = \sigma_z\left(\sqrt{\frac{\pi}{2}}\frac{p\Gamma(2/p)}{\left[\Gamma(1/p)\right]^2}\right). \tag{3.74}$$

Plume Spread Formulation Used in Current Models

We can formulate expressions for plume spreads of near surface releases by writing Eq. (3.66) as

$$U\frac{d\sigma_z^2}{dx} \sim K(\alpha\sigma_z), \tag{3.75}$$

where α is a constant and because $\overline{z} \sim \sigma_z$ for ground-level releases. We take K, the eddy diffusivity, to correspond to that of heat given by

$$K_H = \frac{u_*\theta_*}{d\theta/dz} = \frac{ku_*z}{\phi_H\left(\frac{z}{L}\right)}, \tag{3.76}$$

where

$$\frac{d\theta}{dz} = \frac{\theta_*}{kz}\phi_H\left(\frac{z}{L}\right), \tag{3.77}$$

where $\phi_H(\frac{z}{L})$ is the Monin–Obukhov similarity function and L is the Monin–Obukhov length.

Let us first consider the near neutral boundary layer in which $\phi_H = 1$, so that $K_H \sim u_*z$. In applying Eq. (3.75) we assume that the eddy diffusivity and the wind speed correspond to a height that is a fraction of σ_z so that

$$\begin{aligned} \sigma_z\frac{d\sigma_z}{dx} &\sim \frac{u_*\sigma_z}{U(\sigma_z)} \\ \frac{d\sigma_z}{dx} &\sim \frac{u_*}{U(\sigma_z)} \end{aligned}. \tag{3.78}$$

Now, the effective wind speed is given by the neutral expression

$$U(\sigma_z) \sim u_*\ln\left(\frac{\sigma_z}{z_0}\right), \tag{3.79}$$

which when substituted in Eq. (3.78) and integrated yields

$$\sigma_z\left[\ln(\sigma_z/z_0) - 1\right] + z_0 \sim x, \tag{3.80}$$

We can replace the logarithmic term in Eq. (3.80) to obtain

$$\sigma_z\left[\frac{U}{u_*} - 1\right] + z_0 \sim x. \tag{3.81}$$

Now u_* is usually a small fraction of U except at small distances from the source. Thus, Eq. (3.81) can be approximated by

$$\sigma_z U \sim u_*x. \tag{3.82}$$

The crosswind-integrated ground level concentration is given by

$$\overline{C}^{y} \sim \frac{Q}{\sigma_z U}. \tag{3.83}$$

The crosswind-integrated concentration is relevant to long line sources of pollution such as roads. Using Eq. (3.80), we obtain the relationship

$$\overline{C}^{y} \sim \frac{Q}{u_* x}. \tag{3.84}$$

This result, which has been derived using other methods by Van Ulden (1978) and Briggs (1982), implies that the concentration of an inert pollutant emitted from a line source, such as a road, falls off linearly with distance from the source. This does not mean that the vertical spread of a plume increases linearly with distance as we see from Eq. (3.85):

$$\sigma_z \sim \frac{u_* x}{U}. \tag{3.85}$$

This equation is implicit in σ_z because the wind speed, U, on the right-hand side of the equation is also a function of σ_z in addition to the roughness length, z_0. Because U increases with σ_z, we expect σ_z to grow less than linearly with distance.

In anticipation of the other expressions derived in this chapter, we rewrite Eq. (3.83) using the following definitions:

$$\overline{C_*}^{y} = \frac{\overline{C}^{y} u_* |L|}{Q}, x_* = x/|L|, \tag{3.86}$$

where L is the Monin–Obukhov length. Then the behavior of the ground-level concentrations under neutral condition is described by

$$\overline{C_*}^{y} \sim x_*^{-1}. \tag{3.87}$$

The Unstable Surface Boundary Layer

To extend our previous analysis to other stabilities we will use the following approach. We will first derive the equations for σ_z assuming the surface layer is very unstable or very stable (small $|L|$). Then, we will interpolate between the neutral and the asymptotically stable or unstable expressions to obtain a formula for the entire range of stabilities. Let us illustrate the application of this approach to derive expressions for

σ_z and the crosswind-integrated concentration for a release in the unstable surface layer.

Under asymptotically unstable conditions, the eddy diffusivity of heat as a function of height is given by

$$K_H(z) \sim u_* z(-z/L)^{1/2}. \tag{3.88}$$

Then Eq. (3.75) for asymptotically unstable conditions becomes

$$U\frac{d\sigma_z^2}{dx} \sim u_*\sigma_z(-\sigma_z/L)^{1/2} \tag{3.89}$$

or

$$\frac{d\sigma_z}{dx} \sim \left(\frac{u_*}{U}\right)\sigma_z{}^{1/2}|L|^{-1/2}. \tag{3.90}$$

Assuming $\left(\frac{u_*}{U}\right)$ approaches a constant value, integrating Eq. (3.90) yields

$$\sigma_z \sim \left(\frac{u_*}{U}\right)^2 x^2|L|^{-1}. \tag{3.91}$$

We can write the expression for the crosswind-integrated concentration as

$$\overline{C}^y \sim \frac{Q}{\sigma_z U} \sim \frac{Q|L|U}{u_*^2 x^2}, \tag{3.92}$$

which in terms of nondimensional variables becomes

$$\overline{C_*}^y \sim \left(\frac{U}{u_*}\right)x_*^{-2}. \tag{3.93}$$

Then, an analytical form that interpolates between the neutral and very unstable limits and fits observations is

$$\sigma_z = 0.57\frac{u_*}{U}x\left(1 + 2\left(\frac{u_*}{U}\frac{x}{|L|}\right)\right) \text{ for unstable conditions.} \tag{3.94}$$

We next derive the equations for vertical spread in the stable surface boundary layer.

The Stable Surface Boundary Layer

Under highly stable conditions, U and K_H can be expressed as

$$K_H \sim u_* L \text{ and } U \sim u_* z/L. \tag{3.95}$$

Substituting this expression in Eq. (3.75) for the rate of growth we obtain

$$u_*(\sigma_z/L)\frac{d\sigma_z^2}{dx} \sim u_* L \tag{3.96}$$

or

$$\frac{d\sigma_z^3}{dx} \sim L^2. \tag{3.97}$$

Integrating Eq. (3.97), we obtain

$$\sigma_z^3 \sim xL^2 \tag{3.98a}$$

or

$$\sigma_z \sim x^{1/3}L^{2/3}. \tag{3.98b}$$

Note that σ_z grows as $x^{1/3}$ under very stable conditions. Using this relationship for σ_z, we can write $U\sigma_z$ as

$$U(\sigma_z) \sim u_*\sigma_z/L \sim u_*(x/L)^{1/3}. \tag{3.99}$$

Then,

$$U\sigma_z \sim u_* x^{2/3}L^{1/3}. \tag{3.100}$$

The expression for the crosswind-integrated ground level concentration becomes

$$\overline{C}^y \sim \frac{Q}{\sigma_z U} \sim \frac{Q}{u_* x^{2/3}L^{1/3}} \tag{3.101}$$

and in terms of nondimensional variables, Eq. (3.101) can written as

$$\overline{C_*}^y = x_*^{-2/3}. \tag{3.102}$$

An expression that interpolates between the neutral and the stable asymptotes for σ_z and also describes observed data is given by

$$\sigma_z = 0.57\frac{u_*}{U}x\frac{1}{\left(1+3\frac{u_*}{U}\left(\frac{x}{L}\right)^{2/3}\right)} \text{ for stable conditions.} \tag{3.103}$$

We mentioned earlier that the equations for plume spread are implicit in σ_z because the wind speed, U, is evaluated at a height proportional to σ_z.

The preceding equations apply primarily to near surface releases because we have assumed that $\overline{z} \sim \sigma_z$. We can extend these equations to finite height releases by evaluating the wind speed, U, at a fraction of the mean plume height, $\overline{z}$, which for a Gaussian vertical distribution of concentrations is related to σ_z through the implicit equation

$$\frac{\overline{z}}{\sigma_z} = \sqrt{\frac{2}{\pi}} exp\left[-\frac{1}{2}\left(\frac{h_e}{\sigma_z}\right)^2\right] + \frac{h_e}{\sigma_z} erf\left(\frac{h_e}{\sqrt{2}\sigma_z}\right), \tag{3.104}$$

where h_e is the effective source height.

We now derive expressions for horizontal spread in the surface boundary layer using some of the techniques used for vertical spread.

Horizontal Spread in the Surface Boundary Layer

The formulation of the horizontal spread equations is based on the results obtained by Eckman (1994) who showed that the variation of σ_y with distance and the initial linear increase followed by a smaller increase with distance (or travel time) could be explained by the increase of the wind speed with height if one assumed that σ_y is governed by the expression

$$\frac{d\sigma_y}{dx} = \frac{\sigma_v}{U}, \tag{3.105}$$

where σ_v is the standard deviation of the horizontal velocity fluctuations, and the transport wind speed, U, is evaluated at a fraction of σ_z.

Under neutral conditions, we can rewrite Eq. (3.105) as

$$\frac{d\sigma_y}{dx} = \frac{\sigma_v}{u_*}\left(\frac{u_*}{U}\right) \sim \frac{\sigma_v}{u_*}\frac{d\sigma_z}{dx} \tag{3.106}$$

resulting in

$$\sigma_y \sim \frac{\sigma_v}{u_*}\sigma_z. \tag{3.107}$$

The asymptotic expression for unstable conditions follows from

$$\frac{d\sigma_y}{dx} = \frac{\sigma_v}{u_*}\left(\frac{u_*}{U}\right). \tag{3.108}$$

As before, assuming that u_*/U is independent of x, we can integrate Eq. (3.108) to obtain

$$\sigma_y \sim \frac{\sigma_v}{u_*}\left(\frac{u_*}{U}x\right). \tag{3.109}$$

The bracketed term in Eq. (3.109) can be rewritten using Eq. (3.91) for σ_z to obtain

$$\sigma_y \sim \frac{\sigma_v}{u_*}(\sigma_z|L|)^{1/2}. \tag{3.110}$$

The formulation of the stable asymptote for σ_y uses

$$\frac{u_*}{U} \sim \frac{L}{\sigma_z} \text{ and } \sigma_z \sim L^{2/3}x^{1/3} \tag{3.111}$$

in Eq. (3.103) to obtain

$$\sigma_y \sim \frac{\sigma_v}{u_*}\frac{\sigma_z^2}{L}. \tag{3.112}$$

We can combine the preceding equations to obtain formulations for σ_y for the entire range of L. Then, the plume spread equations with the empirical constants that provide the best fit between model estimates and observations become, for stable conditions,

$$\sigma_y = 1.6\frac{\sigma_v}{u_*}\sigma_z\left(1 + 2.5\frac{\sigma_z}{L}\right), L > 0. \tag{3.113}$$

The formulation for σ_y for stable conditions that interpolates between neutral and unstable conditions is

$$\sigma_y = 1.6\frac{\sigma_v}{u_*}\sigma_z\left(1 + \frac{\sigma_z}{|L|}\right)^{-1/2}, \; L < 0. \tag{3.114}$$

The preceding equations describe plume spreads measured in field studies in which tracers were released over uniform flat terrain. Thus, the question arises as to whether these equations apply to nonuniform urban conditions. It is likely that the plume spreads in urban areas will deviate from the results of these equations, but in the absence of a theory for nonuniform urban conditions, the best we can do is to use these equations with the meteorological inputs corresponding to the area being considered. However, these equations cannot be applied in the presence of building structures, such as street canyons, that induce three-dimensional flows.

CONCLUDING REMARKS

Air quality models used in practice for source–receptor distances of a few kilometers assume that emissions from a source can be described by a plume in which the concentration distributions in the horizontal and vertical follow the Gaussian distribution; as we have seen, other distributions can be used to describe the vertical concentration profile. This framework allows the incorporation of several processes that affect ground-level concentrations. It can be readily used to interpret data from field studies and thus can be improved empirically to provide better descriptions of dispersion. These features, coupled with its computational simplicity, explain its popularity in applications that require realism as well as transparency.

Highways and roads situated in urban areas are usually lined by sound barriers and can be depressed or elevated relative to the surroundings. These configurations have major effects on dispersion of emissions from the road and hence on near-road air quality. Chapter 4, The Impact of Highways on Urban Air Quality, deals with these effects.

REFERENCES

Barad M.L. (Ed.), 1958. Project Prairie Grass. A field program in diffusion, Geophysical Research Paper No. 59, vols. I (300 pp.) and II (221 pp.), AFCRF-TR-58-235, Air Force Cambridge Research Center, Bedford, MA.

Briggs, G.A., 1982. Similarity forms for ground-source surface-layer diffusion. Bound. Layer Meteorol. 23, 489–502.

Businger, J.A., 1973. In: Haugen, D.A. (Ed.), Turbulent transfer in the atmospheric surface layer, workshop on micrometeorology. American Meteorological Society, pp. 67–100.

Businger, J.A., Wyngaard, J.C., Izumi, Y., Bradley, E.F., 1971. Flux-profile relationships in atmospheric surface layer. J. Atmos. Sci. 28, 181–189.

Cimorelli, J.A., Perry, G.S., Venkatram, A., Weil, C.J., Paine, J.R., Wilson, B.R., et al., 2005. AERMOD: a dispersion model for industrial source applications. Part I: General model formulation and boundary layer characterization. J. Appl. Meteorol. 44, 682–693.

Eckman, R.M., 1994. Re-examination of empirically derived formulas for horizontal diffusion from surface sources. Atmos. Environ. 28, 265–272.

Gryning, S.E., Van Ulden, A.P., Larsen, S., 1983. In: Model, A.K. (Ed.), Dispersion from a ground level source investigated, vol. 109. Quart. J. R. Meteorol. Soc., pp. 355–364.

McElroy, J.L., Pooler, F., 1968. The St. Louis dispersion study-volume II—analysis. National Air Pollution Control Administration, Pub. No. AP-53, US DHEW Arlington, 50 pps.

Nieuwstadt, F.T.M., 1981. The steady state height and resistance laws of the nocturnal boundary layer: theory compared with Cabauw observations. Bound. Layer Meteorol. 20, 3–17.

Nieuwstadt, F.T.M., 1984. The turbulent structure of the stable, nocturnal boundary layer. J. Atmos. Sci. 41, 2202–2216.

Nieuwstadt, F.T.M., Van Ulden, A.P., 1978. A numerical study of the vertical dispersion of passive contaminants from a continuous source in the atmospheric surface layer. Atmos. Environ. 12, 2119–2124.
Panofsky, H.A., Tennekes, H., Lenschow, D.H., Wyngaard, J.C., 1977. The characteristics of turbulent velocity components in the surface layer under convective conditions. Bound. Layer Meteorol. 11, 355–361.
Pasquill, F., 1961. The estimation of the dispersion of windborne material. Meteor. Mag. 90, 33–49.
Stull, R., 1988. An Introduction to Boundary Layer Meteorology. Springer, The Netherlands.
Van Ulden, A.P., 1978. Simple estimates for vertical dispersion from sources near the ground. Atmos. Environ. 12, 2125–2129.
Van Ulden, A.P., Holtslag, A.A.M., 1985. Estimation of atmo- spheric boundary-layer parameters for diffusion applications. J. Clim. Appl. Meteorol. 24, 1196–1207.

FURTHER READING

Calder, L.K., 1973. On estimating air pollution concentrations from an highway in an oblique wind. Atmos. Environ. 7, 863–868.
Csanady, G.T., 1973. Turbulent Diffusion in the Environment. Reidel, Dordrecht, p. 248.
Esplin, J.G., 1995. Approximate explicit solution to the general line source problem. Atmos. Environ. 29, 1459–1463.
Holtslag, A.A.M., Van Ulden, A.P., 1983. A simple scheme for daytime estimates of the surface fluxes from routine weather data. J. Climate Appl. Meteorol. 22, 517–529.
Luhar, K.A., Patil, R.S., 1989. A general finite line source model for vehicular pollution prediction. Atmos. Environ. 23, 555–562.
Perry, S.G., 1992. CTDMPLUS: a dispersion model for sources in complex topography. Part I: Technical formulations. J. Appl. Meteor. 31, 633–645.
Schulman, L.L., Strimaitis, D.G., Scire, J.S., 2000. Development and evaluation of the PRIME Plume Rise and building downwash model. JAPCA J Air Waste Manag. Assoc. 50, 378–390.
Snyder, W.H., Thompson, R.S., Eskridge, R.E., Lawson, R.E., Castro, I.P., Lee, J.T., et al., 1985. The structure of the strongly stratified flow over hills: dividing streamline concept. J. Fluid Mech. 152, 249–288.
Taylor, G.I., 1921. Diffusion by continuous movements. Proc. London Math. Soc., Ser. 2 (20), 196–211.
Venkatram, A., 1980. Estimating the Monin–Obukhov length in the stable boundary layer for dispersion applications. Boundary-Layer Meteorol. 19, 481–485.
Venkatram, A., 1992. Vertical dispersion of ground-level releases in the surface boundary layer. Atmos. Environ. 26, 947–949.
Venkatram, A., 1993. Estimates of the maximum ground level concentration in the convective boundary layer—the error in using the Gaussian distribution. Atmos. Environ. 27A, 2187–2191.
Venkatram, A., Horst, T.W., 2006. Approximating dispersion from a finite line source. Atmos. Environ. 40, 2401–2408.
Venkatram, A., Brode, R., Cimorelli, A., Lee, R., Paine, R., Perry, S., et al., 2001. A complex terrain dispersion model for regulatory applications. Atmos. Environ. 35, 4211–4221.
Weil, J.C., 1985. Updating applied diffusion models. J. Climate Appl. Meteor. 24 (11), 1111–1130.
Weil, J.C., 1988. In: Venkatram, A., Wyngaard, J.C. (Eds.), Plume Rise. Lectures on Air Pollution Modeling. American Meteorological Society, Boston, MA, pp. 119–166.

CHAPTER FOUR

The Impact of Highways on Urban Air Quality

Contents

Introduction 77
Line Source Dispersion Model 78
Modeling a Highway 81
  Comparison of Highway Models with Observations 84
Models for the Impacts of Barriers 84
  Effects of Solid Barriers 84
  Model for Downwind Barrier 87
  Model for Upwind Barrier 90
  Dispersion from Depressed Roadways 92
  Model for Depressed Roads 93
  Effects of Vegetation Barriers 96
  Model for a Solid-Vegetation Barrier 98
Summary 99
References 102
Further Reading 104

INTRODUCTION

As indicated in Chapter 3, the impact of highways on near-road air quality can be estimated through models that treat the highway as a set of line sources covering the width of the highway, and running parallel to the road. In this chapter, we describe how the basic line source model can be adapted to model dispersion from a highway that has a finite width and length. We then show how the model can be modified to account for the effects of (a) barriers or structures adjacent to the road, and (b) elevation or depression of the road surface relative to ground level.

It is important to note that the application of the methods discussed in this chapter is restricted to estimating the concentrations of primary emissions from vehicles at distances of up to a few kilometers from the road. Secondary particle formation, chemical transformation, and dry and wet

Urban Transportation and Air Pollution.
DOI: https://doi.org/10.1016/B978-0-12-811506-0.00004-X

deposition are not addressed in this chapter. The methods discussed here are limited to cases where concentrations are primarily affected by transport and dispersion. This is not a practical limitation because most traffic-emitted pollutants, transported at typical wind speeds, are mixed through the planetary boundary layer before chemistry and removal processes become important. At these travel times, it is more appropriate to apply puff or Eulerian grid models, which can accommodate these processes in a convenient framework.

LINE SOURCE DISPERSION MODEL

The basic components of a model used to compute estimates of concentrations of highway emissions are the line source and plume spread expressions described in chapter 3, which we repeat here for convenience. The line source is a basic building block of highway models. Each lane of the highway is represented by a line source. Fig. 4.1 illustrates the coordinate system used to derive the expression for concentration associated with a line source. The x-axis lies along the direction of the mean wind, U, and the line source is inclined at an angle, θ, with the y-axis. In the

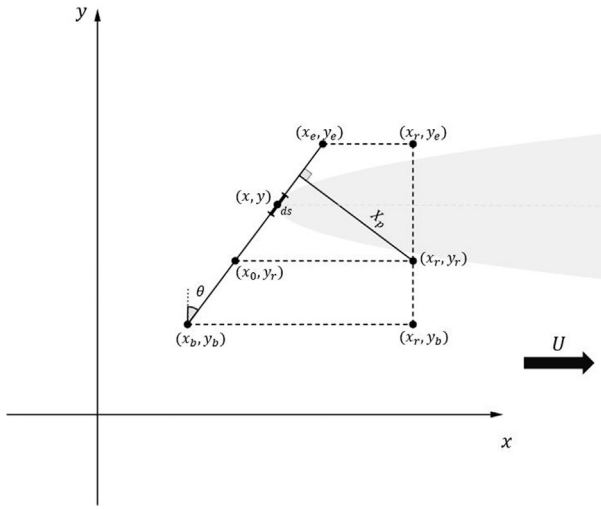

Figure 4.1 Coordinate systems used to calculate contribution of point source at (x,y) to concentration at (x_r,y_r). The system x–y has the x-axis along the mean wind direction, which is at an angle θ to the fixed X axis.

untransformed coordinate system, θ corresponds to the wind direction with respect to the X axis. The (X, Y) point transforms to (x, y) in the mean wind coordinate system according to

$$\begin{aligned} x &= X\cos\theta + Y\sin\theta \\ y &= -X\sin\theta + Y\cos\theta \end{aligned}. \tag{4.1}$$

The beginning and end points of the line source are at (x_b, y_b) and (x_e, y_e) in the rotated coordinate system. The concentration at a receptor is the integral of the contributions of the elemental sources along the line source, each of which has a different downwind distance relative to the receptor. The source strength of an elemental source at (x, y) is qds, where q is the emission rate per unit length of the source, and ds is the length of the element, $ds = dy/\cos\theta$. Then, the concentration at ground level at (x_r, y_r) associated with the line source is:

$$C(x_r, y_r, 0) = \sqrt{\frac{2}{\pi}}\frac{q}{\cos\theta}\int_{yb}^{ye}\frac{1}{U\sigma_y(x_r - x)\sigma_z(x_r - x)}\exp\left(-\frac{(y-y_r)^2}{2\sigma_y^2(x_r - x)}\right)dy \tag{4.2}$$

where the height of source is taken to be zero. Note that both σ_y and σ_z are evaluated at $(x_r - x)$. While this integral can be evaluated numerically, we can obtain a useful analytical approximation by noticing that most of the contribution to the integral originates from the region of the line directly upwind of the receptor. This point on the line is seen to be (See Fig. 4.1):

$$x_0 = x_b + (y_r - y_b)\tan\theta, \tag{4.3}$$

and the downwind distance to the receptor is $x_d = x_r - x_0$. Luhar and Patil (1989) showed that if the vertical spread, σ_z, and horizontal spread, σ_y, are evaluated at this effective distance, the integral could be evaluated to obtain an analytical expression for the concentration associated with a finite line source. The expression is not accurate at wind angles over $\theta = 80°$. Venkatram and Horst (2006) provided a modified expression that is accurate at these large angles and at the same time accounts for the fact that some part of the line source is upwind of the line. The expression for the ground-level concentration from a source near ground level is:

$$C(x_r, y_r) = \sqrt{\frac{2}{\pi}}\frac{q}{U\cos\theta\sigma_z(x_d)}\frac{\left[erf(t_e) - erf(t_b)\right]}{2} \tag{4.4}$$

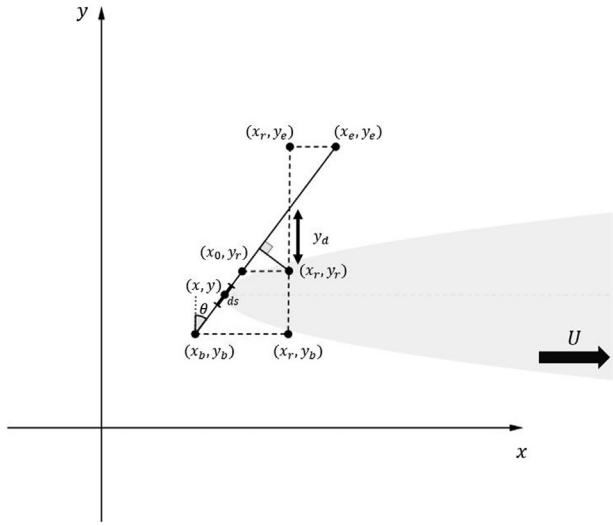

Figure 4.2 Part of the line is upwind of the receptor. The sign of y_d determines the sign of the error function in Eq. (4.4).

where *erf* is the error function. The vertical spread is still evaluated at x_d, but the relevant horizontal spreads are calculated at downwind distances corresponding to the beginning and end points of the line, and are included in the limits

$$t_e = \frac{(y_e - y_r)}{\sqrt{2}\sigma_y(x_r - x_e)}$$
$$t_b = \frac{(y_b - y_r)}{\sqrt{2}\sigma_y(x_r - x_b)} \tag{4.5}$$

Now, if the receptor is close enough to the line source, the downwind distance to the end of the line can be negative, $(x_r - x_e) < 0$, and the part of the line above the point, i, shown in Fig. 4.2 does not contribute to the receptor concentration. At this point, the variable, t, approaches ∞ because $\sigma_y(x_r - x_i) = 0$. Then, $\text{erf}(t_i) = 1$ because $(y_i - y_r) > 0$. We have to allow for the possibility that $(x_r - x_b) < 0$, in which case $\text{erf}(t_i) = -1$ because $(y_i - y_r) < 0$. We can account for both cases by defining $y_d = x_d/\tan\theta$, the vertical distance along x_r to the point on the line at which the downwind distance to the receptor is zero. The sign of y_d determines the sign of the error function. Then, if $(x_r - x_{b,e}) < 0$, $\text{erf}(t_{b,e}) = \text{sign}(y_d)$ in the expression for the concentration.

The expression for an infinite line source is obtained by setting $y_b = -\infty$ and $y_e = \infty$ in Eq. (4.4) to yield (Calder, 1973) formula:

$$C(X_r, Y_r) = \sqrt{\frac{2}{\pi}} \frac{q}{U\cos\theta\sigma_z(x_d)} \tag{4.6}$$

Notice that the wind direction has two effects. The dilution wind speed becomes $U\cos\theta$, which is the component of the wind that is normal to the line source. At the same time, the vertical spread is evaluated at an oblique distance, $x_p/\cos\theta$, where x_p is the perpendicular distance from the receptor to the line. We note Calder's observation that the concentration given by Eq. (4.6) is relatively insensitive to the wind direction because the decrease in the normal wind speed, $U\cos\theta$, is compensated by the increase in the effective σ_z, which increases with $\cos\theta$. In fact, if σ_z grows linearly with downwind distance, the concentration in Eq. (4.6) becomes independent of the wind direction.

Eq. (4.4) can be applied to highways that are elevated relative to the receptor by multiplying the equation by the term $f(z_s, z_r)$ given by

$$f(z_s, z_r) = \frac{1}{2}\left(\exp\left(-\left(\frac{z_s - z_r}{\sqrt{2}\sigma_z(x_d)}\right)^2\right) + \exp\left(-\left(\frac{z_s + z_r}{\sqrt{2}\sigma_z(x_d)}\right)^2\right)\right) \tag{4.7}$$

where the second term on the right accounts for reflection from the ground. The inclusion of $f(z_s, z_r)$ to account for the effects of release and receptor heights is an approximation whose accuracy deteriorates when the source height is more than twice σ_z.

It turns out that Eq. (4.4) is exact when the wind is perpendicular to the line source, $\theta = 0$, for all source and receptor heights. This allows the use of the expression as the kernel of the integral used to compute concentrations associated with an area source. The two-dimensional integral for an area source can be computed by representing the area as a set of line sources perpendicular to the wind.

MODELING A HIGHWAY

The line source dispersion model, described in the previous section, is the major component of practical dispersion models such as RLINE

(Snyder et al., 2013). Each lane of the highway is represented by a line source with an emission rate modeled using the methods described in Chapter 1. Plume spreads are modeled using the equations described in Chapter 3. One of the basic modifications to highway dispersion models is the inclusion of vertical plume spread induced by vehicle motion on the road. Models based on the solution of the numerical solution of the governing momentum and mass conservation equations (Kalthoff et al., 2005; Steffens et al., 2014) include explicit treatment of turbulence produced by moving vehicles. In analytical models such as RLINE, this effect is included through an initial vertical plume spread, which is approximately taken to be the height of the vehicles because vehicle wakes tend to mix pollutant emissions over this height. Then,

$$\sigma_{zhwy}^2 = h_0^2 + \sigma_z^2 \tag{4.8}$$

where σ_z is the vertical plume expression spread derived in Chapter 3, h_0 is the initial plume size, and σ_{zhwy} is the modified plume spread used for the highway models. The initial source size becomes important when the models are used to estimate concentrations very close to the road, where the standard plume spread equations may be unrealistically small and thus result in unrealistically large concentrations.

The approximation of Eq. (4.4) breaks down at $\theta = 90°$ because of the term $\cos\theta$ in the denominator. We can avoid the problem by taking the limit of $\sigma_z\left(\frac{X_r}{\cos\theta}\right)\cos\theta$ as θ approaches 90° to be $\sigma_z(X_r)$. This limit is consistent with the exact solution of the integral for a parallel wind when the vertical and horizontal plume spreads are linear with downwind distance. We account for this limit by modifying the denominator in the equation to $(\sigma_z(X_r) + \sigma_z\left(X_r/\cos\theta\right)\cos\theta)/2$. Comparison with the numerical solution indicates that this approach has an error of less than 25% when θ approaches 90°.

Under low wind speeds, horizontal meandering of the wind spreads the plume over large azimuth angles, which leads to concentrations at receptors upwind relative to the vector averaged wind direction. AERMOD (Cimorelli et al., 2005), and other currently used regulatory models (e.g., ADMS (atmospheric dispersion modeling system), Carruthers et al., 1994), attempt to treat this situation by assuming that when the mean wind speed is close to zero, the horizontal plume spread covers 360°. If the release spreads radially in all horizontal directions, the

ground-level concentration from a ground-level point source with an emission rate, Q, is given by:

$$C(x, y) = \sqrt{\frac{2}{\pi}} \frac{Q}{2\pi r U_e \sigma_z(r)}, \tag{4.9}$$

where r the distance between the source and receptor. The plume is transported at an effective velocity given by

$$U_e = \left(\sigma_u^2 + \sigma_v^2 + U^2\right)^{1/2} = \left(2\sigma_v^2 + U^2\right)^{1/2}, \tag{4.10}$$

where U is the mean vector velocity, and σ_v and σ_u are the standard deviations of the crosswind and along-wind velocity fluctuations. The expression assumes that $\sigma_v \approx \sigma_u$.

If we assume that the vertical plume spread is linear with distance, the integral of the contributions of the meandering components of the point sources along the line source can be written as

$$C_m(x_r, y_r) = \sqrt{\frac{2}{\pi}} \frac{q}{U_e \sigma_z\left(x_p\right)} \frac{\theta_s}{2\pi}. \tag{4.11}$$

where θ_s is the angle subtended by the line source at the receptor: the angle between the lines joining (x_b, y_b), (x_r, y_r), and (x_e, y_e), and x_p is the perpendicular distance of the receptor from the line source. Eq. (4.10) is a useful approximation even when the vertical plume spread is not linear with distance.

The concentration at a receptor is taken to be a weighted average of concentrations of two possible states: a random spread state, Eq. (4.11), and the plume state, Eq. (4.4).

$$C = C_p(1 - f_r) + C_m f_r. \tag{4.12}$$

Where C_p is the concentration from Eq. (4.4). The weight for the random component in Eq. (4.12) is taken to be

$$f_r = \frac{2\sigma_v^2}{U_e^2} \tag{4.13}$$

This ensures that the weight for the random component goes to unity when the mean wind approaches zero. ADMS uses a weighting scheme based on the mean wind speed.

The need to specify the wind speed, U, used in the dispersion model poses a problem in applying the Gaussian dispersion equation to releases

in the surface layer, where the wind speed varies with height. We compute the wind speed, U, at the mean plume height, $\overline{z}$, by solving the following iteratively,

$$\sigma_z = f(x, u_*, L, U(\overline{z})), \tag{4.14}$$

where the mean plume height for a Gaussian concentration distribution is given by

$$\overline{z} = \sigma_z \sqrt{\frac{2}{\pi}} \exp\left[-\frac{1}{2}\left(\frac{z_s}{\sigma_z}\right)^2 \right] + z_s \operatorname{erf}\left(\frac{z_s}{\sqrt{2}\sigma_z}\right) \tag{4.15}$$

where the right-hand side of Eq. (4.15) corresponds to the expressions for vertical spread given by Eqs. (3.94) and (3.103).

Comparison of Highway Models with Observations

Results from the highway model compare very well with measurements of dispersion of roadway emissions in a 1:150 scale wind tunnel model of a 6-lane divided highway (Heist et al., 2009). The model also provides a good description of observations from the Idaho Falls tracer study (Finn et al., 2010) conducted near NOAA's Grid 3 diffusion grid at the Department of Energy's Idaho National Laboratory (INL), which is located across a broad, relatively flat plain on the western edge of the Snake River Plain in southeast Idaho. For the Idaho Falls tracer study, a 54 m-long sulfur hexafluoride tracer line source release positioned 1 m above ground level (AGL) represented a simulated road.

Fig. 4.3 compares the modeled and observed concentration variation with distance from the source for four experiments conducted on 4 days during the Idaho Falls tracer study. There is a tendency for the model to underestimate concentrations at large distances from the source for measurements made during Day 1. However, the underestimation is very small and the observations remain within a factor of two of the model estimates. Overall, there is very little bias in the model and very good correlation.

MODELS FOR THE IMPACTS OF BARRIERS

Effects of Solid Barriers

Solid barriers affect concentrations associated with vehicle emissions by modifying the flow field and turbulence in the vicinity of the barrier.

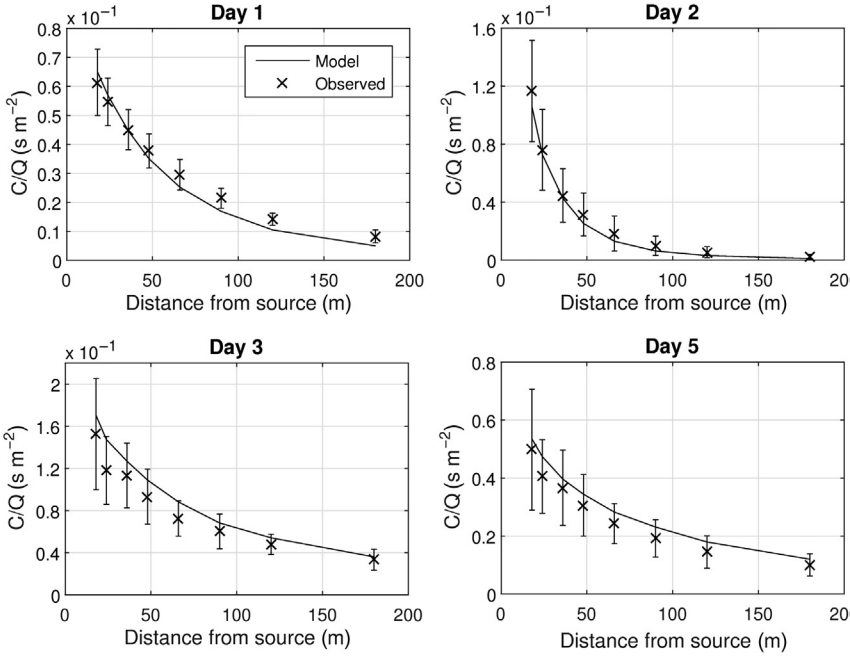

Figure 4.3 Downwind variation of highway dispersion model and crosswind maximum of 15 min average concentration observations during the control experiments (no barrier present) of the Idaho Falls study. Error bars show standard deviation of observations. The 4 days of the Idaho Falls study represent measurements during atmospheric stability conditions that are: neutral—Day 1, unstable—Day 2, stable—Day 3, and very stable —Day 5.

The mean flow pattern around a typical solid barrier is shown in Fig. 4.4. When the wind direction is perpendicular to the barrier, the pollutant plumes from vehicles are carried over the barrier by the mean flow that is deflected upward. A recirculating region forms behind the barrier, in which the near surface flow is opposite to that in the mean flow aloft. Above the recirculating cavity, the flow is deflected downward. Turbulence levels are enhanced in a vertically expanding wake whose effects extend to a distance of about 10–20 times the height of the barrier. Fig. 4.5 shows the increase in turbulent kinetic energy (TKE) in the presence of a barrier relative to that with no barrier present at different distances from the barrier. Initially the increase in TKE is largest near the top of the barrier, where the wind-shear generated turbulence is large. Farther downwind the increased TKE becomes mixed over a larger

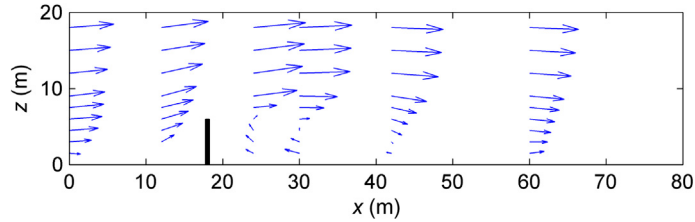

Figure 4.4 Flow induced by a solid barrier. The mean wind direction upwind of the barrier is along the *x*-axis. Arrows represent wind direction vectors. The black rectangle represents the barrier location. Data from EPA wind tunnel study (Heist et al., 2009).

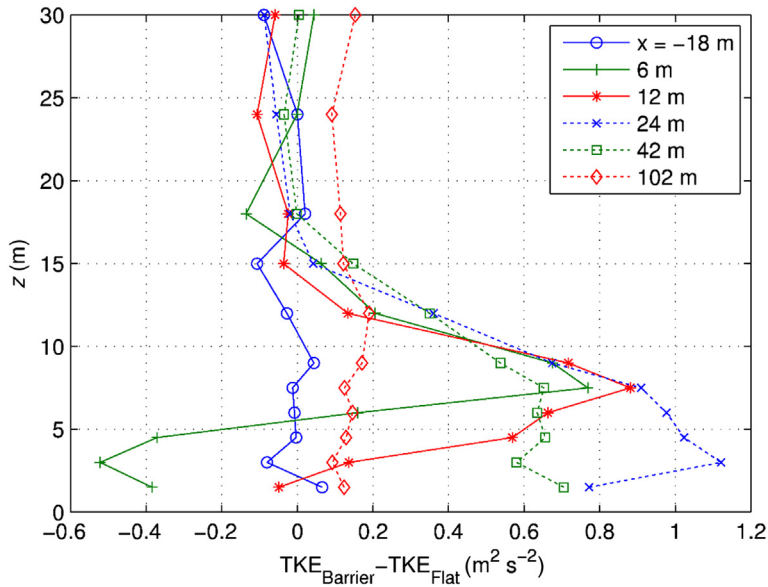

Figure 4.5 Increase in TKE in the presence of a solid barrier at different distances from the 6 m-tall (full scale) barrier. The increased TKE is the difference between the TKE measured in the presence of a barrier and the TKE with no barrier present. Data from EPA wind tunnel study (Heist et al., 2009).

height as the wake grows in size. At 102 m from the barrier, we see that the increased TKE is mixed over a height larger than the barrier.

The upward flow deflection caused by solid barriers effectively raises the height of roadway emissions from near ground level to approximately the height of the barrier. A fraction of these elevated emissions is entrained into the recirculating cavity and then re-emitted into the wake region of

the flow. In general, the combination of all these barrier-induced effects leads to a reduction in concentrations relative to those without the barrier.

The primary effects of barriers described above tend to reduce concentrations downwind. Field (Finn et al., 2010) and wind tunnel (Heist et al., 2009) studies showed that for 6 and 9 m-tall barriers, the concentration immediately downwind of the barrier was 15-50% lower than the concentration with no barrier present. The effect of the barrier on concentrations persisted up to about 50 times the barrier height, after which the concentration approached the value that would occur without the barrier.

A few studies have been conducted to examine the impact of the variation in the shape of the barrier top, porous barriers, catalytic coatings (to reduce NO_2), barriers covered with vegetation (Hooghwerff et al., 2010), and barriers with built-in particulate filters ("EU-LIFE project SPAS," 2011; Iser and Scharl, 2009; Rodler and Henn, 2009). Variations in the shape of the barrier top, porous barriers, catalytic coatings, and barriers covered with vegetation did not reduce the concentration more than a simple 4 m-tall wall. Catalytic coatings and vegetation cover are ineffective because the contact time between pollutants and the barrier surface is not significant. The shape of the barrier top does not alter the primary effects of barriers described above and thus does not significantly influence the concentrations. Filters installed in noise barriers can sometimes reduce concentrations of PM_{10}. However, they are impractical because the pressure due to wind is typically not sufficient to overcome the filter resistance.

Porous barriers cause the same physical effects as solid barriers except that some of the mean flow passes through the barrier rather than over the top. Rows of trees or other vegetation act as porous barriers. The impact of vegetation and other porous barriers on concentrations of traffic emissions is an active area of research and we discuss preliminary research findings at the end of the chapter.

Model for Downwind Barrier

A simple model (Schulte et al., 2014) to account for the impact of the barrier assumes that the concentration is well mixed from the surface to the barrier height, and the concentration profile then follows a Gaussian distribution above the barrier height with the maximum concentration occurring at the barrier height, as shown in Fig. 4.6. We can then

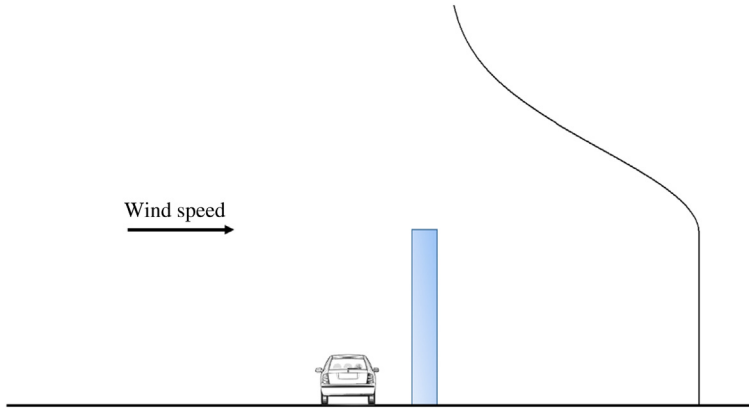

Figure 4.6 Schematic of concentration profile in mixed-wake model.

express the surface concentration associated with an infinitely long line source as:

$$C_s = \frac{q}{U\left(\frac{H}{2}\right)\cos(\theta)H + U(\overline{z})\cos(\theta)\sqrt{\frac{\pi}{2}}\sigma_z} \tag{4.16}$$

where q is the emission rate per length of the line source, C_s is the concentration at the surface, H is the barrier height, $U(\overline{z})$ is the wind speed at the effective centerline height of the plume above the barrier, and θ is the wind direction with respect to the perpendicular to the road. The vertical plume spread, σ_z, is calculated using equations presented in chapter 3.

This model provides a good description of results from the EPA wind tunnel and Idaho Falls tracer studies (Finn et al., 2010; Heist et al., 2009; Schulte et al., 2014). However, it overestimates concentrations close to the barrier during unstable conditions in the Idaho Falls tracer experiment (Finn et al., 2010). To reduce this effect, the model has been modified so that the maximum concentration occurs above the barrier height to be consistent with the wind tunnel data (Heist et al., 2009). The second modification is an entrainment factor, f_m, that reduces entrainment into the barrier wake during unstable conditions. This is an empirical modification to account for the overestimation of concentrations close to the source under the unstable conditions of the Idaho Falls experiment. The factor reduces entrainment behind the barrier as the absolute value of the Monin–Obukhov length decreases. It is also a function of

downwind distance, starting at values below unity just downwind of the barrier and approaching unity at large downwind distances. f_m is taken to be:

$$f_m = f_c + (1 - f_c)\left(1 - \exp\left(-\frac{x}{L_s}\right)\right) \tag{4.17}$$

where f_c, the entrainment factor at $x = 0$, is taken to be:

$$f_c = \exp\left(-\frac{L_s}{|L_{MO}|}\right) \tag{4.18}$$

where $L_s = 10H$ and H is the barrier height. f_c decreases as the absolute value of Monin–Obukhov length decreases.

The third modification is the effect of barrier on surface friction velocity. The surface friction velocity is enhanced based on an empirical model for the development of a neutral boundary layer after a roughness change:

$$u_{*w} = u_*\left(\frac{z_{0w}}{z_0}\right)^{0.17} \tag{4.19}$$

where the effective roughness of the wall is taken to be $z_{0w} = H/9$.

Assuming that the barrier does not modify the upwind heat flux, the Monin–Obukhov length is taken to be proportional to u_*^3. Then, the Monin–Obukhov length behind the barrier is:

$$L_w = L_{MO}\left(\frac{u_{*w}}{u_*}\right)^3 \tag{4.20}$$

The velocity below the barrier height is assumed to be uniform with height given by its value at $z = H$. With these parameterizations, the surface concentration can be expressed as

$$C_s = f_m C_{max}\left[\exp\left(-p_1^2\right) + \exp\left(-p_2^2\right)\right] \tag{4.21}$$

where $C_{\max}$ is the maximum concentration:

$$C_{max} = \frac{\frac{q}{\cos\theta}}{f_m U(H) H\left[\exp\left(-p_1^2\right) + \exp\left(-p_2^2\right)\right] + U(\bar{z})\sqrt{\frac{\pi}{2}}\sigma_z\left[2 - \mathrm{erf}(p_1) - \mathrm{erf}(p_2)\right]} \tag{4.22}$$

In this equation, $U(H)$ is the velocity at barrier height, $p_1 = (H - H_p)/\sqrt{2}\sigma_z$, $p_2 = (H + H_p)/\sqrt{2}\sigma_z$, and H_p is the height of maximum concentration, taken to be:

$$H_p = H + \frac{\sigma_{zB}}{2} \tag{4.23}$$

where σ_{zB} is the vertical plume spread right behind the barrier. This model performs better than the model presented in Schulte et al. (2014) in describing concentrations close to the barrier in the Idaho Falls experiment (Finn et al., 2010) during unstable conditions.

Model for Upwind Barrier

Here, we describe a semiempirical model to estimate the effects of upwind barriers on near-road pollutant concentrations. This allows us to estimate the impact of barriers on both sides of the highway by combining the upwind barrier model with the mixed-wake model (Schulte et al., 2014) to estimate the effect of a downwind barrier. The models have been evaluated using the data collected by Heist et al. (2009) in a wind tunnel study (Ahangar et al., 2017).

Figs. 4.7 and 4.8 depict the velocity profiles seen in the wind tunnel studies when upwind barriers are present. We see that the length of the recirculation zone behind the barrier is about 6 barrier heights. Case "G" and case "H" correspond to a single barrier upwind and downwind of the road, respectively. As expected, the velocity field around a single barrier does not depend on its location.

However, as Fig. 4.8 shows, the recirculation zone extends 4 barrier heights downwind of the upwind barrier when there are barriers on both sides of the highway. This observation is used in formulating the model for dispersion in the presence of two barriers. This is consistent with studies (Becker et al., 2002; Schulman et al., 2000) that show that the extent of the recirculation zone depends on the height of the barrier, the width of the road, the aspect ratio, and the type of boundary layer.

We see from the wind tunnel measurements that the flow in the recirculation zone is directed toward the upwind barrier close to the highway surface. This flow transports the pollutants emitted within the recirculation zone toward the barrier in the upwind direction. This feature is also observed in street canyons on the leeward side of the street and is incorporated in the operational street pollution model (Berkowicz, 2000).

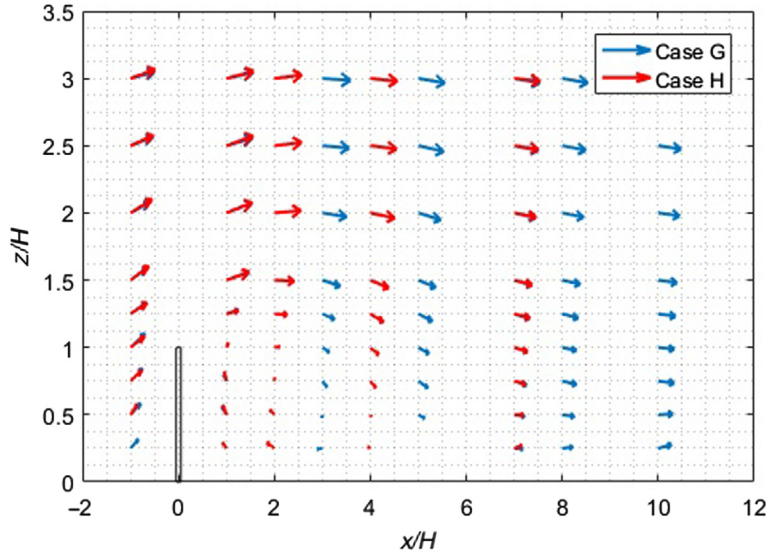

Figure 4.7 Wind velocity vectors in the presence of a solid barrier for case G and case H from the wind tunnel data (Heist et al., 2009). Dimensions are shown as multiples of the barrier height (H) and the location of the barrier has been set to $\frac{x}{H} = 0$ for both cases.

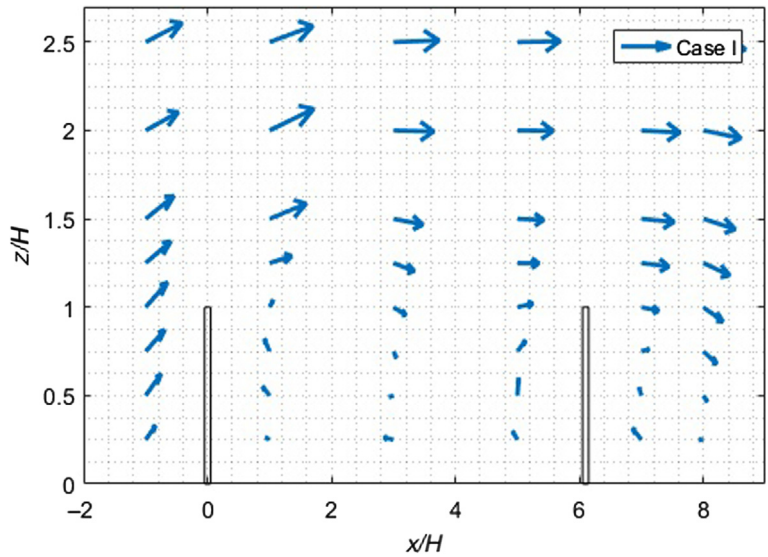

Figure 4.8 Wind velocity vectors in the presence of two solid barriers for case I from the wind tunnel data (Heist et al., 2009). Dimensions are multiples of barrier height (H).

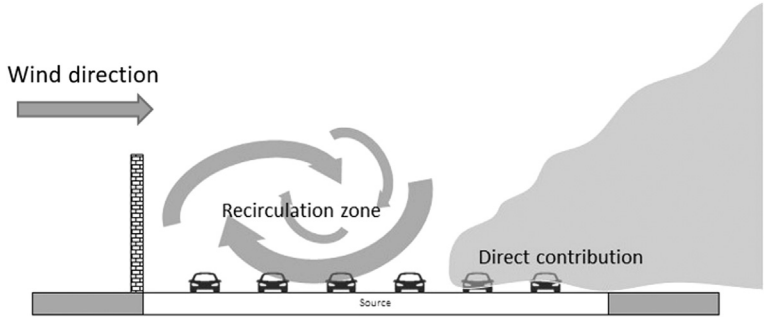

Figure 4.9 Recirculation zone and direct contribution in the upwind barrier model.

We assume that the emissions on the highway that are covered by the recirculation zone originate from a line source located on the upwind barrier at half the height of the barrier. The sources outside the recirculation zone contribute directly to the downwind receptors (see Fig. 4.9).

We model the concentration associated with the line source that represents the emissions in the recirculation zone using the infinitely long line source approximations of Eqs. 4.6 and 4.7:

$$C(x,z)=\frac{q}{U(\bar{z})\cos(\theta)\sqrt{2\pi}\sigma_z\left(x/\cos(\theta)\right)}\left[\exp\left(-\frac{(z_s-z)^2}{2\sigma_z(x)^2}\right)+\exp\left(-\frac{(z_s+z)^2}{2\sigma_z(x)^2}\right)\right] \tag{4.24}$$

where q is the emission rate per unit of length and θ is the angle of the wind direction perpendicular to the line source. In this equation, x is the downwind distance from the line source, z is the receptor height, z_s is the source height, σ_z is the vertical plume spread, and $U(\bar{z})$ is the wind speed evaluated at the effective plume centerline height, $\bar{z}$. The plume spread and wind speed are calculated using the methods described in Chapter 3.

The height of this line source is taken to be half of the barrier height. The sources outside the recirculation are treated as line sources at ground level at various distances from the receptor (Fig. 4.9). The effect of the downwind barrier on these sources is described in the previous section. The combination of the upwind and downwind barrier models provides an excellent description of the concentrations observed in the wind tunnel.

Dispersion from Depressed Roadways

A small number of studies have examined dispersion of emissions from depressed roadways. Feeney et al. (1975) measured particulate lead

concentrations in the vicinity of several road configurations, including a depressed roadway. Samplers were placed 20 m upwind of a freeway and at several distances downwind of the freeway ranging from next to the road to approximately 160 m from the median strip. They found that the mass concentrations of traffic-derived aerosols were lower downwind of the depressed roadway relative to that predicted by a dispersion model that assumed the emissions occurred at road level.

The EPA wind tunnel study (Heist et al., 2009) studied 5 roadway configurations relevant to depressed roads, including flat terrain, a 6 m and a 9 m-deep depressed roadway with vertical sidewalls, a 6 m-deep depressed roadway with 30° sloping sidewalls, and a 6 m-deep depressed roadway with 30° sloping sidewalls with the presence of two 6 m solid barriers on top of the road. They observed that these configurations alter the flow field and increase dispersion and reduce downwind concentrations relative to flat terrain, the reduction in concentrations depending on the particular configuration. For example, surface concentrations measured at a downwind distance of $x = 30$m (from the center of the roadway) were reduced relative to a flat roadway by 66% for the 6 m-deep depressed roadway with vertical walls, and 82% for the 6 m-deep depressed roadway with 30° sloping sidewalls and two 6 m solid barriers on both sides of the road.

The impact of road configurations on the flow field is shown in Fig. 4.10. We see that the depressions modify the flow field relative to that of the flat case. Roadways with vertical sidewalls (Fig. 4.10b and Fig. 4.10d) create recirculating flow in the depressed regions, with a stronger recirculation in the deeper road cut case (Fig. 4.10d). The case with angled side walls has the least effect on the flow field (Fig. 4.10c), showing little evidence of recirculation in the depressed region.

Model for Depressed Roads

It turns out that the effects of the complex flow patterns, seen in Fig. 4.10, induced by the depressed road on dispersion can be simulated through simple modifications to a flat terrain model for near-road dispersion. The modification is to include an initial vertical plume spread and an empirical factor that increases the rate of growth of the plume. For neutral conditions, we use the following equations to compute the vertical plume spread

$$\sigma_z = \sqrt{h_0^2 + \sigma_{zF}^2}; \sigma_{z_F} = 0.57\alpha \frac{u_*}{U(\overline{z})} x \tag{4.25}$$

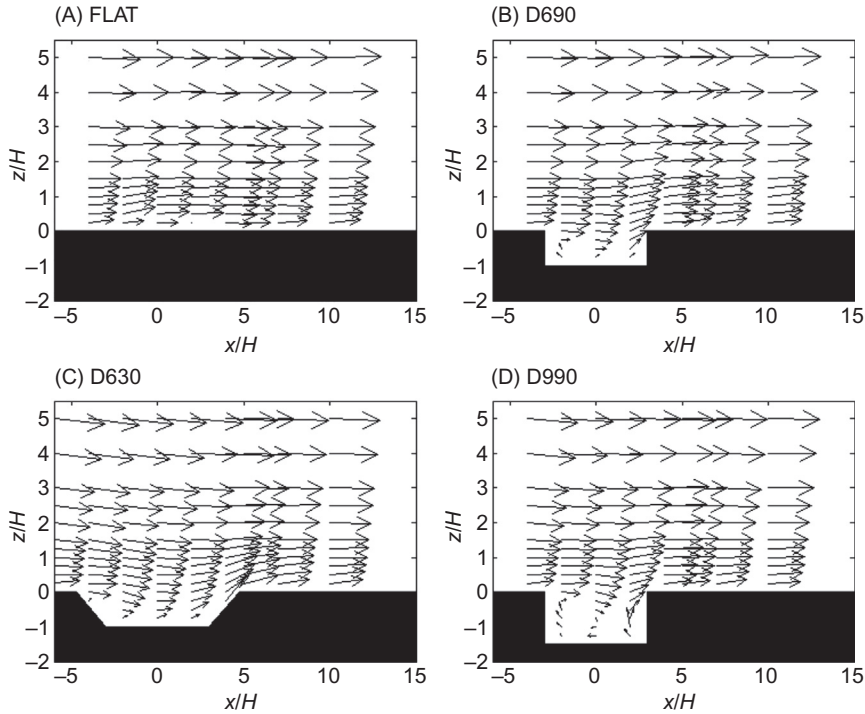

Figure 4.10 Observed mean velocity vectors for various depressed road configurations studied in the wind tunnel (Heist et al., 2009).

The factor α accounts for the increased turbulence in the presence of the road depression. The product αu_* can be interpreted as an effective surface friction velocity. The initial vertical plume spread and α are chosen for each case to obtain the best fit between model estimates and the wind tunnel observations (Heist et al., 2009). The values of h_0 and α for each case are listed in Table 4.1, and the performance of the model in predicting concentrations below a height of 6 m using these values is shown in Fig. 4.11. While these modifications yield good fits to near-surface concentration, the model underestimates concentrations at larger distance from the ground. This is because the concentration profile does not follow the Gaussian profile under neutral conditions, as indicated in Chapter 3.

We see that the effective friction velocity and initial mixing height used to account for the effects of the depressed roadway increase with the depth of the depression. At this point, we do not have enough data to suggest a general formula to estimate the value of the parameters. However, the empirical results from our study are relevant to modeling

Table 4.1 Values of Empirical Parameters of Different Cases that form the σ_z Expression in the Depressed Road Models

Case (see Fig. 4.10)	$h_0(m)$	α
FLAT	0.4	1.00
D690	4.0	1.67
D630	3.5	1.87
D990	4.8	1.83

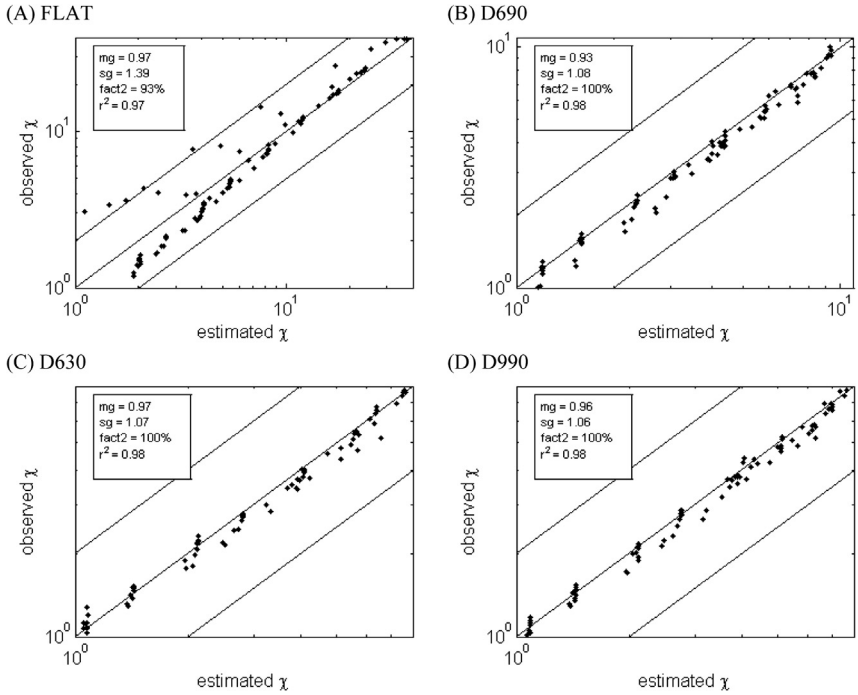

Figure 4.11 Performance of modified RLINE model (Snyder et al., 2013) in estimating concentrations below 6 m height in the flat and depressed road cases of the wind tunnel study (Heist et al., 2009) for all downwind distances. RLINE has been modified to include the initial vertical plume spread and empirical factor α shown in Table 4.1. The concentration, C, has been normalized so that $\chi = CU_r/(Q/L_xL_y)$ where the reference wind speed $U_r = 2.46\ m\ s^{-1}$, the release flow rate $Q = 1500\ cm^3\ min^{-1}$, and the length and width (full scale) of the simulated roadway are $L_y = 72\ m$ and $L_x = 36\ m$, respectively.

the effects of depressed roadways that lie in the range of 6–9 m. The concentrations associated with emissions from these roadways can be estimated by increasing the friction velocity corresponding to flat terrain by a factor of 1.8 and using an initial mixing height of about 4 m. In addition, these magnitudes might be functions of atmospheric stability.

These modifications to a flat terrain model are supported by a study (Venkatram et al., 2013a) that modeled concentrations measured next to a depressed highway in Las Vegas (Baldauf et al., 2013). The basic model assumed line sources (Venkatram and Horst, 2006) located on flat terrain with one modification: vertical mixing of the plume induced by the depression was accounted for through an initial mixing height of the plume equal to the depression of the road, which was approximately 5 m at the location of the measurements.

Effects of Vegetation Barriers

Vegetation barriers have been suggested as a potential method to decrease air pollution near roadways. However, the effects of these barriers on downwind air quality are uncertain. Vegetation barriers affect air quality in two main ways: (1) they absorb particles through dry deposition (Petroff et al., 2008) and (2) they alter the flow fields by forcing the flow over the barrier and decreasing downwind turbulence and wind speed (McNaughton, 1988; Steffens et al., 2012; Tong et al., 2015; Vos et al., 2013; Wang and Takle, 1995). For most vegetation barriers, dry deposition effects are small compared to those related to modifications of the flow field.

Despite the numerous real-world measurements that have been devoted to examine the effect of vegetation barriers on air quality near roadways, conclusions on their effects are not definitive. Al-Dabbous and Kumar (2014) measured concentrations of particles within the size range of 5–560 nm in the vicinity of a roadway in Guildford, Surrey, UK. They observed that the concentration downwind of the 2.2 m-thick vegetation barrier was 37% smaller than the concentration measured directly adjacent to the roadway at a clearing section. Because the receptor downwind of vegetation was 2.2 m further from the roadway than the receptor at the clear section, the actual reduction due to the presence of a vegetation barrier is probably less than the reported value. A field study in Finland deployed passive diffusion-based NO_2 and total anthropogenic VOC samplers, particle deposition samplers, TSI DustTrak DRX samplers for $PM_{2.5}$ and PM_{10}, and TSI P-Trak 8525 condensation particle counters for UFP under tree-canopies in tree-covered park areas and in adjacent treeless areas in the vicinity of 20 sites in Helsinki and Lahti (Setälä et al., 2013). Passive samplers showed insignificant decreases of NO_2, 19% reduction of VOC, and

35%–40% reduction of the mass deposited. However, active samplers showed 20% reduction of ultrafine particles (20–1000 nm), and no difference for $PM_{2.5}$ and PM_{10}. Field studies conducted on evergreen and deciduous trees in North Carolina, USA (Hagler et al., 2012) also concluded that vegetation can lead to higher, lower, or the same concentration as the clearing section. Another field study conducted in Detroit, Michigan (Brantley et al., 2014) showed that the presence of a 15 m-thick vegetation barrier results in 12% reduction in black carbon concentration, while it does not change the particle counts in the fine and coarse particle size range (0.5–1.0 μm aerodynamic diameter). A field campaign conducted in Queens, New York City (Tong et al., 2015) indicated higher concentrations downwind of a vegetation barrier presumably because of decreased TKE downwind of the barrier.

Several modeling and wind-tunnel studies have been carried out to describe the effects of vegetation barriers on urban air pollution. Steffens et al. (2012) incorporated particle aerodynamics and deposition mechanisms into the Comprehensive Turbulent Aerosol Dynamics and Gas Chemistry (CTAG) model to examine the effects of vegetation barriers on roadway-emitted pollutants. They modeled the results of the field experiment conducted in Chapel Hill, NC (Hagler et al., 2012). They assumed that vegetation barriers affect near-road air quality in the following ways: (1) particles are deposited on leaf surfaces, (2) downwind wind speed and turbulence levels in the flow passing through the barrier are decreased, and (3) a fraction of the flow carrying pollutants is forced to go over the barrier. The first and the third effects reduce concentrations, while the second effect increases concentrations. Another computational fluid dynamics model developed by Vos et al. (2013) found that concentrations within street canyons are higher when trees are present. They found that the effect of vegetation in decreasing TKE is stronger than its filtration capacity; thus, vegetation increases local concentrations within street canyons. Wind tunnel studies conducted on the effects of trees within street canyons showed that trees increase concentrations at the leeward wall and decrease concentrations only slightly on the windward side (Gromke and Ruck, 2012).

So far, only a few studies have been performed that explicitly investigate the effects of a combination of vegetation and solid barrier on the air quality near roadways. Baldauf et al. (2008) conducted a field study in Raleigh, NC, which measured concentrations of traffic emissions downwind of a road where a clearing, a solid barrier, or a solid-vegetation barrier combination

were adjacent to three sections of the road. The results indicated that concentrations measured downwind of the solid-vegetation barrier were lower than those in the clearing or downwind of the solid barrier. A CFD model based on Large Eddy Simulation (LES) examined the effects of common vegetation barrier configurations near roadways to find the most effective configuration (Tong et al., 2016). The results indicated that a wide vegetation barrier with high leaf area density (LAD), and also a combination of vegetation and solid barrier, work best as mitigation strategies.

Model for a Solid-Vegetation Barrier

The tentative model presented here is based on a field study conducted in June 2016 to compare the effects of solid barriers and solid-vegetation combination barriers on the near-road concentrations of traffic-emitted pollutants. During 3 days, the ultrafine particle number concentration (UFP) and micrometeorology were measured simultaneously downwind of a solid barrier and a solid-vegetation combination barrier in Sacramento, CA, next to a freeway. Another set of instruments were installed at an upwind location. TSI 3022 condensation particle counters were used for the UFP measurement and Campbell Scientific CSAT3 sonic anemometers were used to measure the three components of wind speed, and the resulting data were processed to yield the mean wind speed and direction along with the surface friction velocity, sensible heat flux, and standard deviation of velocity fluctuations.

The turbulence levels downwind of the solid-vegetation barrier were smaller than those downwind of the solid barrier. The standard deviation of vertical velocity fluctuations, σ_w, downwind of the solid-vegetation barrier were 25% smaller than the corresponding values downwind of the solid barrier. The reduction in turbulence (σ_w) downwind of the solid-vegetation barrier relative to the solid barrier was larger for larger values of the turbulence at the site located upwind of the road.

The average concentration downwind of the solid-vegetation barrier was 13% lower than the corresponding value downwind of the solid barrier. Although the vegetation enhanced the mitigation effect of the solid barrier, this was not the case for all of the observed data.

The field data was interpreted with a modified version of the solid barrier model described earlier. The effects of vegetation were accounted for through three modifications: (1) the reduction of turbulence by the vegetation was modeled by multiplying the surface friction velocity by

the ratio of σ_w downwind of the solid-vegetation barrier to that downwind of the solid barrier, (2) the factor that accounted for the entrainment of material into the wake was reduced by the same ratio, and (3) the effective height of the wall was increased to account for additional plume lofting induced by the vegetation.

The evaluation of the model with measurements indicated that over 90% of the model estimates were within a factor of two of the corresponding observations, although the correlation was poor. The distributions of modeled values compared well with that of the observed UFP. The model shows that the barrier can reduce concentrations next to a road. Adding vegetation to a solid barrier increases the lofting effect of the barrier which leads to a further concentration reduction. Vegetation decreases downwind turbulence levels, which can lead to higher concentrations relative to those measured next to a road without barriers. Our observations indicated that adding vegetation decreases concentrations when the turbulence reduction was small which occurred over most of the sampling period. Increasing the upwind wind speed and turbulence also caused less reduction in concentration levels downwind of the solid-vegetation barrier.

SUMMARY

Existing models for dispersion of vehicle-emitted pollutants provide adequate descriptions of concentrations measured near the road when the receptor and the road are at the same level. These models can also account for the effects of roadside barriers. As shown in this chapter, we can model the effect of depressing a road by adding an initial vertical spread that is roughly equal to the depth of the depression.

It is useful to summarize some of the results presented in this chapter in terms of a simple model for dispersion of emissions from a highway. Chapter 3 (Eq. 3.85) tells us that the product of the vertical spread, σ_z, and the effective transport velocity, $U(\overline{z})$, varies linearly with distance from the source. This suggests that we can write the vertical plume spread as $\sigma_z = h_0 + \frac{\sigma_w x}{U}$, where x is the distance from the source, σ_w is the standard deviation of vertical velocity fluctuations near the road surface, and U is the near surface wind speed; the product $\sigma_z U$ varies linearly in the absence of h_0. Note that the surface wind speed, U, needs to be measured

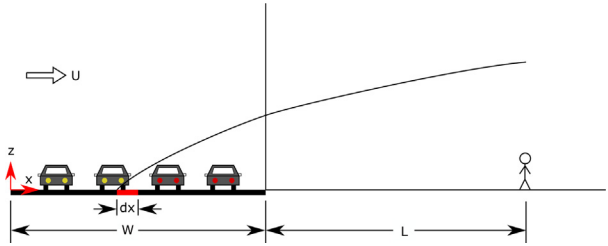

Figure 4.12 Schematic used to derive expression for concentration from a road of width, *W*, at a distance, *L*, from the downwind edge of road.

at a height that is a fraction of the vertical spread, which means that it varies with distance. In this simple analysis, we will ignore this subtlety, and assume that it is a constant.

Consider an infinitely long road with an emission rate, Q, of pollutant per unit length of the road, which can be expressed as $Q = e_f T$, where e_f is the emission factor and T is the traffic flow rate. Refer to Fig. 4.12 for the definition of the variables in the following discussion. Assuming that the emissions are spread over the width of the road, the emission rate from an element with width dx is $\frac{Q}{W}dx$ and the associated concentration at a distance L from the edge of the road is

$$dC(L) = \sqrt{\frac{2}{\pi}} \frac{Q dx}{WU\left(h_0 + \frac{\sigma_w(x+L)}{U}\right)}, \tag{4.26}$$

Integrating this expression between the limits $x = 0$ and $x = W$ yields the expression for the concentration at a downwind distance L from the edge of a road with a width, W

$$C(L) = \sqrt{\frac{2}{\pi}} \frac{Q}{W\sigma_w} \ln\left(1 + \frac{W}{L + \left(h_0 U/\sigma_w\right)}\right) \tag{4.27}$$

Even though the expression is only valid for winds perpendicular to the road and is an approximation, it provides insight into the factors that control dispersion of vehicle emissions close to the road. We see that the near-surface concentration is inversely proportional to σ_w, and the initial mixing is equivalent to adding the distance $h_0 U/\sigma_w$ to the distance L from the edge of the road. If we take $U/\sigma_w = 10$, an initial mixing of $h_0 = 2m$ shifts the road 20 m upwind from the receptor. Because a downwind barrier results in complete mixing below the barrier height, we can estimate the effect of a barrier on downwind concentrations by assuming

that h_0 is equal to the barrier height multiplied by $\sqrt{\frac{2}{\pi}}$, which accounts for the assumption of a Gaussian distribution of the vertical spread.

Eq. (4.27) can also be used to estimate the distance, L_s, at which concentration associated with the road emissions goes below a specified value, C_s. If we take $R = C_s/C(0)$, where $C(0)$ is the concentration at the downwind edge of the road, Eq. (4.28) yields

$$L_s = \frac{W}{\left[\left(1+\frac{W}{x_0}\right)^R - 1\right]} - x_0; \quad x_0 = \frac{h_0 U}{\sigma_w}. \tag{4.28}$$

Note that this "safe" distance, L_s, depends on the emissions from the road and the geometry of the road through the ratio, R, and the micrometeorology characterized by σ_w/U.

Several field studies have examined the impact of vegetation barriers on near-road concentrations. Some of them indicate that vegetation barriers can increase near-road concentrations relative to those in the absence of a barrier. This effect appears to be related to the reduction of turbulence in the air that flows through the vegetation. To see how this might happen, let us express the concentration downwind of a vegetation barrier, C_v, as a linear combination of the concentration, C_b, associated with the flow that goes over the barrier, and concentration, αC_f, associated with the flow that goes through the barrier. Here, C_f is the concentration in the absence of the barrier, and α is the enhancement caused by the turbulence reduction in the vegetation. Then

$$C_v = p\alpha C_f + (1-p)C_b, \tag{4.29}$$

where p is the fraction of the flow that goes through the barrier. Dividing both sides of the equation by C_f, we get the expression for the mitigation factor $R_v = C_v/C_f$ in terms of $R_b = C_b/C_f$ provided by the solid barrier,

$$R_v = p(\alpha - R_b) + R_b. \tag{4.30}$$

Because $\alpha \geq 1$ in the absence of deposition, $R_v \geq R_b$: the vegetation barrier produces less mitigation than a solid barrier. Also, the concentration can be larger than that without the barrier if α and p are large enough. If we assume that vegetation can reduce turbulence levels, vegetation on top of a solid barrier can enhance the effect of the solid barrier by reducing entrainment of the pollutant into the wake of the solid barrier. At this stage, we do not have a model that provides a satisfactory description of these effects.

REFERENCES

Ahangar, F.E., Heist, D., Perry, S., Venkatram, A., 2017. Reduction of air pollution levels downwind of a road with an upwind noise barrier. Atmos. Environ. 155, 1–10. Available from: https://doi.org/10.1016/j.atmosenv.2017.02.001.

Al-Dabbous, A.N., Kumar, P., 2014. The influence of roadside vegetation barriers on airborne nanoparticles and pedestrians exposure under varying wind conditions. Atmos. Environ. 90, 113–124.

Baldauf, R., Thoma, E., Khlystov, A., Isakov, V., Bowker, G., Long, T., et al., 2008. Impacts of noise barriers on near-road air quality. Atmos. Environ. 42, 7502–7507. Available from: https://doi.org/10.1016/j.atmosenv.2008.05.051.

Baldauf, R.W., Heist, D., Isakov, V., Perry, S., Hagler, G.S.W., Kimbrough, S., et al., 2013. Air quality variability near a highway in a complex urban environment. Atmos. Environ. 64, 169–178. Available from: https://doi.org/10.1016/j.atmosenv.2012.09.054.

Becker, S., Lienhart, H., Durst, F., 2002. Flow around three-dimensional obstacles in boundary layers. J. Wind Eng. Ind. Aerodyn. 90, 265–279.

Berkowicz, R., 2000. OSPM – a parameterised street pollution model. Environ. Monit. Assess. 65, 323–331. Available from: https://doi.org/10.1023/A:1006448321977.

Brantley, H.L., Hagler, G.S.W., Deshmukh, P.J., Baldauf, R.W., 2014. Field assessment of the effects of roadside vegetation on near-road black carbon and particulate matter. Sci. Total Environ. 468–469, 120–129.

Calder, K.L., 1973. On estimating air pollution concentrations from a highway in an oblique wind. Atmos. Environ. 7, 863–868.

Carruthers, D.J., Holroyd, R.J., Hunt, J.C.R., Weng, W.-S., Robins, A.G., Apsley, D.D., Thompson, D.J., Smith, F.B., 1994. UK-ADMS: a new approach to modelling dispersion in the earth's atmospheric boundary layer. J. Wind Eng. Ind. Aerodyn. 52, 139–153.

Cimorelli, A.J., Perry, S.G., Venkatram, A., Weil, J.C., Paine, R.J., Wilson, R.B., Lee, R.F., Peters, W.D., Brode, R.W., 2005. AERMOD: a dispersion model for industrial source applications. Part I: general model formulation and boundary layer characterization. J. Appl. Meteorol 44 (5), 682–693.

Feeney, P.J., Cahill, T.A., Flocchini, R.G., Eldred, R.A., Shadoan, D.J., Dunn, T., 1975. Effect of roadbed configuration on traffic derived aerosols. J. Air Pollut. Control Assoc. 25, 1145–1147. Available from: https://doi.org/10.1080/00022470.1975.10470190.

Finn, D., Clawson, K.L., Carter, R.G., Rich, J.D., Eckman, R.M., Perry, S.G., et al., 2010. Tracer studies to characterize the effects of roadside noise barriers on near-road pollutant dispersion under varying atmospheric stability conditions. Atmos. Environ. 44, 204–214. Available from: https://doi.org/10.1016/j.atmosenv.2009.10.012.

Gromke, C., Ruck, B., 2012. Pollutant concentrations in street canyons of different aspect ratio with avenues of trees for various wind directions. Bound.-Layer Meteorol 144, 41–64. Available from: https://doi.org/10.1007/s10546-012-9703-z.

Hagler, G.S.W., Lin, M.Y., Khlystov, A., Baldauf, R.W., Isakov, V., Faircloth, J., et al., 2012. Field investigation of roadside vegetative and structural barrier impact on near-road ultrafine particle concentrations under a variety of wind conditions. Sci. Total Environ. 419, 7–15. Available from: https://doi.org/10.1016/j.scitotenv.2011.12.002.

Heist, D.K., Perry, S.G., Brixey, La, 2009. A wind tunnel study of the effect of roadway configurations on the dispersion of traffic-related pollution. Atmos. Environ. 43, 5101–5111. Available from: https://doi.org/10.1016/j.atmosenv.2009.06.034.

Hooghwerff, J., Tollenar, C.C., Van der Heijden, W.J., 2010. In-situ air quality measurements on existing and innovative noise barriers. Presented at the International Conference on Modelling, Monitoring and Management of Air Pollution, WIT Press, Kos, Greece, pp. 129–139.

Iser, F., Scharl, C., 2009. EU-LIFE Projekt SPAS Task 3: Simulationen Abschlussbericht.
Kalthoff, N., Bäumer, D., Corsmeier, U., Kohler, M., Vogel, B., 2005. Vehicle-induced turbulence near a motorway. Atmos. Environ. 39, 5737–5749. Available from: https://doi.org/10.1016/j.atmosenv.2004.06.048.
Luhar, K.A., Patil, R.S., 1989. A general finite line source model for vehicular pollution prediction. Atmos. Environ. 23, 555–562.
McNaughton, K.G., 1988. 1. Effects of windbreaks on turbulent transport and microclimate. Agric. Ecosyst. Environ. 22–23, 17–39. Available from: https://doi.org/10.1016/0167-8809(88)90006-0.
Petroff, A., Mailliat, A., Amielh, M., Anselmet, F., 2008. Aerosol dry deposition on vegetative canopies. Part I: Review of present knowledge. Atmos. Environ. 42, 3625–3653. Available from: https://doi.org/10.1016/j.atmosenv.2007.09.043.
Rodler, J., Henn, M., 2009. Filter Effect of SPAS and Impact on Air Quality.
Schulman, L.L., Strimaitis, D.G., Scire, J.S., 2000. Development and evaluation of the PRIME pume rise and building downwash model. J. Air Waste Manag. Assoc. 50, 378–390. Available from: https://doi.org/10.1080/10473289.2000.10464017.
Schulte, N., Snyder, M., Isakov, V., Heist, D., Venkatram, A., 2014. Effects of solid barriers on dispersion of roadway emissions. Atmos. Environ. 97, 286–295. Available from: https://doi.org/10.1016/j.atmosenv.2014.08.026.
Setälä, H., Viippola, V., Rantalainen, A.-L., Pennanen, A., Yli-Pelkonen, V., 2013. Does urban vegetation mitigate air pollution in northern conditions? Environ. Pollut. Barking Essex 1987 (183), 104–112. Available from: https://doi.org/10.1016/j.envpol.2012.11.010.
Snyder, M.G.M.G., Venkatram, A., Heist, D.K.D.K., Perry, S.G.S.G., Petersen, W.B.W.B., Isakov, V., 2013. RLINE: a line source dispersion model for near-surface releases. Atmos. Environ. 77, 748–756. Available from: https://doi.org/10.1016/j.atmosenv.2013.05.074.
Steffens, J.T., Heist, D.K., Perry, S.G., Isakov, V., Baldauf, R.W., Zhang, K.M., 2014. Effects of roadway configurations on near-road air quality and the implications on roadway designs. Atmos. Environ. 94, 74–85.
Steffens, J.T., Wang, Y.J., Zhang, K.M., 2012. Exploration of effects of a vegetation barrier on particle size distributions in a near-road environment. Atmos. Environ. 50, 120–128. Available from: https://doi.org/10.1016/j.atmosenv.2011.12.051.
Tong, Z., Baldauf, R.W., Isakov, V., Deshmukh, P., Max Zhang, K., 2016. Roadside vegetation barrier designs to mitigate near-road air pollution impacts. Sci. Total Environ. 541, 920–927. Available from: https://doi.org/10.1016/j.scitotenv.2015.09.067.
Tong, Z., Whitlow, T.H., MacRae, P.F., Landers, A.J., Harada, Y., 2015. Quantifying the effect of vegetation on near-road air quality using brief campaigns. Environ. Pollut. 201, 141–149. Available from: https://doi.org/10.1016/j.envpol.2015.02.026.
Venkatram, A., Horst, T.W.W., 2006. Approximating dispersion from a finite line source. Atmos. Environ. 40, 2401–2408. Available from: https://doi.org/10.1016/j.atmosenv.2005.12.014.
Venkatram, A., Snyder, M., Isakov, V., Kimbrough, S., 2013. Impact of wind direction on near-road pollutant concentrations. Atmos. Environ. 80, 248–258. Available from: https://doi.org/10.1016/j.atmosenv.2013.07.073.
Vos, P.E.J., Maiheu, B., Vankerkom, J., Janssen, S., 2013. Improving local air quality in cities: to tree or not to tree? Environ. Pollut. 183, 113–122. Available from: https://doi.org/10.1016/j.envpol.2012.10.021.
Wang, H., Takle, E.S., 1995. A numerical simulation of boundary-layer flows near shelterbelts. Bound.-Layer Meteorol. 75, 141–173. Available from: https://doi.org/10.1007/BF00721047.

FURTHER READING

Amini, S., Ahangar, F.E., Schulte, N., Venkatram, A., 2016. Using models to interpret the impact of roadside barriers on near-road air quality. Atmos. Environ. 138, 55–64. Available from: https://doi.org/10.1016/j.atmosenv.2016.05.001.

Magistrat Klagenfurt, 2011. EU-LIFE project SPAS [WWW Document]. URL http://www.life-spas.at.

Raupach, M.R., Woods, N., Dorr, G., Leys, J.F., Cleugh, H.A., 2001. The entrapment of particles by windbreaks. Atmos. Environ. 35, 3373–3383. Available from: https://doi.org/10.1016/S1352-2310(01)00139-X.

Venkatram, A., Snyder, M.G., Heist, D.K., Perry, S.G., Petersen, W.B., Isakov, V., 2013b. Re-formulation of plume spread for near-surface dispersion. Atmos. Environ. 77, 846–855. Available from: https://doi.org/10.1016/j.atmosenv.2013.05.073.

CHAPTER FIVE

The Impact of Buildings on Urban Air Quality

Contents

Introduction 105
Primary Effects of Buildings on Dispersion of Traffic Emissions 108
- The Impact of Buildings on Mean Winds and Turbulence Within the Urban Canopy 110
- Vortex Flow and Street Canyons 112
- Challenges for Practical Application of Models of Building Effects on Dispersion 115
- Primary Variables Governing Dispersion in Cities 117

Models for the Effects of Buildings 119
- Operational Street Pollution Model 119
- Vertical Dispersion Model 121

Comparison of Model with Observations 124
- Description of the Los Angeles Field Measurements 125
- Evaluation of the VDM with Data Collected in Los Angeles and Riverside 127

Summary 133
References 135
Further Reading 136

INTRODUCTION

A major challenge facing air pollution regulators and researchers is the need to better characterize the factors that influence exposure to traffic emissions in cities. Early studies of exposure and health effects relied on estimates of exposure concentrations at a person's home location. However, studies that recorded a person's actual exposure using mobile personal exposure monitors that were carried by the subject showed that the personal exposure could be significantly higher than the exposure implied by the measured or modeled concentration at the person's home. These studies concluded that an individual's daily activities and the time spent within microenvironments associated with elevated concentrations

Urban Transportation and Air Pollution.
DOI: https://doi.org/10.1016/B978-0-12-811506-0.00005-1

are important factors that determine actual exposure. The exposure varies depending on the degree to which traffic sources influence the exposure concentrations within the person's home, work, school, and commute microenvironments. The subject of this chapter is the impact that the urban built environment has on exposure concentrations. Buildings tend to reduce dispersion and thus create hot spots associated with elevated concentrations of traffic emissions. In this chapter, we show practical methods to model these hot spot concentrations.

The need to employ accurate models of exposure to traffic emissions is driven by policies aimed at increasing high-density development within cities. These policies, which are meant to reduce greenhouse gas emissions from transportation, rely on reducing vehicle miles traveled to achieve desired reductions in fossil fuel consumption. To accomplish this, the policies incorporate plans for development that place high-density housing in close proximity to businesses and transportation infrastructure. These designs are often called sustainable communities or transit-oriented development (TOD) and are desirable because they promote walking, cycling, and use of public transportation, all of which reduce use of motor vehicles and the associated pollutant and greenhouse gas emissions. However, there is concern that these community designs create pollutant hot spots next to high-density built-up areas, which can reduce dispersion and thus magnify the concentrations of vehicle-emitted pollutants.

The impact of the presence of buildings near the road on dispersion of traffic emissions is manifested at multiple spatial scales ranging from the city scale to the scale of individual buildings. When viewed at the city scale, the effect of the buildings is to increase the surface roughness length and surface heat flux of the city relative to that produced by vegetation and natural terrain, and the resulting impact on mean winds and turbulence translates into modified dispersion relative to the flat terrain models presented in Chapter 3. The urban canopy refers to the region between the ground and the average height of urban buildings. The winds and turbulence within the urban canopy are dominated by the drag force of the buildings. At spatial scales on the order of the building height, individual buildings induce wake flows and recirculating vortices. The combination of these effects modifies the dispersion of traffic emissions with the result that concentrations are significantly different from those that would be observed in rural environments. This has significant implications for the design and

application of regulatory and research dispersion models for estimating the impact of roadways on exposure concentrations in cities.

Regulatory and research dispersion models account for the primary effects of buildings on dispersion using varying approximations, and the models can be classified according to the type of physical phenomena they describe and the spatial resolution they treat. The US EPA regulatory model AERMOD (Cimmorelli et al., 2005) incorporates the effects of buildings at the neighborhood and city scale. AERMOD uses the city population to estimate the enhanced positive heat flux and the increased boundary layer height due to convection that occurs in urban areas during nighttime. These boundary layer parameters are translated into increased turbulence and dispersion during nighttime in urban areas. AERMOD includes the PRIME algorithm that estimates plume downwash in building wakes. However, PRIME is designed for isolated point sources near single buildings and thus is not applicable to estimating the impact of buildings on dispersion of roadway emissions at the street scale.

Thus, in the United States, application of models of building effects at the street scale has been limited primarily to research use. Europe has seen more widespread use of these models for both research and operational applications such as routine air quality forecasting. The most well-known example of the operational models is the Operational Street Pollution Model (OSPM, Berkowicz et al., 1997), developed by the Danish National Environmental Research Institute. OSPM is a street canyon model; Street canyons are streets with tall buildings on either side, the building walls thus forming a canyon. The driving flow above the top of the buildings induces recirculating vortex flows within the canyon, leading to trapping of pollutants within the street. Street canyon models describe dispersion at the scale of individual streets and thus the spatial resolution of these models is 10−100 m. We will discuss more about street canyon models and OSPM in the next section.

In this chapter, we show how the primary effects of buildings on dispersion are incorporated into semiempirical models. The models discussed are useful for estimating the near-road concentration of traffic emissions in urban areas. We focus on the street scale, with an associated spatial resolution of 10−100 m, which is the scale at which roadways impact near-road environment. We begin by reviewing the relevant experimental and modeling studies and describing the physical effects of buildings on dispersion of traffic emissions. Next, we present the formulation of dispersion models that account for these effects. The model development focuses on two models:

OSPM and the Vertical Dispersion Model (VDM). OSPM is included because of its position as a well-known model that can be considered a prototype for the class of street canyon models that describe dispersion within the urban near-road environment. However, OSPM is primarily designed for European cities, whose streets tend to closely match the idealized street canyon model. Cities with nonuniform building heights and spatial inhomogeneity tend to have wind and turbulence patterns that are inconsistent with the street canyon model formulation. Additionally, it is difficult to define the model input parameters needed for street canyon models when the building geometry does not match the street canyon prototype. We make the case that VDM is useful for describing dispersion in spatially inhomogeneous cities with nonuniform building heights, such as those often found in urban cores in the United States. Finally, we describe the evaluation of VDM with observations.

PRIMARY EFFECTS OF BUILDINGS ON DISPERSION OF TRAFFIC EMISSIONS

This section reviews the primary effects of buildings on dispersion. The governing physical processes are active at different spatial or temporal scales, and thus models for these processes are built to match these scales. The effects of buildings occur at spatial scales including the street scale, 10−100 m, the neighborhood scale, 100 m−1 km, the urban background scale, 1−10 km, and the regional scale, 10−100 km. Models for the effects of buildings at each scale are combined in a hierarchy, with the smaller scales providing the most local detail and with these small-scale effects being parameterized using simplifications within the larger scale models. This chapter describes models of the near-road concentrations of traffic emissions, and thus this section focuses on effects that occur at the street scale. Chapter 6 reviews effects that occur at larger spatial scales and describes models of the impact of buildings on dispersion at these scales. We first give an overview of the important physics ranging from street to urban background scales to provide context for the present discussion.

Our discussion of the effects of buildings at different spatial scales is in part modeled on that provided by Britter and Hanna (2003). Fig. 5.1 shows a schematic of the effects of buildings after a transition from a rural area with low surface roughness length into the urban area. When viewed at the city

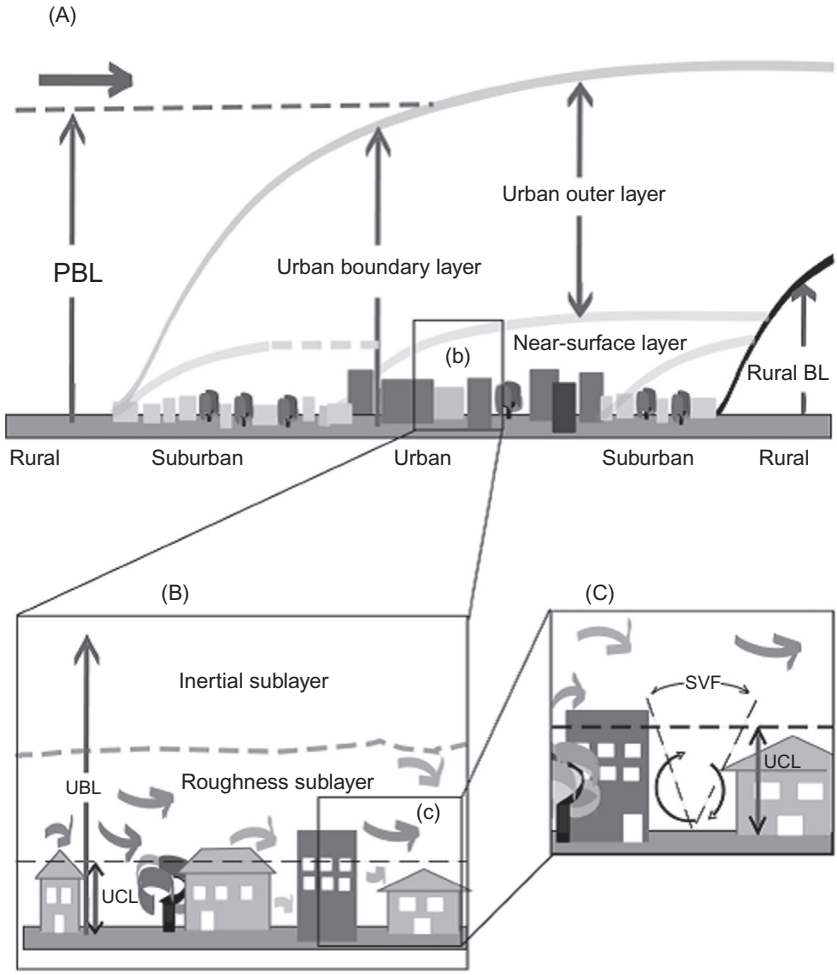

Figure 5.1 Schematic showing the effects of buildings at different spatial scales. Schematic is taken from Fisher et al. (2006). (A) Mesoscale; (B) local scale; and (C) microscale. PBL refers to the planetary boundary layer height.

scale, the impact of individual buildings on the flow and dispersion is averaged out and thus the buildings can be described using statistical parameters. At this scale, the primary impact of the built environment is through modifications of the drag force and the surface energy balance. As air flows from the upwind rural, low surface roughness area into the city, a region develops where the wind is modified due to the increased drag applied by the buildings. The zone where the wind speed is modified is the internal boundary layer (IBL). The height of the IBL grows with distance from the rural–urban

boundary. The wind that has adjusted to the urban surface roughness conditions is the urban boundary layer (UBL). The UBL can be divided into regions where different physical processes dominate. The near-surface UBL flow is described by the roughness sublayer and the inertial sublayer, similar to the way we describe flow over a rural surface. The roughness sublayer is the region, up to a few building heights from the ground, where the dominant length scale is the building height, and the flow is dominated by the effects of the building "roughness elements." Thus, the flow within the roughness sublayer is horizontally inhomogeneous. Above the roughness sublayer is the inertial sublayer, where the dominant length scale is the height from the ground, and similarity profiles can be used to model the wind, displaced upward by an amount proportional to the building height and with the surface roughness determined by building morphology. Models for these effects are described in more detail in Chapter 6. In this section, we focus on the region below the top of the buildings, called the urban canopy layer (UCL). This is the region where the physics of dispersion that governs the near-road concentration within an individual street is active. The UCL is the region described by street canyon dispersion models.

The effect of the buildings at scales larger than the street scale is usually parameterized using statistical measures of the building morphology. These measures typically include the average building height and measures of the building density, including the frontal and plan area fractions (Oke, 1988). The frontal area fraction, $\lambda_f = A_f/A_d$, is the ratio of the frontal area of the obstacles perpendicular to the mean wind direction, A_f, to the ground surface area occupied by the city, A_d. Thus, this parameter describes the building area upon which the drag force acts per unit area of the city. The plan area fraction is the fraction of ground surface area occupied by the buildings, $\lambda_p = A_p/A_d$, where A_p is the area of the buildings when viewed from the top. The area fractions are often used to describe the wind and turbulence within the UCL.

The Impact of Buildings on Mean Winds and Turbulence Within the Urban Canopy

The mean winds and turbulence within the UCL have several key characteristics that significantly influence the dispersion of traffic emissions. First, the mean wind speeds are small compared with winds in rural areas because of the drag force that the buildings exert on the air flow. Second, turbulence levels tend to be increased relative to those in the rural area. The result of the increased turbulence and low winds is that pollutant

plumes in urban areas exhibit significant horizontal meandering due to large, relative to the mean wind, lateral turbulent fluctuations. Finally, building wakes generate strong upward and downward flows as well as vortex flows. These flows form the basis of street canyon dispersion models. We begin by discussing the impact of the buildings on mean winds and turbulence within the urban canopy.

Mean winds and turbulence within the roughness sublayer and the urban canopy are usually described using statistical methods. Thus, while the flow around individual buildings is strongly influenced by the local building geometry, we can develop models to describe the horizontally averaged winds and turbulence within the roughness sublayer and the urban canopy. This horizontal averaging requires that the statistical parameters describing the buildings are horizontally homogeneous over the spatial averaging area. Thus, the city may be divided into regions where average values of the parameters such as the surface roughness length, building height, and area fractions can be assigned. The change in surface roughness of these regions is associated with the formation of an IBL and the adjustment of the wind and shear stress within and above the canopy to the new equilibrium values. For the assumption that the wind adjusts to the new surface conditions to be valid, the horizontal size of the spatial averaging region should be on the order of several building heights.

Buildings exert a drag force on the flow. The resulting shear stress has a maximum near the top of the buildings (Cheng and Castro, 2002; MacDonald, 2000) and then decreases to zero below the height of the buildings. The shear stress near the building tops is associated with a sharp gradient in the mean wind speed and the low shear stress within the urban canopy is associated with a nearly constant wind speed (with height) near the ground. Based on these observations, a simple approach to determine the wind speed within the canopy is to assume a constant (with height) wind speed. By matching the shear stress of the inertial sublayer with the drag force of the buildings, we can relate this wind speed with the parameters of the inertial sublayer and building geometry. Bentham and Britter (2003) developed a relationship between the constant spatially averaged canopy velocity, U_c, the surface friction velocity of the inertial sublayer above the urban area, u_*, and the frontal area fraction of the buildings:

$$\frac{U_c}{u_*} = \left(\frac{2}{\lambda_f}\right)^{1/2} \tag{5.1}$$

The wind within the UCL is often modeled using concepts similar to those of forest canopies. The work on modeling vegetation canopies has been translated for applications to the UCL by MacDonald (2000). By allowing the wind speed to vary with height, these models predict an exponential variation of the wind speed with height (MacDonald, 2000):

$$U(z) = U_H e^{(z-H)/l} \tag{5.2}$$

where U_H is the velocity at the building height and l is a length scale proportional to the building height that determines how deep the rooftop wind penetrates into the urban canopy. MacDonald derives relationships between these parameters and the building frontal and plan area fractions.

Another approach is to use empirical relationships between street and roof wind speed and turbulence. Several field experiments have provided data for this approach (Allwine et al., 2002; Hanna et al., 2007; Rotach et al., 2005).

Vortex Flow and Street Canyons

Some of the earliest studies of dispersion in cities were performed in 1970 and 1971 in San Jose, California, and St Louis, Missouri (Johnson et al., 1973). The studies resulted in a semiempirical dispersion model based on the Gaussian plume model along with a "submodel" that accounts for the microscale features of the dispersion within the urban street. The plume spreads for the Gaussian plume model were determined from tracer release field measurements in a study conducted in St Louis between 1963 and 1965.

The microscale model of (Johnson et al., 1973) and most semiempirical urban dispersion models are based on the picture of the "street canyon," a street with uniform height buildings on either side, a prototypical building block of the urban environment. Fig. 5.2 shows a schematic of a street canyon model. The ideal street canyon has buildings all the same height and no gaps between the buildings. Depending on the aspect ratio, the ratio of the height of buildings to the street width, and the rooftop wind speed and direction, a recirculating vortex flow can develop within the street (Oke, 1988). The physical picture of the dispersion within street canyons typically includes a model of the vortex flow. This model primarily determines the relationship between the near-road concentration and the governing meteorological variables.

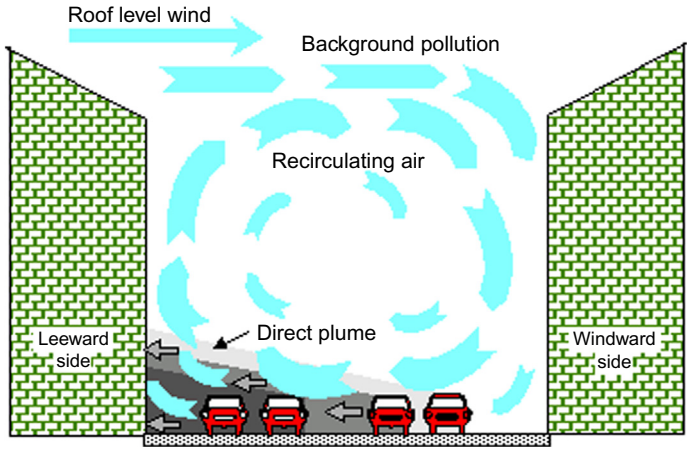

Figure 5.2 Berkowicz, R., 2000. OSPM — a parameterised street pollution model. Environ. Monit. Assess. 65, 323–331 (Figure 1. Schematic illustration of flow and dispersion conditions in street canyons.)

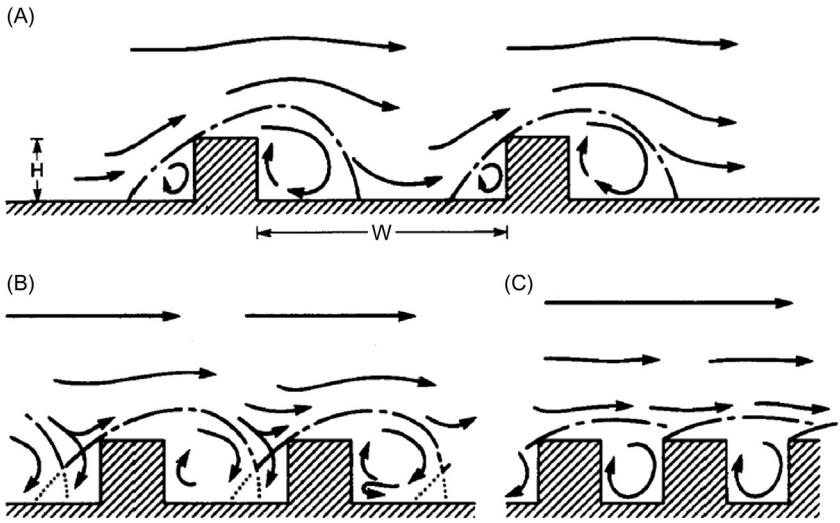

Figure 5.3 Building array flow regimes. (A) Isolated roughness flow; (B) wake interference flow; and (C) skimming flow. Taken from (Oke, 1988).

The existence of a vortex within the street canyon depends on the aspect ratio, the ratio of building height to street width. When the aspect ratio is small, no consistent vortex forms within the canyon, and when the aspect ratio is large, multiple vortices may form. Oke (1988) groups the flow regime within building arrays into the following classes based on

the canyon aspect ratio (Fig. 5.3): isolated roughness flow—the wakes downwind of individual obstacles do not interfere with each other; wake interference flow—the wakes behind obstacles are the same size as the distance between obstacles and begin to interfere with each other; skimming flow—a stable circulation forms within the canyon and the bulk of the flow does not enter the canyon.

For a long street canyon, the change from isolated roughness to wake interference flow occurs around an aspect ratio of 0.3, and the change from wake interference to skimming flow occurs around an aspect ratio of 0.75. The street canyon vortex may disappear under low ambient wind speeds. DePaul and Sheih (1986) verified the existence of a vortex flow using neutrally buoyant balloons as tracers. They found that the vortex disappears when the ambient wind speed is less than 1.5–2 m/s.

One early field study was conducted in a street canyon in San Jose, CA in 1973 (Johnson et al., 1973). Carbon monoxide concentrations and wind speed were measured at several locations and at five different heights within the canyon. The researchers found that the concentrations at the leeward side of the canyon were 3–4 ppm (33%–66%) larger than those at the windward side when the wind blows perpendicular to the canyon, while under parallel flow, the concentrations are similar at both sides. The vertical concentration gradient is smaller at the windward side. The authors show that the ground-level concentration at the leeward side is related to the rooftop wind speed, traffic count, and street geometry as follows:

$$C_L = C_b + \frac{0.07N}{(U + 0.5)(2 + x)} \tag{5.3}$$

where C_b is the background concentration, N is the traffic count, x is the distance from the traffic lane to the receptor, and U is the wind speed. A similar form holds for the windward side, with $2 + x$ replaced by the street width. The factor of 0.5 in the denominator accounts for the effect of vehicle induced turbulence. This model indicates that changes in building height do not directly alter the concentration, and only the street width and rooftop wind speed determine dispersion.

Wind tunnel models of street canyons have shown the same relationship between wind speed and pollutant dilution as was found in the previously mentioned field studies. Meroney et al. (1996) found that the concentration was inversely related to the approach wind speed. Barlow and Belcher (2002) found that the entrainment velocity that mixes pollutants vertically is proportional to the wind speed above the canyon. Both

studies tested the effect of increasing the surface roughness upstream of the canyon to simulate real urban conditions. Meroney et al. (1996) found that the presence of upstream buildings creates a displacement of the incoming velocity profile, which causes the formation of a shear layer at the top of the canyon and results in a permanent recirculating eddy within the canyon (with aspect ratio 1), while the small upstream roughness case shows an intermittent eddy for the same canyon. The presence of upstream buildings thus results in trapping of pollutants within the permanent recirculating eddy, resulting in larger concentrations relative to those in the absence of buildings. For smaller aspect ratios, the presence of upstream buildings is less important.

These studies show the importance of the rooftop wind speed in determining dispersion in street canyons. Other studies indicate that the vertical pollutant transport occurs due to an unstable shear layer that develops at the top of the canyon (Louka et al., 2000). The unsteady fluctuations of the shear layer cause intermittent recirculation in the canyon, thus intermittently flushing pollutants out of the canyon. The street canyon studied by Louka et al. (2000) was mostly isolated, with only three buildings upwind of the canyon. The reason for the very intermittent vortex flow in this experiment may be similar to that for the Meroney et al. (1996) wind tunnel study, where the isolated street canyon had a more unsteady vortex than the canyon surrounded by urban roughness.

Some of the existing work on modeling street canyons is summarized by Vardoulakis et al. (2003). Existing models can be classified as: empirical regression models, semiempirical box models, semiempirical Gaussian plume models, Lagrangian particle models, unsteady Gaussian puff models, and computational fluid dynamics (CFD) models. We are most interested in the semiempirical box and Gaussian plume models because they require only easily measured input variables and capture only the essential mechanisms of dispersion in cities. CFD models are capable of simulating dispersion in cities, but they do not provide clear insight into the important mechanisms.

Challenges for Practical Application of Models of Building Effects on Dispersion

There are several difficulties in applying semiempirical street canyon dispersion models to model dispersion in real-world cities. One problem with dispersion models based on the street canyon model is that it is not clear that they are applicable to real-world urban streets with significant

building height variability and spatial inhomogeneity. Well-known street canyon dispersion models have been evaluated mostly with data collected in European cities, where medium density urban streets tend to closely approximate the ideal street canyon. Dense urban cores within the United States have significant spatial and building height variability, putting into question the applicability of the street canyon dispersion models to these urban environments.

A further challenge facing application of urban dispersion models is that there is little consensus on the meteorological variables that are most relevant for application to near-road dispersion model parameterizations. The STREET model of Johnson et al. (1973), which is similar to the model of Dabberdt et al. (1973), parameterizes the concentration in terms of the near surface wind speed within the street, which is linearly related to the rooftop wind speed in the model formulation. Nicholson (1975) developed a model that parameterizes concentrations in terms of the average vertical velocity near the top of the street canyon when the wind is perpendicular to the street. For parallel winds, the average horizontal wind speed within the canyon is used. For conditions of low within-canyon wind speeds, the canyon plume box model (CPBM) of Yamartino and Wiegand (1986) parameterizes pollutant transport using a Gaussian plume model with plume spreads determined by the average vertical and horizontal turbulent velocities within the street canyon. The OSPM (Berkowicz et al., 1997) relates the surface concentration with both the vertical turbulent velocity near the surface and the roof of the canyon.

Vortex flow within a street canyon may result in higher concentrations on one side of the street than the other. Most street canyon models describe the spatial variation of concentrations within the street by accounting for the vortex flow that advects emissions from the street toward the leeward side (Berkowicz et al., 1997; Johnson et al., 1973; Yamartino and Wiegand, 1986). These models typically include a parameterization of the "recirculating" contribution, which affects the concentration on both the windward and leeward sides of the street, and is due to the vortex flow trapping pollutants within the canyon, and the "direct" contribution, which impacts on the leeward side of the street, due to direct emissions advected across the street. Other models such as that of Nicholson (1975) only parameterize the average concentration within the canyon. As mentioned previously, the vortex flow model may not be appropriate for cities with significant spatial inhomogeneity. We examine

the value of this aspect of the vortex flow concept as part of the dispersion model evaluation.

A significant challenge to the application of dispersion models to urban environments is the lack of routine measurements of the required meteorological data inputs. Because of this, models rely on assumptions about the relationships between available data and the required model inputs. The street canyon model of Dabberdt et al. (1973) parameterizes the concentration in terms of the rooftop wind speed. The rooftop wind speed used in the model is estimated from the wind speed measured at a nearby airport. This simple parameterization results from the need to use routinely measured wind speed as model inputs. Normally, only measurements of mean wind speed and direction are made at rural locations such as airports. Turbulence levels are not routinely measured, and even mean wind speed and direction data is usually not available within dense urban centers. For these reasons, all of the urban dispersion models require such parameterizations to be applicable to real world situations. The semiempirical models that we describe in this chapter are developed with the requirement that they only depend on meteorological data that are readily available or can be determined through semiempirical models that relate the wind speed measured at the "rural" airport site to that at the urban site of interest.

Primary Variables Governing Dispersion in Cities

We now examine the primary variables that govern near-road pollutant concentrations in cities. We present the discussion in the context of an analysis of near-road concentration data using several dispersion models. The relationship between vehicle-related concentrations in a street and associated micrometeorology was formulated through an analysis of data collected by the Lower Saxony Ministry for Environment, Energy, and Climate, in Göttinger Straße, Hanover, Germany, during 2003–2007. Göttinger Str. is 25 m wide with 20 m-tall buildings on either side. Measurements of NO and NO_2 concentrations were made at two locations: one on the southwest side of the road 1.5 m above ground level (AGL) and the other on the southwest building rooftop above the surface monitor. Wind speed and turbulence measurements were made using a sonic anemometer near the surface concentration monitor at 10 m AGL, and mean winds were measured near the rooftop monitor at 42 m AGL. Traffic flow measurements were made with automatic

counters, and were converted into emission rates using emission factors of 0.465 and 6.18 g/km of NO_x for passenger cars and trucks, respectively, determined using EMFAC 2007 (California Air Resources Board, 2017). We used the average emission factors for light and heavy duty trucks for the truck portion of the traffic and that for light-duty vehicles for the passenger car portion.

We used the Göttinger Strasse data to evaluate several alternative dispersion models with different dependence on the surface and rooftop σ_w and wind speed. We treat the rooftop concentration as the urban background, so that the difference between street and roof concentrations is the local contribution estimated by the models. We used the NO_x concentration measurements for model comparison because NO_x emission factors are relatively well known.

Our discussion of the variables governing dispersion in cities is framed in terms of an analysis of several alternative models. The first model is a modified form of the OSPM direct contribution model and is described by Eq. (5.4), where h_0 is the initial vertical plume spread, q is the emission rate per unit length of road, σ_{ws} is the near surface standard deviation of vertical velocity fluctuations, U_s is the near surface wind speed, W is the road width, and w is the distance of the receptor from the side of the road.

$$C = \sqrt{\frac{2}{\pi}} \frac{q}{W\sigma_{ws}} ln\left(1 + \frac{\sigma_{ws} W}{h_0 U_s + \sigma_{ws} w}\right) \tag{5.4}$$

If the initial vertical plume spread is negligible compared with the plume spread due to atmospheric turbulence at the position of the receptor, $\sigma_{ws} w / U_s h_0 >> 1$, then the direct concentration is described by Eq. (5.5), where a term with logarithmic dependence on the street width has been neglected.

$$C = \sqrt{\frac{2}{\pi}} \frac{q}{W\sigma_{ws}} \tag{5.5}$$

The models of Eqs. (5.4) and (5.5) are insensitive to the initial vertical plume spread. To examine the influence of the initial vertical plume spread, we assumed that the concentration is well mixed below the height h_0, and follows a Gaussian shape above h_0. Then the concentration near the surface is described by Eq. (5.6), where L is the length of the street upwind of the receptor.

$$C = \sqrt{\frac{2}{\pi}}\frac{q}{\sigma_{ws} w}\left(1 + \sqrt{\frac{2}{\pi}}\frac{h_0 U_s}{L\sigma_{ws}}\right)^{-1} \tag{5.6}$$

A comparison of model estimates from these three models with measurements from Gottinger Strasse showed that the simplest model, Eq. (5.5), provided the best description of the data. This equation is consistent with the scaling suggested by Kastner-Klein et al. (2003), who found that σ_w is a better scaling velocity than U_s for the concentration.

MODELS FOR THE EFFECTS OF BUILDINGS

The previous section described the important physical effects that buildings have on the transport of pollutants within cities. We now show how models of the dispersion of traffic emissions can be constructed. The discussion is focused on two models, the OSPM and the VDM. OSPM is widely used and is recognized as the state-of-the-art operational near-road dispersion model by the European air pollution research community within which it was developed. It has been evaluated extensively with observed concentrations of traffic emissions in several cities, primarily in Europe. The model design is based on the idealized street canyon formulation, commonly found in the cities of Europe from which the model originated. However, this may limit the models usefulness for streets that do not fit the assumptions of the street canyon model. The second model, VDM, is designed to estimate dispersion in streets characterized by non-uniform building heights and spatial inhomogeneity, features characteristic of cities in North America.

Operational Street Pollution Model

OSPM combines a street canyon box model with a model of the dispersion of the direct emissions from the road. The recirculating vortex flow advects emissions from the road toward the leeward side of the street. The emissions are then mixed vertically, and are trapped within the canyon by the vortex flow. Exchange of the trapped pollutants with the air above the canyon occurs by vertical turbulent transport, the magnitude of which is controlled by the standard deviation of vertical velocity

fluctuations at the roof level. To model these features of the dispersion, OSPM separates the concentration into two components: the recirculating component and the direct component (see Fig. 5.2).

For the direct component, the vertical plume spread, σ_z, is given by:

$$\sigma_z = h_0 + \sigma_{ws} x / U_s \tag{5.7}$$

where σ_{ws} is the vertical turbulent velocity at the bottom of the canyon, U_s is the wind speed at the bottom of the canyon, and h_0 is the initial vertical plume spread. By modeling the road as an area source and integrating the ground-level concentration across the source, the concentration next to the edge of the road is given by Berkowicz et al. (1997):

$$C_{direct} = \sqrt{\frac{2}{\pi}} \frac{q}{W \sigma_{ws}} \ln\left(1 + \frac{W \sigma_{ws}}{h_0 U_s}\right) \tag{5.8}$$

where q is the emission rate per unit length of road and W is the road width. The initial vertical plume spread, h_0, is due to the mixing produced by motion of the vehicles, and has magnitude proportional to the vehicle height.

The recirculating contribution is determined by considering the canyon as a box model. Emissions enter the box at the bottom and are transported out of the box at the top by the vertical turbulent velocity at the top of the box. When the building height, H, is larger than the street width, $H \geq W$, the concentration in the box is:

$$C_{recirc} = \frac{q}{W \sigma_{wr}} \tag{5.9}$$

where σ_{wr} is the standard deviation of vertical velocity fluctuations at the top of the canyon.

OSPM determines the wind speed at the bottom of the canyon from that at the rooftop by assuming a logarithmic velocity profile within the canyon:

$$U_s = U_t \frac{\ln(h_0/z_0)}{\ln(H/z_0)} (1 - 0.2p \sin(\Phi)) \tag{5.10}$$

where U_t is the wind speed at the top of the canyon, z_0 is the surface roughness length, Φ is the angle of the rooftop wind from the direction parallel to the street, and $p = H_{upwind}/H$, where H_{upwind} is the building height on the upwind side of the road. The surface roughness length is

0.1 m. At the ground, the vertical turbulent velocity is the combination of the mechanically generated turbulence and the traffic produced turbulence:

$$\sigma_{ws} = ((0.1U_s)^2 + \sigma_{w0}^2)^{1/2} \tag{5.11}$$

where σ_{w0} is the vertical turbulent velocity due to traffic. The vertical turbulent velocity at the roof is calculated as:

$$\sigma_{wr} = ((0.1U_t)^2 + 0.4\sigma_{w0}^2)^{1/2} \tag{5.12}$$

The traffic produced turbulence is:

$$\sigma_{w0} = b\left(\frac{N_{veh}VS^2}{W}\right)^{1/2} \tag{5.13}$$

where N_{veh} is the traffic flow rate, V is the average vehicle speed, S^2 is the surface area of one vehicle, and $b = 0.3$ is a constant.

OSPM includes many special cases and formulations to ensure that the concentrations produced by the model are reasonable. The description of OSPM that we have given here only includes the components of the model essential to describe the street canyon formulation for winds blowing perpendicular to the street.

Vertical Dispersion Model

OSPM is designed to estimate concentrations within street canyons and thus invokes the concept of a street lined with unbroken walls of buildings with uniform heights. Within real-world cities, the building heights and shapes are often extremely variable, buildings are placed at varying distance from the road, and gaps often exist between buildings. It is not clear that street canyon models are useful for estimating dispersion of traffic emissions within these types of streets, which are typical of those found in US cities. Thus, there is a need for a model that accounts for the effects of varying building heights on dispersion. But, in doing so, as we will see later, the model relinquishes the spatial resolution of the concentration field that OSPM is designed for.

The model that we describe next is designed to estimate near surface concentrations of pollutants emitted from vehicles traveling on urban streets

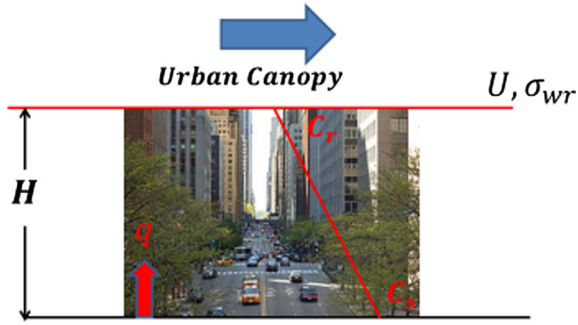

Figure 5.4 Schematic illustrating the balance between emissions and vertical transport.

surrounded by buildings. We refer to it as the vertical dispersion model (VDM) to emphasize the dominant influence of vertical turbulent transport in its formulation. The model assumes that the near surface concentrations over the length and breadth of a typical city block is governed by the balance between emissions at the surface and vertical transport out of the urban canopy, as shown in Fig. 5.4.

Then, we can write

$$q \sim K_z W \frac{(C_s - C_r)}{H} \tag{5.14}$$

where K_z is the vertical eddy diffusivity, H and W are the building height and street width, C_s is the horizontally averaged concentration in the street canyon at the ground, C_r is the rooftop (at H) concentration, and q is the emission rate per unit length of the street.

The eddy diffusivity is taken as the product of a mixing length, l, and the standard deviation of vertical velocity fluctuations averaged over the height of the buildings, σ_w:

$$K_z = l\sigma_w \tag{5.15}$$

If we assume that the size of the large turbulent eddies dominating vertical mixing is limited by the smaller of the street width and building height, then the mixing length is proportional to the smaller of H and W:

$$l \sim \left(h_0 + \frac{HW}{H + W} \right) \tag{5.16}$$

where h_0 is the mixing length associated with the initial vertical mixing caused by the motion of the vehicles. Eqs. (5.14) through (5.16) can be combined to yield an expression for the surface concentration:

$$C_s - C_r = \frac{q}{\beta\sigma_w W}\left(\frac{1+a_r}{1+(1+a_r)\left(h_0/H\right)}\right) \tag{5.17}$$

where $a_r = \left(H/W\right)$ is the aspect ratio and β is an empirical constant, which is obtained by fitting model estimates to observations.

If measurements of the rooftop concentration are not available, C_r can be estimated by assuming that local emissions are matched by vertical transport at roof level:

$$q = \gamma C_r W \sigma_{wr} \tag{5.18}$$

where $\sigma_{wr}$is the standard deviation of vertical velocity fluctuations at roof level, and γ is an empirical constant used to calibrate the model.

Substituting Eq. (5.18) into (5.17) yields:

$$C_s = \frac{q}{\gamma\sigma_{wr} w}\left(1 + \frac{\gamma\sigma_{wr}}{\beta\sigma_w}\frac{1+a_r}{1+(1+a_r)\left(\frac{h_0}{H}\right)}\right) \tag{5.19}$$

Eqs. (5.17) and (5.19) are referred to as the VDM. Eq. (5.17) can be used if σ_w and C_r can be estimated from measurements. In practice, this information is usually not available. Thus, it is often necessary to estimate the average σ_w from the rooftop σ_{wr}, which can be estimated using the models described in Chapter 6.

We can relate σ_w to σ_{wr} by assuming that turbulent kinetic energy produced at roof level, per unit length of street, $u_{*r}^2 U_r W$, is dissipated over the volume of the street at the rate $(\sigma_w^3/l)WH$:

$$u_{*r}^2 U_r W \sim \sigma_{wr}^3 W \sim \frac{\sigma_w^3}{l} WH \tag{5.20}$$

where l is the length scale of the large turbulent eddies within the canyon, and u_{*r}^2 and U_r are the shear stress and the mean wind speed at roof level, and both u_{*r} and U_r are correlated with σ_{wr}. If l is similar to the form given by Eq. (5.16), we can write the semiempirical expression:

$$\sigma_{wr} = \sigma_w(1+\eta a_r)^{1/3} \tag{5.21}$$

where $\eta = 0.4$ provides the best fit with the data as shown in a later section. The ratio of rooftop and average σ_w is nearly constant because the 1/3 power in Eq. (5.21) results in low sensitivity to the aspect ratio.

The application of VDM requires a value of the aspect ratio, a_r, that best describes the morphology of the nonuniform buildings lining a street. This was determined empirically by evaluating VDM with data collected in a field experiment conducted in Los Angeles, the details of which are discussed in the next section. We found that the following definition of the effective height, H, of the buildings provided the best results:

$$H = \frac{1}{L}\sum_i H_i B_i \tag{5.22}$$

where L is the street length, H_i and B_i are the height and width (along the street) of building i, and the sum is taken over all the buildings on one side of the street. Eq. (5.22) can be interpreted as the area-weighted building height: the sum of the frontal area of the buildings divided by the street length. Then, the equivalent building height used in Eq. (5.19) is the average over both sides of the street.

We assume that the modeled concentration represents an average over the street canyon within one city block. For the effective building height to be consistent with the model, it is calculated from the geometry of all the buildings bordering the street canyon within one city block. The use of the block length for defining the scale for horizontal inhomogeneity is somewhat arbitrary, but the assumption of horizontal homogeneity within one city block has been used in models such as SIRANE (Soulhac et al., 2011), and comparisons with observations indicate that this is a useful assumption.

COMPARISON OF MODEL WITH OBSERVATIONS

This section describes the performance of the VDM in estimating concentrations of traffic emissions. Model performance is evaluated using near-road measurements of concentrations of ultrafine particle number (UFP) and carbon monoxide (CO) made in field studies conducted in Riverside and Los Angeles, CA.

Throughout this section, we use the geometric mean, m_g, and standard deviation, s_g, of the residuals between log-transformed model predictions and observations as well as the correlation coefficient, r^2, and the fraction of data within a factor of two of model estimates, *fact*2, to evaluate model performance. The geometric mean and standard deviation are computed as $\ln(m_g) = \frac{1}{n}\sum_i r_i$, and $\ln(s_g) = \sqrt{\frac{\sum_i [r_i - \ln(m_g)]^2}{n-1}}$, where $r_i = \ln(C_{oi}) - \ln(C_{mi})$, subscripts *oi* and *mi* refer to observed and model estimated concentrations, and n is the number of data points. An m_g equal to one indicates zero model bias. The interval that contains 95% of the ratios of observed to predicted concentrations is approximately given by $[m_g s_g^{-2}, m_g s_g^2]$.

Description of the Los Angeles Field Measurements

We use observed near-road concentrations of UFP to evaluate the dispersion models. This is done for three reasons. First, UFP is a product of combustion that provides a strong signal of local traffic emissions. Second, it is linked with negative health effects (Knibbs et al., 2011). Finally, the condensation particle counters that measure UFP have a response time on the order of 10 s, fast enough to capture the impact of individual vehicles or groups of vehicles on the concentration. The time signature of these concentration events can be processed to yield the contribution of local vehicle traffic on the total concentration observed by the monitor. Thus, the UFP signal allows us to separate local traffic sources from background sources, which is extremely useful for evaluation of street-scale dispersion models since these models use horizontal averaging scales on the order of the size of the street and thus treat emissions on adjacent streets as part of the background.

The primary condition for locating the concentration monitors is based on the need to resolve the effect of the built environment on near road concentrations. Field measurements pose significant challenges to isolating the effect of one variable on the concentration because variability in uncontrolled factors such as traffic emission rate can overwhelm the signal due to the presence of buildings. The local vehicle emission rate must be known to evaluate the dispersion models, but emissions can be difficult to determine in practice. Individual vehicle emission rates can vary significantly, and during congested driving conditions, characteristic of urban environments, the local traffic within a street is often

Table 5.1 Locations at Which Field Measurements of UFP Were Made. The Observations Are Used to Evaluate the VDM and OSPM

Location	Dates	Building Morphology
Downtown Los Angeles	9/20/13, 5/7/14, 5/9/14	Urban core with significant building height variability. Many buildings approximately 50 m tall
Wilshire Blvd	5/30/14	Variable building heights up to 50 m tall. Average building height is less than that in downtown Los Angeles
Temple City	1/15/14, 1/16/14, 1/17/14	Suburban area with many single-story buildings. Nearly uniform building height of 6 m
Riverside	7/1/15–7/30/15	Urban area with buildings about 20 m tall

accelerating or idling, increasing uncertainty of the emission rates (Smit et al., 2008). Emission models of gaseous pollutants and particle mass are usually accurate to about a factor of two or three (Smit et al., 2010). UFP number, which we use as the primary measured pollutant in the field study, has emission factors that vary by about an order of magnitude Kumar et al. (2011). Because of the uncertainty in the emission estimates, when possible the experiments were designed so that UFP concentration measurements were made at two sections on the same street: one section with tall buildings adjacent to the street and another where there are no buildings or very short buildings adjacent. This design ensures that local vehicle emissions are similar at the two locations, allowing us to directly compare concentrations at the open and building sections to isolate the building effect.

The data used in this evaluation was collected during two measurement campaigns. The first campaign was conducted in several cities in Los Angeles County, CA, USA, between September 2013 and July 2014. The second campaign was conducted in Riverside, CA, USA, in September and August, 2015. Table 5.1 gives an overview of the building morphology of the various field locations in this campaign.

Here, we use the data from the Los Angeles study to evaluate the performance of the VDM and OSPM. We use data from the Riverside field study to further evaluate the VDM, including observed concentrations of traffic-emitted carbon monoxide. The evaluation using the data from the Riverside study is described in the next section.

Table 5.2 Summary of Area-Weighted Building Height, Street Width, and Aspect Ratio of All Sites

Site	Area-Weighted Building Height [m]	Street Width [m]	Aspect Ratio
8th St Building	43.25	20.0	2.16
8th St Mid	34.5	20.0	1.73
Broadway	35.90	26.0	1.38
7th St	45.80	25.0	1.83
Temple City	6.00	30.0	0.20
Wilshire Blvd Building	36.0	30.0	1.20
Wilshire Blvd Open	8.25	30.0	0.28

TSI 3022 condensation particle counters were used to record UFP number concentrations at a sampling rate of 1 Hz. Samples are drawn through a copper and Tygon tube with the tube sampling inlet set at 1 m above ground level. The instruments measure the concentration of particles with diameters greater than 10 nm (50% detection efficiency is 10 nm). The inlet flow rate is 1.5 L min^{-1}.

One of the measurement locations in downtown Los Angeles was near the 8th St and Hill St intersection. The site was chosen because 8th St had a section where there were no buildings next to the road, the "open" site, and a section where there were tall buildings directly next to the road, the "built" site. We obtained building height and outline information for Los Angeles County in a GIS database format which we then used to calculate the built environment parameters shown in Table 5.2. The data for this study was obtained from the Los Angeles County GIS data portal (Los Angeles County, 2008). Information about the building geometry is an essential component for modeling dispersion of traffic emissions that is often not readily available. It is rare to have access to such information on the built environment as LA county freely provides.

Evaluation of the VDM with Data Collected in Los Angeles and Riverside

Fig. 5.5 shows the evaluation of the surface concentration predicted by Eq. (5.19) with the 30-min averaged local contribution of UFP in the Los Angeles field study, normalized by the traffic emission rate based on the local vehicle traffic counts. The local contribution is a measure of local traffic impacts, and we use the average of the values measured on

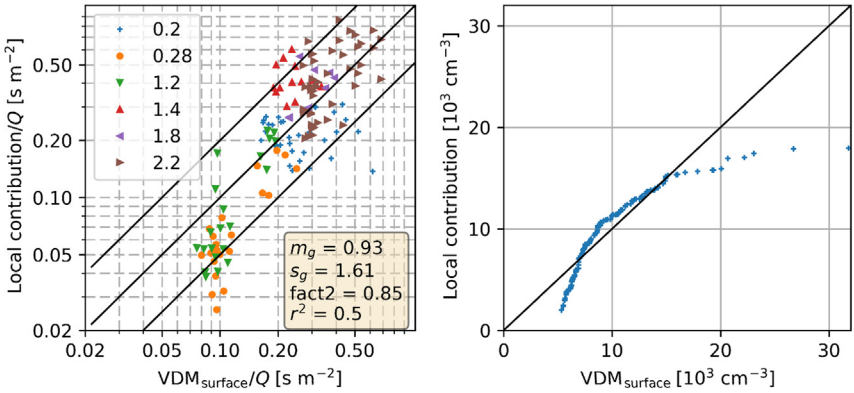

Figure 5.5 Comparison of VDM with 30 min averaged local contribution of UFP. Left: scatter plot of the data. The local contribution is the average of both sides of the street and is normalized by the daily average emission rate, assuming an emission factor of $10^{14} veh^{-1} km^{-1}$. Right: quantile–quantile plot. The building height of the 8th St open section has been set equal to that of the 8th St building section. $VDM_{surface}$ is C_s from Eq. (5.19).

both sides of the street for the model evaluation. We describe the method to compute the local contribution next.

To remove the impact of background sources, we determine the contribution of local emissions to the total concentration observed at the surface monitors, and use only this "local contribution." The UFP concentration time series contains information about the local vehicle emissions in the form of large amplitude short-lived spikes superimposed on the slowly varying baseline. This occurs because the UFP emission factor varies by several orders of magnitude, and so local emission events from high-emitting vehicles produce large concentration spikes that can be separated from the total concentration. We filter the signal to separate the slowly varying component from the spikes, which contain information about local emissions. A moving average filter with a window size larger than the time scale of the spikes does not adequately separate the two components because the concentration distribution is highly skewed, making the average an inadequate measure of the baseline concentration. Instead of the moving average, we use a windowed percentile to separate the components. We define the baseline as the concentration that is below a chosen percentile of the concentration distribution. Then, within each time window of a chosen length, each data point is classified as either baseline or spike if the concentration is below or above the

percentile cutoff of the window. The baseline is then constructed by linearly interpolating between the points that are classified as baseline, and the spikes are separated by subtracting the baseline from the total. This type of analysis is common for analyzing UFP time series, especially in analysis of mobile monitoring data (Bukowiecki et al., 2002). Details of the method that we have developed are described in Schulte et al. (2015).

The model was applied to the data using the best fit parameters $h_0 = 2m$ and $\beta = 1$. The values of the parameters that characterize the buildings, the area-weighted building height, and street width are listed in Table 5.2. We have assumed the emission factor of UFP equals $10^{14} veh^{-1} km^{-1}$, which is the magnitude of UFP emission factors reported in literature (Kumar et al., 2011). The value of the final parameter, γ, was determined by matching the observed and modeled concentrations from the Los Angeles data. The resulting value is $\gamma = 1.0$.

The left panel of Fig. 5.5 shows the scatter plot of the data and the right panel shows a quantile−quantile plot. The figure indicates that the model provides a good description of the measured local contributions of UFP. There is little model bias and most of the observations are within a factor of two of the model estimates. The quantile−quantile plot indicates that the model overestimates the lowest concentrations and the scatter plot of the concentrations normalized by emissions shows that this is due to underestimation of the dispersion. However, most of the data is described well by the model. This implies that local contributions are primarily governed by the ratio of area-weighted building height to street width and the vertical average of the standard deviation of the vertical velocity fluctuations. The low model bias indicates that traffic emissions are consistent with an emission factor of $1.0 \times 10^{14} veh^{-1} km^{-1}$. This value is within the range reported by Ketzel et al. (2003).

Evaluation of the OSPM recirculating contribution model, which uses the mean rooftop wind speed as the primary meteorological variable governing near road concentrations, showed little correlation between model estimates and observations at the field sites in the Los Angeles study. This supports the conclusion that vertical turbulent transport rather than advection by the mean wind dominates dispersion in cities with significant building height variability. This conclusion is supported by observations analyzed in Hanna et al. (2014), which show that data from field studies conducted in Manhattan, NY, indicate rapid vertical mixing in the presence of buildings.

We show that modeling the air quality impact of vehicular emissions reduces to estimating the effective aspect ratio of the street, and the roof

level σ_w. The effective aspect ratio plays the major role in magnifying concentrations relative to those that would have been measured in the absence of buildings.

The building morphology where measurements were conducted in Los Angeles was mainly of two types: urban core areas with many tall ($\sim$50 m) buildings, and suburban with primarily single story buildings. So VDM was evaluated with measurements conducted in a street with an intermediate aspect ratio of 0.4 in Riverside, CA, over a period of about a month. We used observed near-road concentrations of carbon monoxide to improve the calibration of the empirical constants in the VDM and to estimate confidence limits for their values.

As in the previous study conducted in Los Angeles, concentration measurements were made next to a busy road at two locations, one with tall buildings next to the road and one several blocks away with only short buildings next to the road. A site next to Market St in Riverside, CA, was chosen to meet the requirements of the study. Fig. 5.6 shows an overview of the site. The "building" section has an area-weighted building height of 14.37 m and a street width of 33 m, resulting in an aspect ratio of 0.44. The "open" section has area-weighted building height of 2.14 m and street width of 30 m. The traffic on Market St was about 26,000 vehicles per day.

Fig. 5.6 shows the locations of the instruments that were used in the study. Campbell scientific CSAT3 sonic anemometers were used to measure the three components of wind speed and temperature at 10 Hz at both the building and open sites and on the roof of city hall, approximately 100 m from the building site. The resulting turbulence data was processed to yield time average wind speeds, wind direction, turbulent velocities, and heat and momentum fluxes. The micrometeorological measurements were made continuously between July 30 and September 9, 2015.

Concentrations of UFP were measured using TSI 3022 condensation particle counters between about 7 am and 7 pm on 15 days in August and September, 2015, resulting in a total of about 150 h of particle concentration data. A total of five particle counters were used: one on each side of Market St at both the building and open sites and one on the city hall roof. The instruments provided 1-second average concentrations. The UFP concentration data was processed to yield the contribution of local vehicle traffic using the method described for the evaluation of the Los Angeles data.

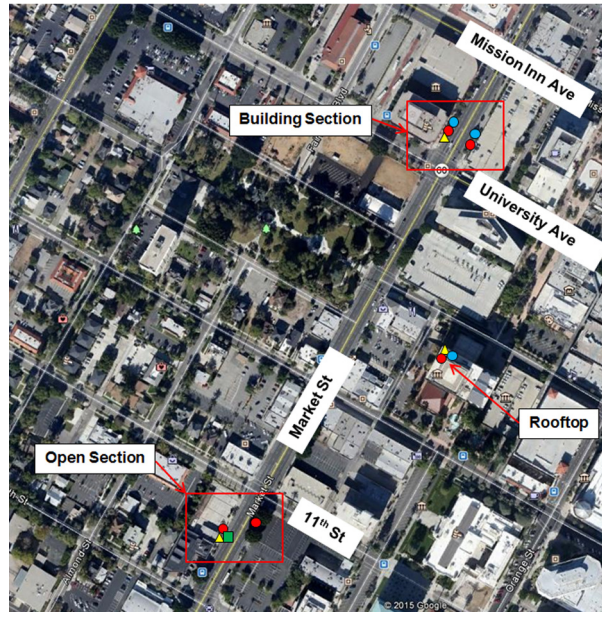

Figure 5.6 Location of instruments in May 2015 Riverside, CA, field study. ●—Condensation Particle Counter (CPC).●—AQMesh. △—Sonic Anemometer. ■—Camera. Map Data: Google.

Measurements of carbon monoxide (CO), nitrogen oxides (NO and NO_2), ozone (O_3), and sulfur dioxide (SO_2) were made using AQMesh five gas pollutant monitor "pods" between August 18 and September 9, 2015. The pods are ideally suited for long term measurements of concentrations of vehicle emissions. They use much less power than the condensation particle counters, the integrated battery holds enough charge to function for the entire study, enabling continuous concentration measurements. Three pods were used: one on each side of Market St at the "building" section, and one on the rooftop. Averaging time for the AQMesh monitors was 1 min, and data was later aggregated into 2 h averages for analysis. Only the carbon monoxide data was analyzed for the evaluations in this chapter.

Sonic anemometers and AQMesh pods were mounted at a height of 4 m above ground level (AGL). Condensation particle counters mounted to light poles have inlets at a height of 1 m AGL. The rooftop sonic anemometer and AQMesh pod were attached to a tripod 3 and 2 m above the 25 m-tall roof of city hall, respectively. The rooftop condensation particle counter inlet is 0.5 m above the rooftop.

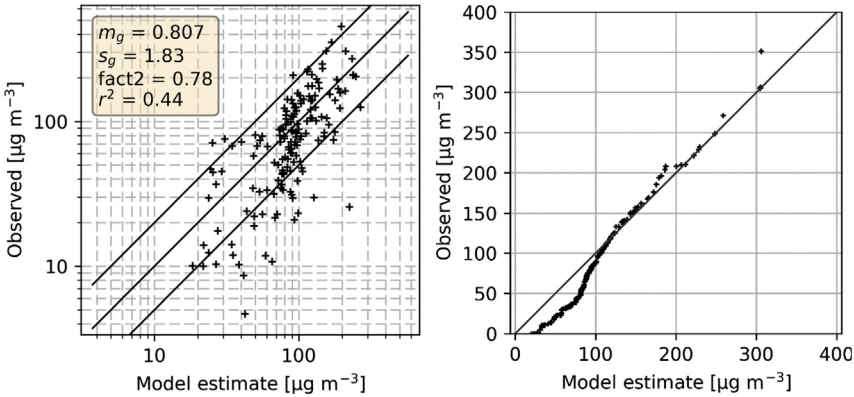

Figure 5.7 Comparison of VDM with vertical difference of 2-h average carbon monoxide concentrations in Riverside, CA. Left: Scatter plot of the data. Observations are normalized by the emission rate assuming an emission factor of 3.75$g\ km^{-1}$ for nontrucks and 2.5$g\ km^{-1}$ for trucks. Right: Quantile–quantile plot.

Fig. 5.7 shows the comparison of the observed vertical difference of carbon monoxide concentrations with VDM predictions. Model estimates are determined using emission factors of 3.75$g\ km^{-1}$ for nontrucks and 2.5$g\ km^{-1}$ for trucks.

There is significant scatter between the observations and model estimates, indicated by the low correlation coefficient. However, 78% of the data are within a factor of two of model estimates. Most of the discrepancy between observations and model estimates is due to cases where the observed vertical difference is small compared with model estimates. This usually occurs during night and early morning between about 1:00 am and 7:00 am, when the traffic flow rate and hence the emission rate is very small. We do not have a good estimate of the actual traffic flow rate during this time period. In particular, the comparison is somewhat sensitive to the assumption of when the morning rush hour traffic begins, since this determines the time of the morning spike in concentration. The right panel of Fig. 5.7 shows that the VDM tends to overestimate the lowest concentrations but otherwise the distribution of concentrations predicted by VDM describes the data remarkably well.

There is little model bias since we derived the emission factor from the comparison of model with observations. The values of m_g and s_g indicate that 95% of the observations are within a factor of 0.24–2.7 of the model estimates. These results show that the VDM adequately predicts near road

concentrations within an urban area. To apply the model, we need to determine the value of the meteorological input variables: σ_w at the urban rooftop and surface. Since measurements of σ_w are not routinely made in urban areas, these variables must be determined from routine meteorological measurements, which are usually only made in rural areas such as airports. Chapter 6 describes the evaluation of a model that relates measured micrometeorology at a rural area to that at the urban rooftop and surface.

SUMMARY

The evaluation of the VDM supports the applicability of the model for estimating near-road concentrations within urban areas. The results show that the standard deviation of vertical velocity fluctuations, σ_w, in the urban canopy governs near-surface concentrations, especially during low wind speed conditions typical of urban areas. The mean wind speed likely plays a small role in dispersion in urban areas because the turbulent intensities are large, resulting in significant horizontal meandering of the pollutant plume. Measurements of mean winds and turbulence in Manhattan and Oklahoma city (Hanna, 2009; Hanna et al., 2007) support the conclusion that strong vertical turbulent mixing governs dispersion in urban areas. Near surface winds in these studies were only about 1/3 of the rooftop value, and wind directions varied significantly (Hanna et al., 2007). This results in more horizontal meandering of pollutant plumes, creating conditions where vertical transport governs the near-road concentrations.

For the VDM to be consistent with the data collected in the Los Angeles study as well as the Riverside measurements, it was necessary to assume that the emission factors of NO_x, CO, and UFP could vary by about a factor of two of the EMFAC2011 estimates. This assumption is supported by studies showing errors in emission models of up to a factor of three and two for CO and NO_x, respectively (Smit et al., 2010). Emission factors depend on the composition of the vehicle fleet and the type of driving conditions. Hence, traffic flow conditions observed in the Riverside study may result in emission factors that are different from those predicted by average speed models such as EMFAC, and it may be necessary to estimate emissions by explicitly

including the level of traffic congestion at the field site in the emission model (Smit et al., 2008). However, it may be difficult to obtain more accurate emission estimates even with more comprehensive models that include measures of congestion because it will be more difficult to obtain accurate estimates of the input data for these models. Considering the uncertainty in the emission rates, the value of the model calibration constant β is likely within about a factor of two of the value $\beta = 1$ chosen in this study.

We have shown that estimating the impact of buildings on dispersion of traffic emissions in the near-road environment reduces to estimating the ratio of the area-weighted building height to street width and the vertical average of the standard deviation of vertical velocity fluctuations. Throughout this chapter, we have used measurements to determine the values of the micrometeorological model inputs. However, only the mean wind is routinely measured, and these measurements are primarily made in rural areas. For practical applications where the turbulence data in the urban area is unknown, we must determine the values of the micrometeorological input variables required for the VDM from these routine measurements. Chapter 6 describes methods to estimate the urban micrometeorology based on the routine measurements at an upwind rural location.

The evaluation and application of VDM has focused on a single street in a city block. How do we apply the model to estimate near surface concentrations in an urban area with a large number of roads? One approach is to use a model such as AERMOD to estimate concentrations at the effective top of the urban canopy assuming that the roads are the same level as the canopy top. The meteorological inputs would account for the roughness of the urban area averaged over the scale of the urban built-up area. The IBL model, described in Chapter 6, can be used to estimate these inputs. The resulting concentrations correspond to the rooftop values in Eq. (5.17), which can be then used to estimate the concentration at street level using

$$C_s = C_{AERMOD} + \frac{q}{\beta \sigma_w W}\left(\frac{1 + a_r}{1 + (1 + a_r)\left(h_0/H\right)}\right), \tag{5.23}$$

where the parameters in the second term on the right-hand side of the equation correspond to the road of interest. More details are described in Chapter 6.

REFERENCES

Aarhus University Department of Environmental Science, 2018. Operational Street Pollution Model-OSPM. http://www.au.dk/ospm/.

Allwine, K.J., Shinn, J.H., Streit, G.E., Clawson, K.L., Brown, M., 2002. Overview of urban 2000: a multiscale field study of dispersion through an urban environment. Bull. Am. Meteorol. Soc. 83, 521–536.

Barlow, J.F., Belcher, S.E., 2002. A wind tunnel model for quantifying fluxes in the urban boundary layer. Bound.-Layer Meteorol 104, 131–150.

Bentham, T., Britter, R., 2003. Spatially averaged flow within obstacle arrays. Atmos. Environ. 37, 2037–2043. Available from: https://doi.org/10.1016/S1352-2310(03)00123-7.

Berkowicz, R., Hertel, O., Larsen, S.E., Sørensen, N.N., Nielsen, M., 1997. Modelling traffic pollution in streets. Natl. Environ. Res. Inst. Rosk. Den 10129, 20.

Britter, R.E., Hanna, S.R., 2003. Flow and dispersion in urban areas. Annu. Rev. Fluid Mech. 35, 469–496. Available from: https://doi.org/10.1146/annurev.fluid.35.101101.161147.

Bukowiecki, N., Dommen, J., Prevot, A.S.H., Richter, R., Weingartner, E., Baltensperger, U., 2002. A mobile pollutant measurement laboratory—measuring gas phase and aerosol ambient concentrations with high spatial and temporal resolution. Atmos. Environ. 36, 5569–5579.

California Air Resources Board, 2017. Mobile Source Emission Inventory. URL https://www.arb.ca.gov/msei/msei.htm (accessed 1.1.17).

Cheng, H., Castro, I.P., 2002. Near wall flow over urban-like roughness. Bound.-Layer Meteorol 104, 229–259.

Cimorelli, A.J., Perry, S.G., Venkatram, A., Weil, J.C., Paine, R.J., Wilson, R.B., Lee, R.F., Peters, W.D., Brode, R.W., 2005. AERMOD: a dispersion model for industrial source applications. Part I: general model formulation and boundary layer characterization. J. Appl. Meteorol 44 (5), 682–693.

Dabberdt, W.F., Ludwig, F.L., Johnson, Jr., W.B., 1973. Validation and applications of an urban diffusion model for vehicular pollutants. Atmos. Environ. 7, 603–618.

DePaul, F.T., Sheih, C.M., 1986. Measurements of wind velocities in a street canyon. Atmos. Environ. 20, 455–459. Available from: https://doi.org/10.1016/0004-6981(86)90085-5.

Fisher, B., Kukkonen, J., Piringer, M., Rotach, M.W., Schatzmann, M., 2006. Meteorology applied to urban air pollution problems: concepts from COST 715. Atmospheric. Chem. Phys. 6, 555–564. Available from: https://doi.org/10.5194/acp-6-555-2006.

Hanna, S., 2009. A simple urban dispersion model tested with tracer data from Oklahoma City and Manhattan. Atmos. Environ. 43, 778–786.

Hanna, S., White, J., Zhou, Y., 2007. Observed winds, turbulence, and dispersion in built-up downtown areas of Oklahoma City and Manhattan. Bound.-Layer Meteorol. 125, 441–468. Available from: https://doi.org/10.1007/s10546-007-9197-2.

Hanna, S., Chang, J.C., Flaherty, J., 2014. Observed Ratios of Rooftop to Surface Concentrations in Built-Up City Centers. Atlanta, Georgia. Available at www.ametsoc.org.

Johnson, W.B., Ludwig, F.L., Dabberdt, W.F., Allen, R.J., 1973. An urban diffusion simulation model for carbon monoxide. J. Air Pollut. Control Assoc. 23, 490–498. Available from: https://doi.org/10.1080/00022470.1973.10469794.

Ketzel, M., Wåhlin, P., Berkowicz, R., Palmgren, F., 2003. Particle and trace gas emission factors under urban driving conditions in Copenhagen based on street and roof-level observations. Atmos. Environ. 37, 2735–2749. Available from: https://doi.org/10.1016/S1352-2310(03)00245-0.

Knibbs, L.D., Cole-Hunter, T., Morawska, L., 2011. A review of commuter exposure to ultrafine particles and its health effects. Atmos. Environ. 45, 2611–2622. Available from: https://doi.org/10.1016/j.atmosenv.2011.02.065.

Kumar, P., Ketzel, M., Vardoulakis, S., Pirjola, L., Britter, R., 2011. Dynamics and dispersion modelling of nanoparticles from road traffic in the urban atmospheric environment—a review. J. Aerosol Sci. 42, 580–603. Available from: https://doi.org/10.1016/j.jaerosci.2011.06.001.

Los Angeles County, 2008. Countywide Building Outlines.

Louka, P., Belcher, S.E., Harrison, R.G., 2000. Coupling between air flow in streets and the well-developed boundary layer aloft. Atmos. Environ. 34, 2613–2621.

MacDonald, R.W., 2000. Modelling the mean velocity profile in the urban canopy layer. Bound.-Layer Meteorol. 97, 25–45.

Meroney, R.N., Pavageau, M., Rafailidis, S., Schatzmann, M., 1996. Study of line source characteristics for 2-D physical modelling of pollutant dispersion in street canyons. J. Wind Eng. Ind. Aerodyn. 62, 37–56.

Nicholson, S.E., 1975. A pollution model for street-level air. Atmos. Environ. 9, 19–31.

Oke, T.R., 1988. Street design and urban canopy layer climate. Energy Build. 11, 103–113. Available from: https://doi.org/10.1016/0378-7788(88)90026-6.

Rotach, M.W., Vogt, R., Bernhofer, C., Batchvarova, E., Christen, A., Clappier, A., et al., 2005. BUBBLE – an urban boundary layer meteorology project. Theor. Appl. Climatol. 81, 231–261. Available from: https://doi.org/10.1007/s00704-004-0117-9.

Smit, R., Brown, A.L., Chan, Y.C., 2008. Do air pollution emissions and fuel consumption models for roadways include the effects of congestion in the roadway traffic flow? Environ. Model. Softw. 23, 1262–1270. Available from: https://doi.org/10.1016/j.envsoft.2008.03.001.

Smit, R., Ntziachristos, L., Boulter, P., 2010. Validation of road vehicle and traffic emission models – a review and meta-analysis. Atmos. Environ. 44, 2943–2953. Available from: https://doi.org/10.1016/j.atmosenv.2010.05.022.

Soulhac, L., Salizzoni, P., Cierco, F.-X., Perkins, R., 2011. The model SIRANE for atmospheric urban pollutant dispersion; part I, presentation of the model. Atmos. Environ. 45, 7379–7395. Available from: https://doi.org/10.1016/j.atmosenv.2011.07.008.

Vardoulakis, S., Fisher, B.E., Pericleous, K., Gonzalez-Flesca, N., 2003. Modelling air quality in street canyons: a review. Atmos. Environ. 37, 155–182. Available from: https://doi.org/10.1016/S1352-2310(02)00857-9.

Yamartino, R.J., Wiegand, G., 1986. Development and evaluation of simple models for the flow, turbulence and pollutant concentration fields within an urban street canyon. Atmos. Environ. 20, 2137–2156. Available from: https://doi.org/10.1016/0004-6981(86)90307-0.

FURTHER READING

Berkowicz, R., 2000. A simple model for urban background pollution. Environ. Monit. Assess. 65, 259–267.

Caton, F., Britter, R.E., Dalziel, S., 2003. Dispersion mechanisms in a street canyon. Atmos. Environ. 37, 693–702. Available from: https://doi.org/10.1016/S1352-2310(02)00830-0.

DePaul, F.T., Sheih, C.M., 1985. A tracer study of dispersion in an urban street canyon. Atmos. Environ. 19, 555–559.

Hanna, S.R., 1989. Confidence limits for air quality model evaluations, as estimated by bootstrap and jackknife resampling methods. Atmospheric Environ 1967 (23), 1385–1398.

Hoydysh, W.G., Dabberdt, W.F., 1988. Kinematics and dispersion characteristics of flows in asymmetric street canyons. Atmos. Environ. 22, 2677–2689.

Macdonald, R.W., Griffiths, R.F., Hall, D.J., 1998. An improved method for the estimation of surface roughness of obstacle arrays. Atmos. Environ. 32, 1857–1864. Available from: https://doi.org/10.1016/S1352-2310(97)00403-2.

Nakamura, Y., Oke, T.R., 1988. Wind, temperature and stability conditions in an east-west oriented urban canyon. Atmos. Environ. 22, 2691–2700. Available from: https://doi.org/10.1016/0004-6981(88)90437-4.

Stockie, J.M., 2011. The mathematics of atmospheric dispersion modeling. SIAM Rev. 53, 349–372. Available from: https://doi.org/10.1137/10080991X.

Venkatram, A., Isakov, V., Thoma, E., Baldauf, R., 2007. Analysis of air quality data near roadways using a dispersion model. Atmos. Environ. 41, 9481–9497. Available from: https://doi.org/10.1016/j.atmosenv.2007.08.045.

CHAPTER SIX

Modeling Dispersion at City Scale

Contents

Introduction 139
Dispersion Models for Near-Road Air Quality 139
Integrating Dispersion Models into a Modeling System 141
References 145

INTRODUCTION

This chapter has three objectives: (1) summarize the primary features of the dispersion models described in previous chapters, (2) describe how the models described earlier can be integrated into a system for estimating the impact of transport-related emissions on air quality next to streets in an urban area with buildings, and (3) describe the construction of micrometeorological inputs for dispersion models applied in urban areas.

Dispersion Models for Near-Road Air Quality

We can use the simple models described in Chapter 4, The Impact of Highways on Urban Air Quality, to illustrate the effects of roadside barriers on concentrations. As a first estimate, we can use Eq. 4.26 to compute the impact of a downwind barrier with a height of 5 m. The ratio of the concentrations with the barrier, C_b, to that without the barrier, C_{nb}, is

$$\frac{C_b(L)}{C_{nb}(L)} = \frac{\ln\left(1 + \frac{W}{\left(\sqrt{2/\pi}HU/\sigma_w\right) + L}\right)}{\ln\left(1 + \frac{W}{\left(h_0U/\sigma_w\right) + L}\right)} \tag{6.1}$$

where H is the barrier height and we have accounted for the effect of the barrier on concentrations by setting the initial vertical plume spread as

Urban Transportation and Air Pollution.
DOI: https://doi.org/10.1016/B978-0-12-811506-0.00006-3

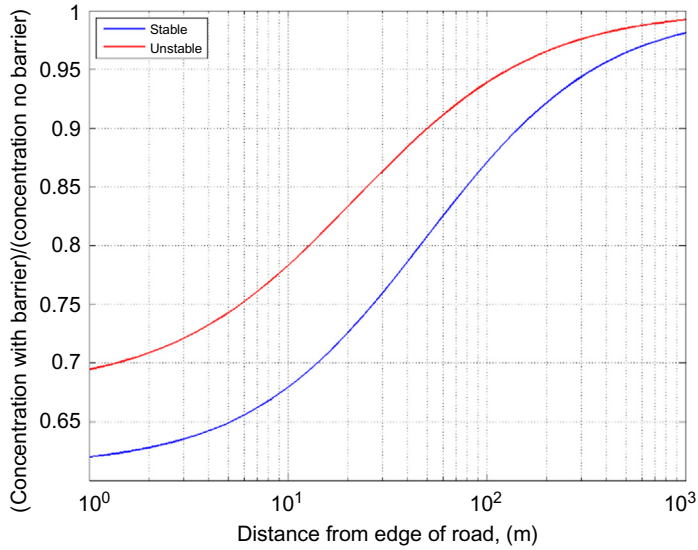

Figure 6.1 Impact of a 5 m barrier on near-road concentrations for $\frac{U}{\sigma_w} = 4$(**unstable**) and $\frac{U}{\sigma_w} = 10$(**stable**).

$h_0 = \sqrt{(2/\pi)H}$. This ratio is likely to be a lower limit because the presence of a barrier will increase the turbulence level σ_w. Fig. 6.1 plots this ratio as a function of distance from the edge of a road for two different values of U/σ_w corresponding to stable and unstable surface boundary layers. We see that in this case, the concentration reduction relative to the concentrations in the absence of the barrier varies from about 30% to 40% next to the road to about 5%–15% at 100 m. The impact of the barrier increases with the stability of the surface layer.

The main point here is that a simple model can provide first cut estimates of concentrations next to roads. The effects of barriers and depressions can be included in this model through initial mixing heights roughly equal to the height of the barrier or the depth of the depression. We can also accommodate the formulations of vertical spread described in Chapter 3, Fundamentals of Micrometeorology and Dispersion, in this model by recasting Eq. (6.1) as

$$C(L) = \sqrt{\frac{2}{\pi}}\frac{Q}{W\sigma_w}\ln\left(1 + \frac{\sigma_z(W)}{h_0 + \sigma_z(L)}\right), \tag{6.2}$$

where $\sigma_z(x)$ is the vertical spread of a plume at a distance x from a surface-level release.

Integrating Dispersion Models into a Modeling System

The models for estimating dispersion of pollutants emitted from vehicles traveling on roads, described in Chapter 4, The Impact of Highways on Urban Air Quality, can be readily incorporated into a modeling system that estimates the cumulative impact of the large number of road segments typical of an urban area (Arunachalam et al., 2014; Barzyk et al., 2015). It involves applying the model for a finite line source for each of the roads, and summing up the resulting concentrations. One of the uncertainties in this exercise is estimating the micrometeorological inputs in urban areas. The next section discusses this issue.

The evaluation and application of the vertical dispersion model (VDM) in Chapter 5, The Impact of Buildings on Urban Air Quality, has focused on a single street in a city block. How do we apply the model to estimate near surface concentrations in an urban area with a large number of roads? One approach is to use a model such as AERMOD (Cimorelli et al., 2005) to estimate concentrations at the effective top of the urban canopy assuming that the roads are the same level as the canopy top. The meteorological inputs would account for the roughness of the urban area averaged over the scale of the urban built-up area. The internal boundary layer (IBL) model, described in the next section, can be used to estimate these inputs. The resulting concentrations correspond to the rooftop values which can be then used to estimate the concentration at street level using

$$C_s = C_{AERMOD} + \frac{q}{\beta\sigma_w W}\left(\frac{1+a_r}{1+(1+a_r)\left(h_0/H\right)}\right), \tag{6.3}$$

where the parameters in the second term on the right-hand side of the equation correspond to the road of interest. Note that this term goes to zero when a_r or H goes to zero, and we recover the AERMOD concentration for flat terrain.

Eq. (6.3) assumes that the street-level concentration consists of two components: (1) concentration associated with local vehicle emissions, which includes the effects of buildings on dispersion, and (2) roof-level concentration, which includes contributions associated with emissions from other streets in the urban area. Thus, it accounts indirectly for the effects of emissions from all the streets on the street-level concentration at a specific street. It is still an approximation because VDM does not treat the horizontal transport of emissions between streets below the urban

canopy. There are other models (Soulhac et al., 2011) that explicitly account for advection of emissions between streets, but are more complex than VDM. More study is required to examine whether this added complexity yields better model performance relative to that of VDM.

Recall that in Eq. (6.3), σ_w is the standard deviation of the vertical velocity fluctuations averaged over the effective height of the buildings lining a city block. It is related to the rooftop value, σ_{wr}, through the equation

$$\sigma_w = \frac{\sigma_{wr}}{(1+\eta a_r)^{1/3}}, \tag{6.4}$$

where $\eta = 0.4$. Thus, σ_w is reduced relative to σ_{wr}, and the reduction depends on the aspect ratio, a_r.

The higher roughness and upward heat flux over the urban area relative to the upwind rural area will result in a higher σ_{wr} at the urban rooftop level. This will reduce the concentrations at roof-top relative to those at ground level *in the absence of buildings*. However, the presence of the buildings can increase the concentrations relative to the flat-terrain rural scenario through two mechanisms: (1) the reduction of average σ_w that governs street-level concentrations—see Eqs. (6.3) and (6.4)—and (2) the reduction of dispersion by buildings, which is captured by the term within the parenthesis in the second term on the right-hand side of Eq. (6.3), which we refer to as the building effect:

$$\text{Building effect} = \left(\frac{1+a_r}{1+(1+a_r)\left(h_0/H\right)}\right), \tag{6.5}$$

We see that for small (h_0/H), the building effect increases as $(1 + a_r)$.

The street-level concentrations depend on roof-top micrometeorological variables. We address this topic in the next section.

Meteorological Inputs-Internal Boundary Layer Model

Meteorological inputs for the dispersion models can be estimated using near-surface measurements of wind speed made at airports located in suburban areas, and corresponding information on the roughness length and albedo. How can these estimates be transferred to an urban area with different surface characteristics? The meteorological processor in AERMOD (Cimorelli et al., 2005) accounts for the effects of the urban surface through a heat flux that is proportional to the difference between the

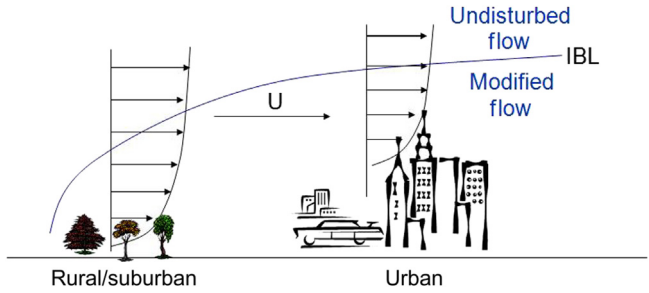

Figure 6.2 Development of an internal boundary layer (IBL) as air travels from the rural to the urban area.

surface temperatures at the urban and rural areas. This "Heat Island" temperature difference is related to the population of the urban area through an empirical equation. This results in a convective boundary layer in the urban area even when the boundary layer in the upwind rural area is stable. The increased roughness coupled with the upward heat flux in the urban area results in increased turbulence levels at urban roof-level relative to those in the rural area.

Another approach to estimating urban meteorological inputs is to apply a model that traces the evolution of the layer next to the ground as the boundary layer from the upwind rural area is advected on to the urban surface. Fig. 6.2 illustrates this concept.

The height, h, of the IBL grows with distance from the rural area. One model proposed by Miyake (see Savelyev and Taylor, 2005) estimates this height by assuming that its growth rate is proportional to standard deviation of the vertical velocity fluctuations at the top of the IBL resulting in the equation:

$$\frac{dh}{dx} = A\left(\frac{\sigma_w}{U}\right)_u = f\left(\frac{h}{L_u}, \frac{h}{z_{0u}}\right), \tag{6.6}$$

where the subscript "u" refers to urban values and L is the Monin-Obukhov length, and $A \sim 1$. Eq. (6.6) assumes that the IBL is in equilibrium with the underlying surface, and the ratio $\left(\sigma_w/U\right)$ can be estimated from Monin−Obukhov similarity theory, denoted by the function f in the third term of the equation. This equation can be integrated if we can estimate the variation of the roughness length, z_{0u}, and Monin-Obukhov length, L_u, over the urban area. Then, the friction velocity at an urban

location is computed by assuming that the mean velocities at h are the same at the urban and the rural upwind locations, $U_u(h) = U_r(h)$, giving

$$u_{*u} = u_{*r}\frac{\phi(h/L_r, h/z_{0r})}{\phi(h/L_u, h/z_{0u})} \tag{6.7}$$

where $\phi = \ln(h/z_0) + \psi_M(z_0/L) - \psi_M(h/L)$ and ψ_M is a function that accounts for stability, which is given in Eq. (3.28) and Eq. (3.29).

Luhar et al. (2006) applied this model to analyze data from the Basel Urban Boundary Layer Experiment (BUBBLE) conducted in the city of Basel, Switzerland (Rotach et al., 2005). The model provided adequate estimates of the urban friction velocity and σ_w at roof-level assuming that the urban Obukhov length is the same as that in the rural area under unstable conditions and that it is very large (neutral) in stable rural conditions. These results are supported by a study conducted in Riverside, CA between July and September, 2015. One of the major objectives of this study was to evaluate a model to estimate the rooftop micrometeorological variables using measurements made upwind. A Campbell scientific CSAT3 sonic anemometer was used to measure the three components of the wind speed vector and the sonic temperature at 10 Hz at 3 m above the 25 m high roof of city hall. Another sonic anemometer was placed at Riverside airport, about 7.8 km southwest from city hall, at 2.7 m above ground level. The airport is usually upwind of the urban site.

The left panel of Fig. 6.3 shows the comparison of the values of u_* estimated at the urban rooftop using the IBL model with corresponding

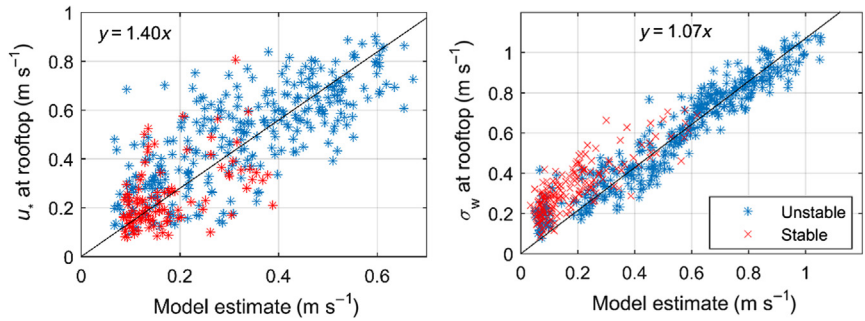

Figure 6.3 Left panel: Comparison of observations with IBL model using Eq. (6.6) and Eq. (6.7) where σ_w is given by Eq. (3.37), the wind speed U is given by Eq. (3.23) and A = 1. The model assumes neutral conditions in urban area. Right panel: Results from Eq. (6.8) where we have used Eq. (3.37) to estimate σ_w. Different markers indicate unstable and stable upwind surface layer conditions.

observations. The performance of the model is adequate although the urban surface friction velocity is underestimated.

A simplified form of the IBL model was evaluated in Schulte et al. (2015). This model was also recommended by Fisher et al. (2006) to estimate the value of the urban surface friction velocity from rural measurements. The basic form of the model is:

$$\frac{u_{*urban}}{u_{*rural}} = \left[\frac{z_{0urban}}{z_{0rural}}\right]^{\alpha} \tag{6.8}$$

where α is an empirical constant. Fisher et al. (2006) recommends a value of 0.0706. However, based on sensitivity studies of the IBL model, $\alpha = 0.14$ to produces the best agreement between Eq. (6.8) and the IBL model. Since for neutral conditions $\sigma_w = 1.3u_*$, Eq. (6.8) also represents the ratio of σ_w at the rooftop to that at the airport. The right panel of Fig. 6.3 shows that this empirical model performs as well or better than the IBL model.

Note that the model indicates that the larger urban roughness has a relatively small effect on the friction velocity at roof level: if the urban roughness length is a factor of 5 higher than the upwind roughness length, the friction velocity increases by a factor of 1.25. This suggests that the main effect of buildings on street-level concentrations occurs through the reduction in vertical dispersion indicated by the aspect ratio factor in Eq. (6.5).

We note that comprehensive models, such as that proposed by Masson (2000), might provide better estimates of turbulent velocities in urban areas. However, at this point, it is not clear that more complex models are required for dispersion applications in urban areas.

REFERENCES

Arunachalam, S., Barzyk, T., Isakov, V., Venkatram, A., Snyder, M., Rice, N.A., et al., 2014. C-port: a community-scale near-source air quality system to assess port-related air quality impacts, in: HARMO 2014 – 16th International Conference on Harmonisation within Atmospheric Dispersion Modelling for Regulatory Purposes, Proceedings.

Barzyk, T.M., Isakov, V., Arunachalam, S., Venkatram, A., Cook, R., Naess, B., 2015. A near-road modeling system for community-scale assessments oftraffic-related air pollution in the United States. Environ. Model. Softw. 66, 46–56. Available from: https://doi.org/10.1016/j.envsoft.2014.12.004.

Cimorelli, A.J., Perry, S.G., Venkatram, A., Weil, J.C., Paine, R.J., Wilson, R.B., et al., 2005. AERMOD: a dispersion model for industrial source applications. Part I: general model formulation and boundary layer characterization. J. Appl. Meteorol. 44. Available from: https://doi.org/10.1175/JAM2227.1.

Fisher, P., Kukkonen, J., Piringer, M., Rotach, M.W., Schatzmann, M., 2006. Meteorology applied to urban air pollution problems: concepts from COST 715. Atmos. Chem. Phys. Discuss. 6, 555–564. Available from: https://doi.org/10.5194/acpd-5-7903-2005.

Luhar, A.K., Venkatram, A., Lee, S.M., 2006. On relationships between urban and rural near-surface meteorology for diffusion applications. Atmos. Environ. 40, 6541–6553. Available from: https://doi.org/10.1016/j.atmosenv.2006.05.067.

Masson, V., 2000. A physically-based scheme for the urban energy budget in atmospheric models. Boundary-Layer Meteorol. 94, 357–397. Available from: https://doi.org/10.1023/A:1002463829265.

Rotach, M.W., Vogt, R., Bernhofer, C., Batchvarova, E., Christen, A., Clappier, A., et al., 2005. BUBBLE – an urban boundary layer meteorology project. Theor. Appl. Climatol. 81, 231–261. Available from: https://doi.org/10.1007/s00704-004-0117-9.

Savelyev, S.A., Taylor, P.A., 2005. Internal boundary layers: I. Height formulae for neutral and diabatic flows. Boundary-Layer Meteorol. 115, 1–25.

Schulte, N., Tan, S., Venkatram, A., 2015. The ratio of effective building height to street width governs dispersion of local vehicle emissions. Atmos. Environ. 112, 54–63. Available from: https://doi.org/10.1016/j.atmosenv.2015.03.061.

Soulhac, L., Salizzoni, P., Cierco, F.X., Perkins, R., 2011. The model SIRANE for atmospheric urban pollutant dispersion; part I, presentation of the model. Atmos. Environ. 45, 7379–7395. Available from: https://doi.org/10.1016/j.atmosenv.2011.07.008.

APPENDIX A

Dispersion From an Elevated Point Source

Most of the air quality impact of urban transportation is caused by emissions close to ground level, which is the reason that this book deals primarily with models for dispersion of pollutants from ground-level sources. In this appendix we provide a basic understanding of dispersion from elevated releases to allow the reader to appreciate dispersion models used in other applications. We refer to a source as elevated if it is located above a 10th of the boundary layer height, although this definition is not always clear cut. In this part of the boundary layer we assume that the wind speed is more or less constant with height.

MODELING A POINT SOURCE

We model dispersion from an elevated source by considering an idealized point source located at $z = h_e$, with the x-axis of the coordinate system aligned along the wind direction at the source, as shown in Fig. A.1. The time-averaged (typically 1 hour) concentration field is described using the following Gaussian distribution:

$$C(x, y, z) = \frac{Q}{2\pi\sigma_y\sigma_z U} \exp\left[-\frac{(z-h_e)^2}{2\sigma_z^2} - \frac{y^2}{2\sigma_y^2}\right] \tag{A.1}$$

where y is the crosswind coordinate, Q is the source strength (mass/time), U is the time-averaged wind speed at source height, and σ_y and σ_z are the plume spreads normal to the mean wind direction.

Eq. (A.1) assumes that along-wind dispersion is much smaller than transport by the mean wind. This assumption breaks down when the mean wind is comparable to the turbulent velocity along the wind, σ_u. The form of the dispersion model under low wind speed conditions is discussed in a later section.

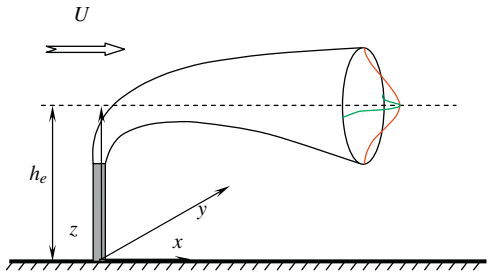

Figure A.1 Gaussian distribution used to model a plume from a point source.

The effect of the ground on concentrations is accounted for by making sure that there is no flux of material through the ground, which is taken to be $z = 0$. The mathematical trick to achieve this is to place an "image" source at a distance $z = -h_e$, where h_e is the effective height of the source above ground. The upward flux from this image source essentially cancels out the downward flux from the real source without affecting the mass balance. Then the concentration becomes

$$C(x, y, z) = \frac{Q}{2\pi\sigma_y\sigma_z U}\exp\left[-\frac{y^2}{2\sigma_y^2}\right]\left\{\exp\left[-\frac{(z-h_e)^2}{2\sigma_z^2}\right] + \exp\left[-\frac{(z+h_e)^2}{2\sigma_z^2}\right]\right\} \tag{A.2}$$

In the real atmosphere, dispersion in the upward direction is limited by the height of the atmospheric boundary layer. This limitation of vertical mixing is incorporated into the Gaussian formulation by "reflecting" material off the top of the mixed layer. Then Eq. (A.2) can be modified to account for the infinite set of "reflections" from the ground and the top of the mixed layer (see Csanady, 1973). When the pollutant is well mixed through the depth of the boundary layer, z_i, the expression for the concentration becomes

$$C(x, y) = \frac{Q}{\sqrt{2\pi}\sigma_y z_i U}\exp\left(-\frac{y^2}{2\sigma_y^2}\right). \tag{A.3}$$

Eq. (A.2) can be modified to account for dry deposition of material at the surface. The Gaussian formulation for a point source can be used to model volume, area, and line sources because each of these source types can be discretized into point sources; the associated concentrations are simply the sums of the contributions from these point sources. The

application of Eq. (A.2) requires formulation for several variables: (1) plume spreads σ_y and σ_z, (2) the effective height of release h_e , and (3) the effective wind speed U.

Horizontal Plume Spread of Elevated Releases

The horizontal spread of elevated releases is usually modeled using the following expression:

$$\sigma_y = \frac{\sigma_v T}{\left(1 + T/2\tau_{Lv}\right)^{1/2}} \tag{A.4}$$

where T is the travel time, x/U, where U and σ_v are evaluated at effective plume height. This form of the equation corresponds to a more general equation derived by Taylor (1922) for the Lagrangian statistics of particles released into a homogeneous turbulent flow. Here the spread of the plume in different directions is modeled as the spread of particles released sequentially from a point source. We provide a simple interpretation of the equation suggested by Taylor. The Lagrangian time scale, which we denote by τ, is essentially the time scale over which a particle embedded in turbulent flow loses memory of its initial velocity. One way of thinking about this is to picture particle motion as a series of straight-line trajectories that change direction at time intervals of τ. The velocity of the particle at the end of these intervals is chosen from the distribution of turbulent velocities at the location of the particle.

Consider the motion of a particle in the crosswind y-direction, released from a point in a uniform flow in which the statistics of the turbulent velocities do not vary with distance along any one coordinate direction. If the time of travel, T, is much less than the Lagrangian time scale, τ, this distance is simply

$$Y = v_i T \tag{A.5}$$

We denote the mean over an ensemble of particles released by angle brackets. The mean crosswind spread of the ensemble of particles at time, T, is zero because $\langle v_i \rangle = 0$. The variance of particle spread becomes

$$\left\langle Y^2 \right\rangle = \sigma_y^2 = \left\langle v_i^2 \right\rangle T^2 = \sigma_v^2 T^2 \tag{A.6}$$

so that

$$\sigma_y = \sigma_v T \text{ when } T \ll \tau. \tag{A.7}$$

When $T \gg \tau$ the distance traveled by this particle, Y, after time T from its release point is

$$Y = \sum_{i=1}^{i=N} v_i \tau, \tag{A.8}$$

where $N = \frac{T}{\tau}$. Then the expression for the variance of the spread becomes

$$\langle Y^2 \rangle = N \langle v_i^2 \rangle \tau^2 + \tau^2 \sum_{i \neq j} \langle v_i v_j \rangle. \tag{A.9}$$

The second term on the right-hand side of the equation is zero because the velocities in each of the intervals are uncorrelated, and Eq. (A.9) becomes

$$\langle Y^2 \rangle = \sigma_y^2 = N \langle v_i^2 \rangle \tau^2 = \frac{T}{\tau} \sigma_v^2 \tau^2 = \sigma_v^2 \tau T, \tag{A.10}$$

so that

$$\sigma_y = \sigma_v (T\tau)^{1/2} \text{ when } T \gg \tau. \tag{A.11}$$

A more complete mathematical analysis yields the factor 2 multiplying the right side of the equation. The asymptotic linear and square root dependence of plume spread on time of travel are captured in Eq. (A.4) for the horizontal spread.

The application of Eq. (A.4) requires expressions for the time of travel, T, and the Lagrangian time scale. The time scale for horizontal spread is expressed in terms of a length scale l, and σ_v, $\tau_{Lv} = l/\sigma_v$. The length scale is taken to be proportional to a length characterizing the eddies responsible for transport, and the constant of proportionality is obtained by fitting estimates of plume spread from Eq. (A.4) to observations. For example, Draxler (1976) found that a Lagrangian time scale of the order of 100 seconds provides an adequate description of the data that he analyzed; his analysis uses wind speed at release height to estimate travel time from source to receptor. Note that there is little consensus on the appropriate time scale. One approach is simply to assume that the time scale is infinite, leading to $\sigma_y = \sigma_v x/U$.

Vertical Plume Spread Formulations

The expressions for vertical plume spread for elevated releases are also based on theoretical analysis first proposed by Taylor (1922). The expressions for the vertical plume spread are based on

$$\sigma_z = \frac{\sigma_w x}{U}\left(1+\frac{x}{2U\tau_{Lw}}\right)^{-1/2}, \tag{A.12}$$

where τ_{Lw} is the Lagrangian time scale, whose formulation will be discussed later. This expression strictly applies to a boundary layer in which the mean and turbulent properties are constant in space. To apply it to a real boundary layer in which the properties are highly inhomogeneous, we can use one of two approaches. The first is to average the turbulence and mean properties over the region of interest, and use the average properties in the homogeneous formulations. This is not as straightforward as it seems because the limits of the average require an estimate of the plume dimensions, which in turn depends on the average properties. Furthermore the averaging procedure is necessarily arbitrary. The validity of the method needs to be established by comparing the results obtained from the formulations with observations or theory that accounts for inhomogeneity more explicitly. In general, empirical knowledge derived from observations plays a major role in the development of practical models of dispersion. As in most turbulence research, theory can suggest plausible forms for a dispersion model, but the model usually contains parameters that have to be estimated from observations.

In some dispersion models, the meteorological variables σ_w, σ_v, and U are evaluated at the effective height of the plume. Alternatively, these variables correspond to averages between the effective source height and ground level, with the justification that the material sees this average as it travels from source to ground level.

Even if we could treat the boundary layer as vertically homogeneous the presence of boundaries, such as the ground and the top of the mixed layer, makes it difficult to estimate the Lagrangian time scale from a priori considerations. Thus the time scale is often treated as an empirical parameter that is derived by fitting plume spread expressions to observations. The Lagrangian time scale, τ_{Lw}, is generally taken to be l/σ_w, where l is a length scale. We will derive an expression for this length scale using the

expression for eddy diffusivity in Chapter 3, Fundamentals of Micrometeorology and Dispersion:

$$K = \sigma_w l \tag{A.13}$$

Here we show how the Monin-Obukhov relationships that apply to the near surface boundary layer can be extended to the upper boundary layer to yield the required length scale, l.

As in the surface layer, we will derive the expression for the length scale by interpolating between the neutral and stable limits. The eddy diffusivity for heat when the boundary layer is very stable is

$$K_H = \frac{k u_* L}{\beta}, \tag{A.14}$$

where $k = 0.4$ and $\beta = 4.7$. Comparing Eqs. (A.13) and (A.14) yields

$$l = \frac{k}{\beta}\left(\frac{u_*}{\sigma_w}\right) L. \tag{A.15}$$

To apply this equation to the upper boundary layer, we need an expression for L

$$L = -\frac{T}{g}\frac{u_*^3}{kH}, \tag{A.16}$$

in the surface layer in terms of the local temperature gradient. The kinematic heat flux, H, is given by

$$H = -K_H \frac{d\theta}{dz} = -\frac{k u_* L}{\beta}\frac{d\theta}{dz}. \tag{A.17}$$

The local temperature gradient can be written in terms of the Brunt–Vaisala frequency, N,

$$N^2 = \frac{g}{T}\left(\frac{d\theta}{dz}\right) \text{ or } \frac{d\theta}{dz} = \frac{T}{g}N^2. \tag{A.18}$$

Eqs. (A.17) and (A.18) when substituted in Eq. (A.16) yields

$$L = \frac{u_*}{k}\frac{\sqrt{\beta}}{N}. \tag{A.19}$$

Eq. (A.19) in Eq. (A.15) provides the required expression for the stable length scale, l_s

$$l_s = \frac{1}{\sqrt{\beta}} \frac{u_*^2}{\sigma_w} \frac{1}{N}. \tag{A.20}$$

If we use the $\sigma_w = 1.3u_*$ and $\beta = 4.7$, we obtain the numerical coefficient in the length scale

$$l_s = 0.27 \frac{\sigma_w}{N}. \tag{A.21}$$

Under neutral conditions

$$K = ku_* z = \sigma_w l_n, \tag{A.22}$$

where l_n is the neutral length scale. Eq. (A.22) and $\sigma_w = 1.3u_*$ yields $l_n = 0.31z$. We can now interpolate between the two limits to derive the Lagrangian integral time scale under stable conditions for elevated releases

$$\begin{aligned} T_{Lw} &= \frac{l}{\sigma_w} \\ \frac{1}{l} &= \frac{1}{l_s} + \frac{1}{l_n} \\ l_s &= 0.27 \frac{\sigma_w}{N}; l_n = 0.31 h_e \end{aligned} \quad , \tag{A.23}$$

where h_e is the effective height of release. The expression for the length scale emphasizes the smaller of the length scales.

When the boundary layer is unstable, τ_{Lw} is taken to be proportional to the time scale of the largest eddies at source height, so that the appropriate length scale is $l_n = 0.31h_e$.

Plume Spreads Induced by Source Effects and Plume Rise

All the previous expressions for spread assume point releases. In practice, the plume is well mixed over a finite area at the source because of effects induced by the physical dimensions of the source. For example, material released on the top of a building is likely to be mixed into the wake of the building before it is spread by atmospheric turbulence. A simple way to account for this is by adding the spread associated with the source to

both the horizontal and the vertical spreads of the plume in the following manner:

$$\sigma^2_{t(y,z)} = \sigma^2_{s(y,z)} + \sigma^2_{y,z}, \tag{A.24}$$

where "t" refers to total plume spread, "s" refers to source effects, and the last term on the right-hand side refers to that associated with atmospheric turbulence. We will provide some methods for estimating the plume spread associated with source effects in a later section.

Buoyancy and momentum associated with the release can also induce additional plume spread. This additional spread, σ_p, which is proportional to plume rise, is also accounted for in Eq. (A.24) as follows:

$$\sigma^2_{t(y,z)} = \sigma^2_{s(y,z)} + \sigma^2_{y,z} + \sigma^2_p. \tag{A.25}$$

The expressions for plume spreads from releases at an arbitrary height in the boundary layer can be formulated by combining the plume spreads for surface release with those from an elevated release,

$$\sigma_{y,z} = (1-f)\sigma_{y,z(\text{surface})} + f\sigma_{y,z(\text{elevated})}, \tag{A.26}$$

where the interpolating factor f is taken to be the ratio of the effective release height to the mixed layer height to ensure the correct limiting behavior.

We next estimate the effective height of a source when the pollutant is released with buoyancy and momentum.

Plume Rise

Most elevated releases are associated with momentum and buoyancy to increase the effective height of the release. The effective stack height, h_e, is then given by

$$h_e = h_s + h_p, \tag{A.27}$$

where h_s is the physical stack height, and h_p is the plume rise. Most practical plume rise models are based on the plume rise in a neutral atmosphere with a constant wind speed, U (Weil, 1988)

$$h_p = \left(\frac{3}{\beta^2}\frac{F_m}{U}t + \frac{3}{2\beta^2}\frac{F_b}{U}t^2\right)^{1/3}, \tag{A.28}$$

where β is an entrainment parameter taken to be 0.6, $t = x/U$ is the time of travel from the source, and the momentum flux, F_m, and the buoyancy flux, F_b, of the plume are given by

$$F_m = v_s^2 r_s^2 \left(\frac{T_a}{T_s}\right)$$
$$F_b = \frac{g}{T_a} v_s r_s^2 (T_s - T_a) \tag{A.29}$$

where v_s is the velocity of the exhaust gases, r_s is the stack inner radius, T_s is the exhaust gas temperature, and T_a is the ambient temperature.

Eq. (A.28) is a useful approximation when the plume is rising in the unstable boundary layer in which the potential temperature is relatively uniform in the vertical. However, the formulation assumes that the growth of the plume is dominated by turbulence induced within the plume by the vertical motion of the rising plume. Atmospheric turbulence is important in the later stages of plume rise when the rise velocity becomes comparable to the standard deviation of the vertical velocity fluctuations, σ_w. Although the effects of atmospheric turbulence can be explicitly accounted for when the plume is rising, it is generally assumed that atmospheric turbulence only affects the final plume rise when the plume levels off. The plume is assumed to reach its final height when the plume rise rate is comparable to σ_w,

$$\frac{dh_p}{dt} = \sigma_w. \tag{A.30}$$

In most plumes, buoyancy dominates initial plume momentum by the time the plume reaches its final height. Then Eqs. (A.28) and (A.30) yield the final plume rise, h_f

$$h_f = \frac{2}{3\beta^2} \frac{F_b}{U\sigma_w^2}. \tag{A.31}$$

The equations governing the rise of a plume in a stable atmosphere (gradient of potential temperature is positive) accounts for the fact that plume buoyancy relative to the atmosphere decreases as the plume rises. The solution for the path of the plume differs from that given by Eq. (A.31). However, practical dispersion models assume that the Eq. (A.28) holds until the plume reaches its final height given by

$$h_f = \left(\frac{6}{\beta^2}\frac{F_b}{UN^2}\right)^{1/3}, \tag{A.32}$$

where N is the Brunt–Vaisala frequency of the atmosphere defined by

$$N = \left(\frac{g}{T_a}\frac{d\theta}{dz}\right)^{1/2}, \tag{A.33}$$

where $d\theta/dz$ is the average potential temperature gradient in the atmospheric layer that the plume rises through.

As indicated earlier the plume model assumes a vertically homogeneous atmosphere. The formulation is applied in the real atmosphere by using the properties at the stack height to represent the entire boundary layer. This approximation can be improved iteratively by first calculating the plume rise using properties at stack height, and then using averages over the plume rise height. The errors in such approximations become critical near the ground where wind speed and temperature change substantially with height. Some practical dispersion models avoid these errors through numerical solution of the governing equations, which explicitly account for the variation of atmospheric properties with height.

Most dispersion models account for the interaction of the rising plume with the inversion capping the mixing layer height through a "plume penetration factor," which is a function of the plume buoyancy and the temperature difference across the capping inversion. This factor multiplies the emission rate of the source. When the plume completely penetrates the inversion and is trapped within the elevated stable layer, the factor is zero. When the plume does not have sufficient buoyancy to penetrate the inversion, the factor is taken to be unity. All the material within the atmospheric boundary layer is "reflected" from the top of the boundary layer.

Plume Rise Equations

We derive the plume rise equations using a simple model of the plume, which assumes that the plume properties such as temperature and velocity are uniform across the cross-section of the plume; this is referred to as the top hat approximation. The plume rises in a boundary layer characterized by a uniform horizontal wind speed u, and stratification characterized by the Brunt–Vaisala frequency, N, defined by Eq. (A.33).

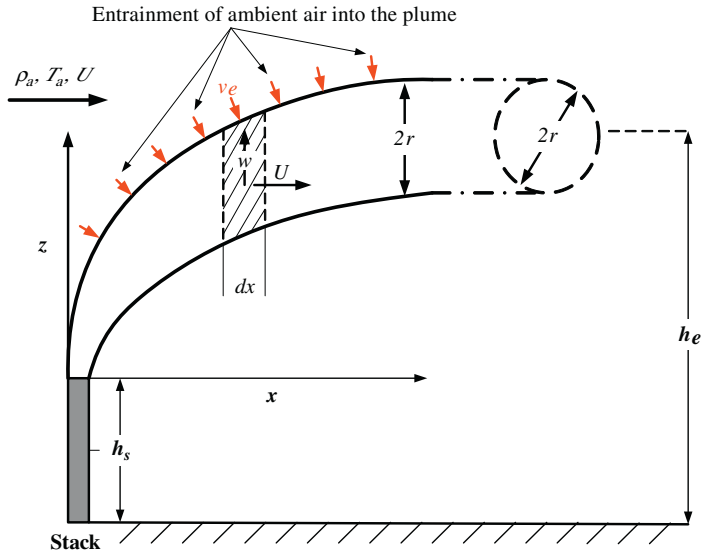

Figure A.2 Plume control volume used to derive plume rise equations.

For simplicity, we assume that the plume bends over rapidly enough that the horizontal velocity inside the plume is equal to the ambient horizontal wind speed, U, which is taken to be uniform with height. Fig. A.2 shows a control volume of thickness dx that encloses a plume with a radius r.

Plume rise corresponds to the vertical position of the plume, z, as a function of distance, x, from the stack.

We start with the mass conservation equation for air, which states that the change in the plume mass flux with downwind distance is caused by the entrainment of ambient air into the plume as

$$d(\rho_p U \pi r^2) = 2\pi r \rho_a v_e dx \tag{A.34}$$

where ρ_p and ρ_a are the plume and ambient densities, respectively, r is the radius of the plume, U is the ambient horizontal wind speed that is assumed to be constant, and v_e, the entrainment velocity, is taken to be proportional to the vertical velocity of the plume,

$$v_e = \beta w, \tag{A.35}$$

where w is the vertical velocity of the plume and β is an entrainment coefficient. Substituting Eq. (A.35) in Eq. (A.34), and assuming constant horizontal wind speed U, results in

$$U\frac{d}{dx}(\rho_p r^2) = 2r\rho_a \beta w. \tag{A.36}$$

Assuming that the density difference between the plume and ambient air is relevant only when buoyancy forces are considered, replacing w with dz/dt, and noticing that $U\frac{d}{dx} = \frac{d}{dt}$, Eq. (A.36) becomes

$$\frac{dr}{dt} = \beta\frac{dz}{dt} \tag{A.37}$$

or

$$r = \beta z + r_0, \tag{A.38}$$

where r_0 is the radius of the plume at $z = 0$.

The conservation of vertical momentum states

$$d(\rho_p U w \pi r^2) = F_u \rho_p \pi r^2 dx \tag{A.39}$$

where F_u is the buoyancy force in the unit mass of the plume, which is

$$F_u = g\frac{(T_p - T_a)}{T_a} = \left(\frac{T_p}{T_a} - 1\right)g \simeq \frac{g}{T_a}(\theta_p - \theta_a). \tag{A.40}$$

Then Eq. (A.39) becomes

$$\frac{d}{dx}(Uwr^2) = \frac{g}{T_a}(\theta_p - \theta_a)r^2, \tag{A.41}$$

which can be written as

$$\frac{d}{dt}\left(wr^2\right) = \frac{g}{T_a}\left(\theta_p - \theta_a\right)r^2. \tag{A.42}$$

The conservation of energy in the plume states that the change in enthalpy flux is equal to the entrainment of enthalpy into the plume, which simplifies to

$$\frac{d}{dt}\left(r^2\theta_p\right) = \theta_a\frac{dr^2}{dt}, \tag{A.43}$$

where we have assumed that the differences in densities and specific heats of the boundary layer and the plume can be neglected. We can rewrite Eq. (A.43) as follows:

$$\frac{d}{dt}\left(r^2\theta_p\right) = \frac{d}{dt}\left(r^2\theta_a\right) - \frac{d\theta_a}{dt}r^2 \tag{A.44}$$

and

$$\begin{aligned}\frac{d}{dt}\left(r^2\theta_p\right) &= \frac{d}{dt}\left(r^2\theta_a\right) - \frac{d\theta_a}{dz}\frac{dz}{dt}r^2 \\ &= \frac{d}{dt}\left(r^2\theta_a\right) - \frac{d\theta_a}{dz}\frac{1}{\beta}\frac{dr}{dt}r^2.\end{aligned} \tag{A.45}$$

Then using the definition of the Brunt–Vaisala frequency, Eq. (A.45) becomes

$$\frac{d}{dt}\left(\frac{g}{T_a}r^2\left(\theta_p - \theta_a\right)\right) = -\frac{N^2}{3\beta}\frac{dr^3}{dt}, \tag{A.46}$$

which can be integrated to yield

$$\frac{g}{T_a}r^2\left(\theta_p - \theta_a\right) = \frac{g}{T_a}r_0^2\left(\theta_{0p} - \theta_{0a}\right) - \frac{N^2}{3\beta}\left(r^3 - r_0^3\right), \tag{A.47}$$

where the subscript "0" refers to properties when the plume bends over. Now, we assume that the energy flux through the plume when it bends over is equal to that at the source, so that

$$\frac{g}{T_a}Ur_0^2\left(\theta_{0p} - \theta_{0a}\right) = \frac{g}{T_a}v_s r_s^2(T_s - T_a), \tag{A.48}$$

where v_s is the velocity of the gas at the stack, T_s is the temperature, r_s is the stack radius, and T_a is the ambient temperature at the stack mouth. The left-hand side of the equation is the energy flux through the plume multiplied by g/T_a. The right-hand side of the equation is called the buoyancy flux denoted by F_b. With these definitions, Eq. (A.48) becomes

$$\frac{g}{T_a}r^2\left(\theta_p - \theta_a\right) = \frac{F_b}{U} - \frac{N^2}{3\beta}\left(r^3 - r_0^3\right). \tag{A.49}$$

Substituting Eq. (A.49) into the vertical momentum Eq. (A.41) yields

$$\frac{d}{dt}\left(wr^2\right) = \frac{F_b}{U} - \frac{N^2}{3\beta}\left(r^3 - r_0^3\right), \tag{A.50}$$

which can be written as

$$\frac{d}{dt}\left(\frac{1}{\beta}\frac{dr}{dt}r^2\right) = \frac{F_b}{U} - \frac{N^2}{3\beta}\left(r^3 - r_0^3\right), \tag{A.51}$$

which becomes

$$\frac{d}{dt}\left(\frac{1}{3\beta}\frac{dr^3}{dt}\right) = \frac{F_b}{U} - \frac{N^2}{3\beta}\left(r^3 - r_0^3\right). \tag{A.52}$$

Now substitute $p = \left(r^3 - r_0^3\right)\frac{1}{3\beta}$ in Eq. (A.52) to obtain

$$\frac{d^2p}{dt^2} + N^2 p = \frac{F_b}{U}. \tag{A.53}$$

The solution of this second order differential equation is as follows:

$$p = A\sin(Nt) + B\cos(Nt) + \frac{F_b}{UN^2}. \tag{A.54}$$

The constants A and B are obtained by specifying p and dp/dt at $t = 0$. At $t = 0$, $p = 0$ from its definition, so that

$$B = -\frac{F_b}{UN^2}. \tag{A.55}$$

Now the definition of p gives

$$\frac{dp}{dt} = \frac{r^2}{\beta}\frac{dr}{dt} = \frac{r^2}{\beta}\beta w = r^2 w. \tag{A.56}$$

At $t = 0$,

$$\frac{dp}{dt} = r_0^2 w_0. \tag{A.57}$$

As in the case of buoyancy flux, we assume that the momentum flux when the plume bends over is equal to the momentum flux from the stack,

$$U r_0^2 w_0 = r_s^2 v_s^2 \equiv F_m, \tag{A.58}$$

where F_m is the called the momentum flux. Eq. (A.29) corrects F_m for the difference in air densities between the stack mouth and the surrounding air. Then substituting Eq. (A.58) into Eq. (A.57) and equating to the first derivative of p in Eq. (A.54) we get the constant A,

$$A = \frac{F_m}{UN}, \tag{A.59}$$

and the solution Eq. (A.54) becomes

$$\frac{1}{3\beta}\left(r^3 - r_0^3\right) = \frac{F_m}{UN}\sin(Nt) + \frac{F_b}{UN^2}(1 - \cos(Nt)). \tag{A.60}$$

Substituting, $r = r_0 + \beta z$ (Eq. A.38) into Eq. (A.60), we get the final expression for plume rise in a boundary layer with stratification N,

$$z = \left[\left(\frac{r_0}{\beta}\right)^3 + \frac{3}{U\beta^2}\left(\frac{F_m}{N}\sin(Nt) + \frac{F_b}{N^2}(1-\cos(Nt))\right)\right]^{1/3} - \frac{r_0}{\beta}. \tag{A.61}$$

When the boundary is neutral, N approaches zero, so that we can replace

$$\begin{aligned} \sin(Nt) &\simeq Nt \\ 1 - \cos(Nt) &\simeq \frac{N^2t^2}{2} \end{aligned} \tag{A.62}$$

in Eq. (A.61) to obtain

$$z = \left[\left(\frac{r_0}{\beta}\right)^3 + \frac{3}{U\beta^2}\left(F_m t + \frac{F_b}{2}t^2\right)\right]^{1/3} - \frac{r_0}{\beta}. \tag{A.63}$$

If we assume that r_0 is small compared to the plume rise, we obtain the plume rise equations in the previous section.

Note that the solution for plume rise in a stable atmosphere suggests oscillations of the plume, which are not observed in the real atmosphere. The practical approach is to assume that the plume rises as it would in a neutral atmosphere until it reaches a maximum of Eq. (A.63). If we neglect r_0 the maximum plume rise in stable conditions works out to be

$$z_{\max}(\text{stable}) = \left(\frac{3}{\beta^2}\frac{F_b}{UN^2}\left(1 + \left(1 + \frac{F_m^2N^2}{F_b^2}\right)^{1/2}\right)\right)^{1/3}. \tag{A.64}$$

If the momentum flux is small, we get

$$z_{\max}(\text{stable}) = \left(\frac{6}{\beta^2}\frac{F_b}{UN^2}\right)^{1/3}. \tag{A.65}$$

Building Downwash

Buildings and other structures near a relatively short stack can have a substantial effect on plume transport and dispersion, and on the resulting ground-level concentrations that are observed. The "rule of thumb" is that a stack should be at least 2.5 times the height of adjacent buildings to avoid the effects of the buildings. Much of what is known of the effects of buildings on plume transport and diffusion has been obtained from wind tunnel and field studies.

When the airflow meets a building (or other obstruction), it is forced around, up and over the building. On the lee side of the building, the flow separates, leaving a closed circulation containing lower wind speeds (see Fig. A.3). The building also creates a "wake" of increased turbulence, which enhances plume dispersion for distances of several building heights.

If a plume gets caught in the cavity, concentrations next to the building can be relatively high. If the plume escapes the cavity but remains in the turbulent wake, it may be carried downward and dispersed more rapidly by the turbulence. This can result in either higher or lower concentrations than would occur without the building, depending on whether the reduced height or increased turbulent diffusion has the greater effect. The height to which the turbulent wake has a significant effect on the plume is generally considered to be about the building height plus 1.5 times the lesser of the building height or width. This results in a height of 2.5 building heights for cubic buildings, and less for tall, slender buildings. Since it is considered good engineering practice to build stacks taller than adjacent buildings by this amount, this height is called the "good engineering practice" (GEP) stack height.

Most treatments of building effects on dispersion are based on incorporating two effects: (1) the effective reduction of source height associated

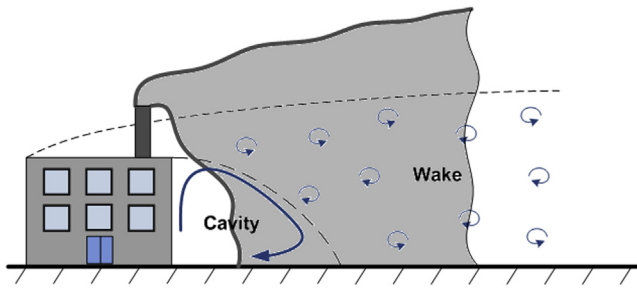

Figure A.3 Plume dispersion affected by cavity and wake behind building.

with the trapping of pollutants in the cavity and (2) the increased turbulence in the building wake. If the emissions are entrained into the cavity, the source is assumed to be at ground level, but the plume is assigned initial values to account for the fact that the emissions originate from a cavity whose size scales with the dimensions of the building. For example, the initial spreads of the plume are taken to be

$$\begin{aligned} \sigma_{yo} &= \alpha w \\ \sigma_{zo} &= \beta h \end{aligned} \tag{A.66}$$

where w and h are the width and height of the building, and α and β are constants. Alternatively, these initial spreads can be modeled in terms of a "virtual" source at ground level at an upwind distance that results in these spreads.

The fraction of the emissions that is entrained into the building cavity is taken to be a function of the stack height and the building height. The fraction that is not entrained into the cavity is treated as a conventional point source, except that plume dispersion is enhanced to account for the increased turbulence levels in the building cavity. The concentration at a downwind receptor is then a sum of the concentrations from the elevated source and the ground-level source, corresponding to the emissions from the cavity. Current models, such as the PRIME algorithm (Schulman et al., 2000) use approaches based on these ideas.

Terrain Treatment

Several complicated processes govern dispersion in complex terrain. Under unstable conditions the plume is depressed towards the surface of the obstacle as it goes over it. The implied compression of the streamlines is associated with a speedup of the flow and an amplification of vertical turbulence. Under stable conditions, part of the flow flowing towards an obstacle tends to remain horizontal, while the other part climbs over the hill.

Terrain features can rise toward the plume, deflecting its flow over or around, or allowing the plume to come in contact with the terrain. In convective (unstable) conditions the airflow, and thus the plume, is forced over the terrain obstacle. On the lee side of the obstacle a wake or cavity may occur in the flow, resulting in high concentrations on that side of the terrain feature.

The alignment of ridges and valleys can channel the flow. This can result in high concentrations appearing in areas quite different than would

be expected if this effect were not accounted for. The presence of hills and valleys can also help to create local wind flows that may affect the transport of plumes.

Accounting for these effects in air quality models presents a significant challenge. The effects cannot be ignored in regulatory modeling since terrain effects generally contribute to higher concentrations than would be observed in flat terrain situations. On the other hand, representing terrain effects accurately may require the use of computational fluid dynamics models or other modeling approaches that require extensive computer resources, and are difficult and time consuming to use.

The complex terrain model described (Venkatram et al., 2001) here is similar to that incorporated into the AMS/EPA Regulatory Model (AERMOD; Cimorelli et al., 2005). The model is essentially an interpolation of knowledge of flow and dispersion in complex terrain in two asymptotic states. Under very stable conditions, the flow and hence the plume embedded in it, tends to remain horizontal when it encounters an obstacle.

Under unstable conditions the plume is more likely to climb over the obstacle. Thus the very stable and very unstable conditions represent the two asymptotic states. Under unstable conditions the plume is depressed towards the surface of the obstacle as it goes over it. The implied compression of streamlines is associated with speedup of the flow and amplification of vertical turbulence. These and other effects are accounted for in models such as the Complex Terrain Dispersion Model (CTDMPLUS; Perry, 1992) that attempt to provide accurate concentration estimates for plumes dispersing in complex terrain.

AERMOD uses a much simpler approach because the objective is to estimate the frequency distribution of possible concentrations. It assumes that this distribution of concentrations can be generated by estimating concentrations at a chosen set of receptors on the terrain feature of interest. It also assumes that the details of the flow field, while affecting the location of the concentration; do not have a major impact on the magnitude of the concentration. Thus the concentration at a receptor is estimated by assuming that the plume travels in a straight line from the source to the receptor. The micrometeorology associated with any transport direction corresponds to measurements at a tower that reflects the effects of the terrain on flow and turbulence. In summary AERMOD generates the concentration distribution with inputs, consisting of micrometeorology and receptor locations, whose joint distribution is derived from observations.

As shown in Fig. A.4, AERMOD assumes that the concentration at a receptor, located at a position (x,y,z), is a weighted combination of two concentration estimates: one assumes that the plume is horizontal, and the other assumes that the plume climbs over the hill. The concentrations associated with the horizontal plume dominate during stable conditions, while those caused by the terrain-following plume are more important during unstable conditions. These assumptions allow us to write the concentration, $C(x,y,z)$, as

$$C(x, y, z) = fC_f(x, y, z) + (1 - f)C_f(x, y, z_e). \tag{A.67}$$

The first term on the right-hand side of Eq. (A.67) represents the contribution of the horizontal plume, while the second term is the contribution of the terrain-following plume. The weighting factor, f, is discussed later.

The concentration, $C(x,y,z)$, is that associated with a plume unaffected by the terrain. The plume axis remains horizontal. Thus $C_f(x,y,z)$ is evaluated at the receptor height, z, to simulate a horizontal plume. In the second term the concentration is evaluated at an effective height, z_e, given by

$$z_e = (z - z_h), \tag{A.68}$$

which assumes that the plume climbs over the hill. Here z_h represents the height of the terrain at (x,y), so that $(z - z_h)$represents the height of the receptor above local terrain.

Note that the receptor location is treated in the same manner as meteorology in the sense that it is simply one of the inputs that generate concentrations. Thus the model does not pretend to provide estimates of spatial concentration patterns at a specific time. A concentration estimate at a receptor is only a plausible value that could occur at that receptor; the meteorology does not specify a specific time for all receptors.

The Weighting Factor, f

The formulation of the weighting factor, f, uses the concept of the dividing streamline height, H_c. Although the concept has been discussed elsewhere, it is worthwhile to reexamine the underlying assumptions and the derivation of the expression for H_c. Consider a parcel of air of unit mass at certain height, h, with horizontal velocity $U(h)$. In a stably stratified environment, upward motion requires work done against downward buoyancy forces. Thus, in order to climb a hill, the parcel of air will have to exchange its kinetic energy for the potential energy required to work

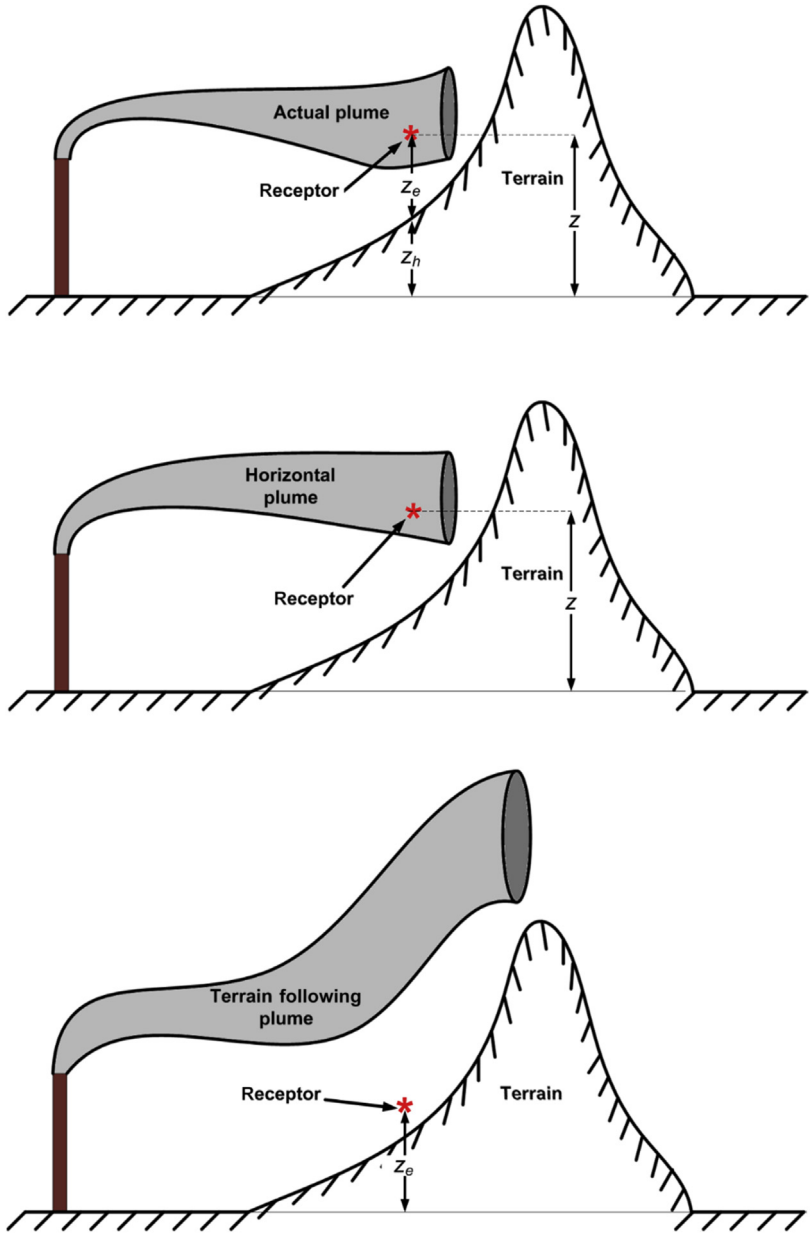

Figure A.4 Two-state approach. The total concentration predicted by Complex Terrain model is the weighted sum of the two extreme possible plume states.

against buoyancy forces. To examine whether the air parcel has kinetic energy to climb to a height z, we need to calculate the work done against the negative buoyancy forces. The downward buoyancy force at a height z is

$$F = g\left(1 - \frac{\rho_s}{\rho_p}\right) \approx g\left(1 - \frac{\theta_p}{\theta_s}\right) \tag{A.69}$$

where ρ refers to the density, θ is the potential temperature, the subscript "s" refers to the surroundings, and the subscript "p" refers to the air parcel. If we assume that the motion of the parcel is adiabatic, the potential temperature of the parcel remains at the value at its starting position h. Then the potential temperature difference between the parcel and its surroundings is equal to the surrounding potential temperature difference between z and h. Then the downward buoyancy force can be written as

$$F = \frac{g}{\theta_s}\int_h^z \frac{d\theta}{dz}\,d\zeta \approx \int_h^z N^2(\zeta)d\zeta, \tag{A.70}$$

where ζ is a dummy integration variable, and $N(z)$ is the local Brunt–Vaisala frequency. Then, neglecting drag forces on the parcel, the work done in pushing the parcel up from h to z is

$$W = \int_h^z F(\zeta)d\zeta. \tag{A.71}$$

If the expression for F from Eq. (A.70) is substituted into Eq. (A.71) and the resulting expression integrated by parts, we obtain

$$W = \int_h^z (z-\zeta)N^2(\zeta)d\zeta. \tag{A.72}$$

Notice that the Brunt–Vaisala frequency, $N(z)$, is zero in an adiabatic atmosphere: an air parcel is neutrally buoyant during vertical motion. Thus in this idealized analysis, which neglects drag forces, no work is done in moving a parcel vertically in an adiabatic atmosphere.

Now consider a receptor at height z. If we assume that the horizontal velocity is either constant or increases with height, we can always find a height above which the fluid has enough kinetic energy to climb to the receptor height. The critical dividing streamline height, H_c, is that height above which a fluid parcel has just enough kinetic energy to climb to

receptor height. This height is obtained by equating the work done in the climb to the kinetic energy. From Eq. (A.71), we find

$$\frac{1}{2}U^2(H_c) = \int_{H_c}^{z} (z-\zeta)N^2(\zeta)d\zeta. \tag{A.73}$$

The left-hand side of the equation is the kinetic energy of the parcel at H_c. If the potential temperature varies linearly with height, the Brunt–Vaisala frequency is essentially constant, and we obtain the simple expression

$$H_c = z - \frac{U(H_c)}{N}. \tag{A.74}$$

We see that U/N is the vertical distance that a parcel at any height can climb before it runs out of kinetic energy. Notice that the dividing streamline height, H_c, depends on the receptor height, z. Although the concept of dividing streamline height is based on an idealized scenario, towing tank experiments by Snyder et al. (1985) indicate that it can usefully characterize the flow of a stably stratified fluid around a three-dimensional obstacle. It turns out that if H_c is calculated relative to the top of the hill, the flow below H_c tends to flow around the hill, while that above H_c climbs over the hill. This suggests that the part of a plume embedded in the flow above H_c will have an impact on the hill above the effective plume height, while that below it will remain horizontal. This leads to the tentative assumption that f is a function of the fraction, ϕ, of the plume that is below H_c,

$$\phi = \frac{\int_0^{H_c} C_f(x,y,z)dz}{\int_0^{\infty} C_f(x,y,z)dz}. \tag{A.75}$$

Fig. A.5 illustrates how the weighting factor is constructed.

This fraction goes to zero under unstable conditions because H_c is zero. The weight, f, is taken to be

$$f = \frac{1}{2}(1+\phi). \tag{A.76}$$

When ϕ goes to unity the entire plume lies below H_c, and f goes to unity. Under these conditions the hill concentrations are entirely determined by the horizontal plume.

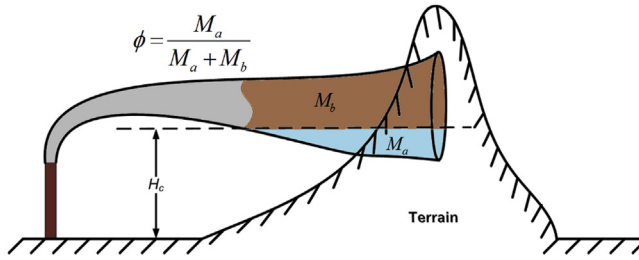

Figure A.5 Construction of the weighting factor used in calculating total concentration.

When ϕ goes to zero under unstable conditions, f becomes 1/2. Thus, under unstable conditions, the concentration at an elevated receptor is the average of the contributions from the horizontal plume and the terrain-following plume. This means that when the plume height is just above or below (in units of vertical spread) the receptor height, the hill concentration is enhanced over that in flat terrain. When the plume is well above the receptor, both components of the plume contribute equally, and the concentration reduces to that over flat terrain, as it should. When the plume is well below the receptor height the horizontal plume makes a negligible contribution, and the hill concentration is half the value of that in flat terrain. Clearly this is a simplification because the concentration at the receptor under these conditions could be close to zero if the flow does not carry the plume to the receptor. On the other hand the concentration could approach the flat terrain value if the flow carries the plume over the receptor. Thus the factor, f, could range from zero to unity depending on the details of the flow. Using $f = 1/2$ is a simplification that will lead to an overestimate of the concentrations under some circumstances.

In a region with a number of irregular hills the dividing streamline height, H_c, is not likely to describe the two-layer flow seen around a simple isolated hill in a laboratory (Snyder et al., 1985). However, we can apply the underlying concepts to real terrain by assuming that the plume can potentially affect the receptor if the flow can carry the plume over a vertical distance, H, equal to the local terrain height, z_h, plus the effective plume height, h_e,

$$H = z_h + h_e. \tag{A.77}$$

Then H_c is calculated by putting $z = H$ in Eq. (A.74).

Eq. (A.77) embodies the idea that the local terrain at height, z_h, is at ground level relative to the plume if the flow has enough energy to carry

the plume to the height, H. The receptor located at height, z, sees a plume at a height h_e above the terrain. The concentration at the receptor can be then estimated using a "flat terrain" model with the plume released at h_e. The fraction of the emissions that contributes to this flat terrain concentration is determined by the weighting factor, f, given by Eq. (A.76).

REFERENCES

Csanady, G.T., 1973. Turbulent Diffusion in the Environment. Springer.

Cimorelli, A.J., Perry, S.G., Venkatram, A., Weil, J.C., Paine, R.J., Wilson, R.B., et al., 2005. AERMOD: a dispersion model for industrial source applications. Part I: general model formulation and boundary layer characterization. J. Appl. Meteorol. 44, 682–693. Available from: https://doi.org/10.1175/JAM2227.1.

Draxler, R.R., 1976. Determination of atmospheric diffusion parameters. Atmos. Environ. 10, 99–105. Available from: https://doi.org/10.1016/0004-6981(76)90226-2.

Perry, S.G., 1992. CTDMPLUS, a dispersion model for sources in complex topography. Part I: technical formulations. J. Appl. Meteorol. 31, 633–645.

Schulman, L.L., Strimaitis, D.G., Scire, J.S., 2000. Development and evaluation of the PRIME Plume Rise and Building Downwash Model. J. Air Waste Manage. Assoc. 50, 378–390. Available from: https://doi.org/10.1080/10473289.2000.10464017.

Snyder, W.H., et al., 1985. The structure of the strongly stratified flow over hills: dividing streamline concept. J. Fluid Mech. 152, 249–288.

Taylor, G.I., 1922. Diffusion by continuous movements. Proc. Lond. Math. Soc. 2 (1), 196–212.

Venkatram, A., Brode, R., Cimorelli, A., Lee, R., Paine, R., Perry, S., et al., 2001. A complex terrain dispersion model for regulatory applications. Atmos. Environ. 35. Available from: https://doi.org/10.1016/S1352-2310(01)00186-8.

Weil, J.C., 1988. Plume rise. In: Venkatram, A., Wyngaard, J.C. (Eds.), Lectures on Air Pollution Modeling. American Meteorological Society, Boston, MA.

INDEX

Note: Page numbers followed by "*f*" and "*t*" refer to figures and tables, respectively.

A

Above ground level (AGL), 84, 117–118, 131
Adiabatic lapse rate, 23–25
ADMS. *See* Atmospheric dispersion modeling system (ADMS)
AERMOD model, 4, 9, 62–63, 107, 141–143
AGL. *See* Above ground level (AGL)
Air, 13
  composition, 17–18
  density, 15
  pollutants, 8, 18
  quality
    model, 2
    monitoring studies, 1
Anticyclones, 26–27, 32–33
AQMesh pods, 131
Argon, 17
Asthma, 1
Atmospheric boundary layer, 18, 37, 40–42, 41*f*
  dispersion, 61–73
    horizontal spread in surface boundary layer, 72–73
    plume spread formulation used in current models, 67–69
    stable surface boundary layer, 70–72
    unstable surface boundary layer, 69–70
  point source, 60–61
  turbulence in, 42–46
Atmospheric dispersion modeling system (ADMS), 82–83
Atmospheric pressure, 15, 18
Atmospheric stability, 22–25, 22*f*, 23*f*

B

Bar, 18, 21
Basel Urban Boundary Layer Experiment (BUBBLE), 144
Biased approach, 9
Bowen ratio, 42
"Broad brush" PGT curves, 62
BUBBLE. *See* Basel Urban Boundary Layer Experiment (BUBBLE)
Building(s), 105–106
  effects, 142
    application of models, 107
    challenges for practical application of models, 115–117
    models for, 119–124
  impact on mean winds and turbulence, 110–112
  morphology, 110, 126*t*, 130
Buildings impact on urban air quality. *See also* Highways impact on urban air quality
  comparison of model with observations, 124–133
    Los Angeles field measurements, 125–127
    VDM evaluation with data collected in Los Angeles and Riverside, 127–133
  models for building effects, 119–124
    OSPM, 119–121
    VDM, 121–124
  primary effects of buildings on dispersion of traffic emissions, 108–119
    buildings impact on mean winds and turbulence within UCL, 110–112
    challenges for practical application, 115–117
    primary variables governing dispersion in cities, 117–119
    vortex flow and street canyons, 112–115
Buoyancy
  forces, 44–45
  production, 58
Businger–Dyer expression, 65–66

C

Canyon plume box model (CPBM), 116
Carbon dioxide, 17–18, 40–41
Carbon monoxide (CO), 1, 4, 124, 131
  concentrations, 114
  measurements, 131
  near-road concentrations, 130
  traffic-emitted, 126
CFD model. *See* Computational fluid dynamics model (CFD model)
Cold air mass, 35–37
Composition of air, 17–18
Comprehensive models, 133–134, 145
Comprehensive Turbulent Aerosol Dynamics and Gas Chemistry model (CTAG model), 97
Computational fluid dynamics model (CFD model), 115
Concentrations
  expression, 13–17
  of highway emissions, 78–79
  of primary emissions, 77–78
  of traffic emissions, 87
Condensation particle counters, 125, 127
Constant lapse rate, 20
Convective boundary layer height, 52–54, 52*f*
Convective velocity scales, 8–9, 44–46
Coriolis acceleration, 27–29
Coriolis force, 25–29, 30*f*, 34
  motion of ball
    on turntable, 27*f*
    along wire on rotating turntable, 28*f*
  rotation of Earth as function of latitude, 29*f*
Coriolis parameter, 29, 56
CPBM. *See* Canyon plume box model (CPBM)
CTAG model. *See* Comprehensive Turbulent Aerosol Dynamics and Gas Chemistry model (CTAG model)
Cyclones, 26–27, 32
Cyclonic rotation, 32, 35–36
Cylinder of air, 19, 19*f*

D

Daytime boundary layer, 50–54
  height of convective boundary layer, 52–54, 52*f*
Depressed roads model, 93–96, 95*t*
  deriving expression for concentration, 100*f*
  mean velocity vectors for depressed road configurations, 94*f*
Depressed roadways, dispersion from, 92–93
Dilution wind speed, 81
Dispersion
  in atmospheric boundary layer, 61–73
    horizontal spread in surface boundary layer, 72–73
    plume spread formulation used in current models, 67–69
    stable surface boundary layer, 70–72
    unstable surface boundary layer, 69–70
  curves, 62
  from depressed roadways, 92–93
  from elevated stacks, 50
  models/modeling, 58–60, 107
    integrating dispersion models into modeling system, 141–145
    meteorological inputs-internal boundary layer model, 142–145
    for near-road air quality, 139–140
  primary effects of buildings on dispersion of traffic emissions, 108–119
    buildings impact on mean winds and turbulence, 110–112
    challenges for practical application of models of building effects, 115–117
    primary variables governing dispersion in cities, 117–119
    vortex flow and street canyons, 112–115
  of vehicle-emitted pollutants, 10
Displacement, 6
Dominant length scale, 108–110
Downwind barrier model, 87–90
Dry adiabatic lapse rate, 24–25
Dry deposition, 2

E

Eddy diffusivity, 62–63, 122
  equation, 64
  of turbulence, 44, 56
Effective aspect ratio, 129–130
EMFAC
  EMFAC 2007, 117–118
  EMFAC 2011, 133–134
  model, 5
Emission
  factor, 5–6
  models, 125–126
  of pollutants from vehicles, 5
  rates, 7–8
Empirical model, 89, 145
Empirical regression models, 115
Entrainment factor, 88–89
EPA wind tunnel study, 93
Error function (*erf*), 79–80
"EU-LIFE project SPAS", 87
Eulerian grid models, 2–3, 77–78

F

Federal Test Procedure (FTP), 5
  emission factor, 6
  FTP/correction factor approach, 5
First law of thermodynamics, 21
Free convection velocity scale, 8–9, 53
Friction(al)
  effects, 34–35
    turning of wind by frictional forces, 34*f*
  force, 25
  velocity, 46–47
Fronts, 35–37, 36*f*
FTP. *See* Federal Test Procedure (FTP)
Fuel
  consumption rates, 7–8
  fuel-based emission factor, 7

G

Gamma function, 63–64
Gaussian dispersion equation, 83–84
Gaussian distribution, 60–61, 60*f*, 67, 87–88, 100–101
Gaussian formulation, 61
Gaussian plume model, 112, 116
Geostrophic wind, 29–31, 30*f*
Gravitational force, 6
Greenhouse
  effect, 17–18
  gases, 40–41
Ground-level concentration, 58–59, 65–67, 79–80, 114, 120
  behavior, 69
  crosswind, 66*f*
  from ground-level point source, 82–83
Guy Ballot's Law, 31

H

Hadley cell, 33
Heat and momentum
  eddy diffusivities for, 63
  surface fluxes, 50
"Heat Island" temperature difference, 142–143
High-pressure
  center, 32–33, 32*f*
  regions, 32
Highway dispersion models, 81–82, 85*f*
Highway modeling, 81–84
  comparison of highway models with observations, 84
Highways impact on urban air quality, 77. *See also* Buildings impact on urban air quality
  line source dispersion model, 78–81
  modeling highway, 81–84
  models for impacts of barriers
    dispersion from depressed roadways, 92–93
    downwind barrier model, 87–90
    effects of solid barriers, 84–87
    effects of vegetation barriers, 96–98
    model for depressed roads, 93–96
    model for solid-vegetation barrier, 98–99
    model for upwind barrier, 90–92
Horizontal spread equations, 72
Hydrocarbons, 4, 18
Hydrostatic balance equation, 8
Hydrostatic equilibrium, 18–21, 19*f*

I

IBL model. *See* Internal boundary layer model (IBL model)
Idaho National Laboratory (INL), 84
Ideal street canyon, 112, 115–116
Inertial sublayer, 108–112
INL. *See* Idaho National Laboratory (INL)
Internal boundary layer model (IBL model), 108–110, 141, 143*f*
Isobars, 30, 35
  surface, 31
Isolated roughness flow, 113–114, 113*f*

K

Krypton, 17

L

LAD. *See* Leaf area density (LAD)
Lagrangian particle models, 115
Large Eddy Simulation (LES), 97–98
Large-scale winds, 25
  Coriolis force, 27–29
  pressure gradient force, 25–27
Latent heat flux, 41–42
Leaf area density (LAD), 97–98
LES. *See* Large Eddy Simulation (LES)
Line source dispersion model, 78–82, 78*f*. *See also* Vertical dispersion model (VDM)
Local contribution, 118, 127–129
Local topography, 58
Los Angeles field study
  locations of field measurements of UFP, 126*t*
  measurements, 125–127
  VDM evaluation with, 127–133
Low-pressure
  center, 32–33, 32*f*
  regions, 32

M

Mass
  balance, 3
  per unit volume, 13
  ratio, 15
  transfer, 18
Mass conservation equation, 62–63, 81–82
McElroy–Pooler curves, 61–62
Mean wind
  coordinate system, 78–79
  speeds, 110–111
Mesoscale flows, 58
Meteorological inputs-IBL model, 142–145
  IBL development, 143*f*
Micrometeorology and dispersion, fundamentals of, 8–9, 39–40, 58
  atmospheric boundary layer, 40–42, 41*f*
  daytime boundary layer, 50–54
  dispersion in atmospheric boundary layer, 61–73
    horizontal spread in surface boundary layer, 72–73
    plume spread formulation used in current models, 67–69
    stable surface boundary layer, 70–72
    unstable surface boundary layer, 69–70
  friction velocity, 46–47
  Monin–Obukhov length, 47–50
  nighttime boundary layer, 54–60
  point source in atmospheric boundary layer, 60–61
  surface energy balance, 40–42
  turbulence in atmospheric boundary layer, 42–46
    convective velocity scale, 44–46
  updrafts and downdrafts caused by surface heating, 51*f*
Mixed layer, 46
Mixed-wake model, 90
Mixing ratio (q), 13–14
MOBILE model, 5
"Modal" model, 7
Molar concentration of mixture of gases, 16
Mole fraction, 16
Monin-Obukhov length, 8–9, 46–50, 89
  surface layer similarity, 47–50
Monin–Obukhov similarity theory, 47–48, 143–144

N

Near-road air quality, dispersion models for, 139–140
Neon, 17
Nighttime boundary layer, 54–60
  dispersion modeling, 58–60
  ground-level source, 58–60
  turbulent velocities in stable boundary layer, 57–58
Nitrogen, 15, 17
Nitrogen oxides (NO_x), 1, 4, 131
NO_2, 131

O

Operational models, 107
Operational Street Pollution Model (OSPM), 107–108, 116, 119–121
  air flow within idealized street canyon, 113*f*
  direct contribution model, 118
  recirculating contribution model, 129
Oxygen, 15, 17, 40
Ozone (O_3), 40, 131
  molecular mass, 16

P

Particle models, 3
Pasquill–Gifford–Turner curves (PGT curves), 61–62
Perfect gas law, 14, 21
Personal exposure, 105–106
PGT curves. *See* Pasquill–Gifford–Turner curves (PGT curves)
Physical processes, 8, 108
Plan area fraction, 110
Plume spreads, 81–82
  equations, 73
  formulation used in current models, 67–69
Plume-based models, 3
Pods, 131
Porous barriers, 87
Potential temperature, 21–22, 24
Pressure
  force, 19
  gradient force, 25–27
Primary effects of barriers, 87
PRIME algorithm, 107
Puff models, 2–3, 77–78

R

Radiation-induced surface inversion formation, 54
"Recirculating" contribution, 116–117, 120
Reduction of average (σ_w), 142
Reduction of dispersion, 142
Reynolds number, 42
Riverside field study, VDM evaluation with, 127–133
RLINE model, 81–82
Roadway(s), 1
  dispersion from depressed, 92–93
  emissions on air quality, 1
Rolling friction, 6
Roof-level concentration, 141–142
Rooftop wind speed, 112, 114–117
Roughness sublayer, 108–111

S

Semi-empirical box models, 115
Semi-empirical Gaussian plume models, 115
Semi-empirical models, 90, 117
Sensible heat flux, 41–42, 53–54, 62
Shear production of turbulence scale, 46–47
SIRANE model, 124
Skimming flow, 113–114, 113*f*
Soil heat flux, 41
Solar radiation, 25, 40
  diffuse component, 40
  intensity, 25
Solid barrier effects, 84–87, 86*f*
Solid-vegetation barrier model, 98–99
Sonic anemometers, 117–118, 130–131, 144
Stable boundary layer, 56
  turbulent velocities in, 57–58
  vertical profile of potential temperature and velocity in, 55*f*
  Zilitinkevich's expression for, 56

Stable potential temperature gradient, 52, 57–58
Stable surface boundary layer, 70–72
State-of-the-art operational near-road dispersion model, 119
Street canyon(s), 112–115
  building array flow regimes, 113*f*
  dispersion models, 115–117
  models, 107
  OSPM schematic showing the air flow, 113*f*
STREET model, 116
Street scale, 107–108, 110
Street-level concentration, 141–142
Sulfur dioxide (SO_2), 16–17, 131
Surface boundary layer, horizontal spread in, 72–73
Surface energy balance, 40–42, 41*f*
Surface friction velocity, 89
Surface layer similarity, 47–50
Sustainable communities, 106

T

Temperature, 21–22
Thermal radiation, 17–18, 40–41
TKE. *See* Turbulent kinetic energy (TKE)
TOD. *See* Transit-oriented development (TOD)
Traction power, 6
Traffic emission
  concentrations, 87
  models, 8
  rate, 125–126
Traffic flow measurements, 117–118
Transit-oriented development (TOD), 106
Transport/transportation, 1–2
  emissions, 3–4
  modeling emissions for transport applications, 4–8
    forces acting on car, 6*f*
  sector, 4
Turbulence, 2, 42
  energy production, 54
  levels, 110–111
Turbulent flows, 42, 43*f*
Turbulent kinetic energy (TKE), 84–86, 86*f*
Turbulent velocities in stable boundary layer, 57–58

U

UBL. *See* Urban boundary layer (UBL)
UCL. *See* Urban canopy layer (UCL)
UFP. *See* Ultrafine particles (UFP)
Ultrafine particles (UFP), 98, 124–125, 128–129
Unstable surface boundary layer, 69–70
Unsteady Gaussian puff models, 115
Upwind barrier model, 90–92
  recirculation zone and direct contribution, 92*f*
  wind velocity vectors
    in presence of solid barrier, 91*f*
    in presence of two solid barriers, 91*f*
Urban air quality
  buildings impact on
    comparison of model with observations, 124–133
    models for building effects, 119–124
    primary effects of buildings on dispersion of traffic emissions, 108–119
  highways impact on, 77
  line source dispersion model, 78–81
  modeling highway, 81–84
  models for impacts of barriers
    dispersion from depressed roadways, 92–93
    downwind barrier model, 87–90
    effects of solid barriers, 84–87
    effects of vegetation barriers, 96–98
    model for depressed roads, 93–96
    model for solid-vegetation barrier, 98–99
    model for upwind barrier, 90–92
Urban boundary layer (UBL), 108–110
Urban canopy, 106–107
  impact of buildings on mean winds and turbulence within, 110–112
Urban canopy layer (UCL), 108–110
  buildings impact on mean winds and turbulence within, 110–112
Urban dispersion models, 116–117
US EPA regulatory model, 107

V

VDM. *See* Vertical dispersion model (VDM)
Vegetation barrier effects, 96–98
Vehicles, 1–2
  vehicle-related emissions, 1
Vertical dispersion model (VDM), 107–108, 119, 121–124, 141. *See also* Line source dispersion model
  evaluation with data collected in Los Angeles and Riverside, 127–133
Vertical pollutant transport, 115
Volumetric mixing ratios, 15
Von Karman constant, 47–48
Vortex flow, 112–117

W

Wake interference flow, 113–114, 113*f*
Warm air mass, 35
Water vapor, 17–18, 24–25, 40–41
Wet adiabatic lapse rate, 24–25
Wind tunnel models of street canyons, 114–115

X

Xenon, 17

- Compiles into one reference the state of the science methods for relating roadway emissions to near road pollutant concentrations.
- Demonstrates with clear examples how the modeling is used to interpret and extrapolate measurements of pollutant concentrations near highways.
- Emphasizes how local-scale, semi empirical, steady-state modeling can be applied using only a small set of inputs.

Addressing transportation-related environmental issues is extremely important worldwide as urban areas are constantly searching for ways to mitigate impacts from transportation sources. *Urban Transportation and Air Pollution* synthesizes the state-of-the-art methods for estimating near-road concentrations of roadway emissions.

Dispersion models are critically useful for estimating the impact of roadway emissions in cities; however, many are complex and require detailed inputs not often available. The book provides the information needed to make estimates using methods based on a minimal set of model inputs that can be applied by a wide range of users in many situations.

The book begins with a brief discussion on different methods of characterizing vehicular emissions and the variation of these emissions under different driving and road conditions. It then describes models that account for the effects of road configurations, such as near-road solid barriers on near-road pollutant concentrations. Accompanied by an overview of the meteorology that governs dispersion in cities, the book concludes with presenting dispersion models that link traffic emissions with near-road concentrations in built-up urban environments.

Akula Venkatram, professor of mechanical engineering at the University of California-Riverside, United States, is an internationally recognized researcher in modeling dispersion of transportation-related pollutants in urban areas for more than 20 years. He has written extensively on the subject, and is the recipient of the United States Environmental Protection Agency's *Scientific and Technological Achievement Award* for expanding and improving the scientific and regulatory communities' ability to assess the impacts of mobile source emissions.

Nico Schulte, PhD, is an air pollution specialist in the Research Division of the California Air Resources Board, United States. He has written on modeling dispersion of road emissions and the impact of near-road solid barriers and urban buildings on ground-level pollutants.

Social Sciences

ISBN 978-0-12-811506-0

9 780128 115060

ELSEVIER

elsevier.com/books-and-journals